SYNTHETIC APERTURE FOCUSING TECHNIQUE IN FREQUENCY DOMAIN FOR INSPECTING TIMBER STRUCTURE USING ULTRASONIC ARRAY SYSTEM

A Dissertation

by

HUNGJOO KWON

Submitted to the Office of Graduate and Professional Studies of
Texas A&M University
in partial fulfillment of the requirements for the degree of

DOCTOR OF PHILOSOPHY

Chair of Committee,	Stefan Hurlebaus
Committee Members,	Ray W. James
	Anna C. Birely
	Alex (Gwo-Ping) Fang
Head of Department,	Robin Autenrieth

December 2019

Major Subject: Civil Engineering

ABSTRACT

A frequency-domain synthetic aperture focusing technique for orthotropic media (FD-ORTHO-SAFT) is developed for the in-situ inspection of wood products. The developed algorithm uses the fast Fourier transform to manipulate an ultrasonic array signal in a frequency-wavenumber domain for fast computation speed. In order to take into account the orthotropic property of the media, the group velocity curve information of the media is applied to the developed algorithm. The FD-ORTHO-SAFT algorithm is verified with the simulated ultrasonic array signal by the mathematical model and the finite-difference time-domain method. The performances of the algorithm with and without the noise are tested with the simulated signal by the mathematical model and the finite-difference time-domain method, respectively. The FD-ORTHO-SAFT algorithm is compared with the conventional time-domain synthetic aperture focusing technique for orthotropic media (TD-ORTHO-SAFT) in terms of the array performance index, performance map, and the computation time. The results of both algorithms are analyzed using the potential damage curve as well as the operating time. Also, the feasibility of the FD-ORTHO-SAFT is tested using measured ultrasonic array signals obtained by the commercial ultrasonic array device A1040 MIRA from wood specimens. The FD-ORTHO-SAFT algorithm shows a higher detectability than the synthetic aperture focusing technique algorithm for isotropic media and a faster computation speed than the conventional TD-ORTHO-SAFT. The results show that the FD-ORTHO-SAFT has a better performance for wood products than the time-domain method at the center of the array and has strong suitability for the in-situ inspection of wood products as well as short computation time.

DEDICATION

This dissertation is dedicated to

My wonderful wife, Ah Young, who has been supportive on my journey

My adorable daughter, Lucy, who taught me the pleasure of life

ACKNOWLEDGEMENTS

First of all, I would like to express my deepest gratitude to my committee chair, Dr. Stefan Hurlebaus, for his support, gudiance, and financial assistance throughout this research. He steadily conveyed a spirit of adventure regarding research and an excitement about teaching. Without his patient help this disseration would not have been possible.

I also would like to thank my committee members, Dr. Ray James, Dr. Anna Birely, and Dr. Alex (Gwo-Ping) Fang who gave me invaluable insightful comments on my research and helped me to finish my Ph.D.

Besides, I would like to appreciate my friends, colleagues, and the department faculty and staff for making my time at Texas A&M University a fabulous experience.

Last, but not the least, I am always appreciative of my beloved wife, parents, and parents-in-law for their endless love and unconditional suppport.

NOMENCLATURE

API	array performance index
CT	computed tomography
DI	damage index
FD-ISO-SAFT	frequency-domain synthetic aperture focusing technique for isotropic media
FD-ORTHO-SAFT	frequency-domain synthetic aperture focusing technique for orthotropic media
FD-SAFT	frequency-domain synthetic aperture focusing technique
FFT	fast Fourier transform
ISO-SAFT	synthetic aperture focusing technique for isotropic media
NDT	non-destructive testing
SAFT	synthetic aperture focusing technique
SAFT-C	synthetic aperture focusing technique with combinational sounding
TD-ISO-SAFT	time-domain synthetic aperture focusing technique for isotropic media
TD-ORTHO-SAFT	time-domain synthetic aperture focusing technique for orthotropic media
TD-SAFT	time-domain synthetic aperture focusing technique

TABLE OF CONTENTS

LIST OF FIGURES

FIGURE Page

LIST OF TABLES

1. INTRODUCTION

1.1 BACKGROUND

Timber has been utilized as a structural component on account of its natural strength enough to support structural loads (Gutkowski and Williamson, 1983). Even in these days when high strength materials like concrete and steel have been widely used in the structural fields, timber accounts for a majority of structural components thanks to the development of construction technology (Kolb, 2008). However, wood, a living organism, results in the quality inconsistency of timber products, and the inconsistency makes it difficult to maintain timber structures. Therefore, there has been a high demand for a method to inspect timber elements.

The visual inspection method is a widely utilized method for diagnosing timber at first. It determines the grade of a wood based on the number of knots and the condition of the surface. Although the decision process is simple and quick, the method is not appropriate for accurate damage detection, as results only come from the surface condition and can be biased depending upon the inspector's view (Balendra et al., 2010).

The transverse vibration test was attempted to identify damage locations along the length of the timber element. Dynamic properties such as natural frequencies and mode shapes from the transverse vibration test were utilized to detect the locations of damage because they are sensitive to the stiffness of the element (Dackermann et al., 2010). The transverse vibration test results showed that a damage detection algorithm that uses dynamic properties, called index method, could find out the location of damage exactly. However, the method was unable to describe the shape of damage.

In order to overcome such a problem, methods that directly investigate sectional profiles were promoted. The resistance drill, X-ray and infrared radiation techniques are methods that directly examine the inside of timber, and their results are precise enough to describe the shape of the heterogeneous area. Nonetheless, they are not suitable for an in-situ inspection method, because the methods have limitations that require a lot of time and cost or cause destruction. The resistance drill requires multiple measurements to diagnose the damaged area and can cause potential damage to the wood specimen (Brashaw et al., 2005). The X-ray has constraints like the placement of a metal plate behind objects for recording images (Lechner et al., 2013) as well as the high risk to inspector's health and high expense (Lin et al., 2008). Also, the infrared radiation is applicable only at the time when a sudden temperature change occurs or an external heat source is applied, which requires more time to inspect specimens (López et al., 2014).

The ultrasonic wave is an acoustic wave that propagates in a material in a non-destructive manner, and reflected ultrasonic wave signals have information about damage in the material. Also, an understandable sectional image can be obtained if an image reconstruction algorithm called the synthetic aperture focusing technique (SAFT) is developed (Hoegh, 2013). There is a lot of research about developing the SAFT algorithm for isotropic media, but few studies are performed to develop the SAFT algorithm for orthotropic media like timber. The developed SAFT algorithm for orthotropic media is not suitable for an in-situ inspection method of timber element because of its slow computational speed (Hunter et al., 2008).

1.2 SIGNIFICANCE

There are many structures using timber elements which have required a precise investigation with a non-destructive manner in the United States. Although many studies about developing timber inspection methods were conducted, no one method satisfied criteria for in-situ inspection. This research will provide a comprehensive in-situ timber inspection method with a high accuracy, low cost, fast speed and increased safety. The developed technique will reduce the maintenance cost of timber structures and prevent timber structures from collapse in the future.

1.3 OBJECTIVES

The primary goal of this research is to provide a fast and reliable inspection method to maximize the service life of timber structures using an ultrasonic array system in a non-destructive manner. The ultrasonic array system, with a fast computational speed for inspecting timber structures, will be developed so that the technique can diagnose inside damage which can cause significant maintenance expenses in the future. The objectives of this study are:

1) to develop a frequency-domain synthetic aperture focusing technique algorithm for orthotropic material in order to investigate timber elements in a non-destructive manner and fast computational speed,

2) to check the detectability of the method with various parameters such as the shape of group velcity curve, array's spatial frequency, wave velocity, and impulse operating frequency, and

3) to validate the developed technique with the ultrasonic array signal experimentally obtained from wood specimens.

1.4 OUTLINE OF DISSERTATION

Chapter 1 tells about background information and the significance of inspecting methods for timber and explains the objectives of this study. Chapter 2 reviews literature about inspecting timber, post-processing algorithm for ultrasonic array system such as time- and frequency-domain synthetic aperture focusing technique for isotropic media, and wood products used in the structural field. Chapter 3 explains the theory of the frequency-domain synthetic aperture focusing technique algorithm for orthotropic media like wood. In Chapter 4, the algorithm verification is provided using ultrasonic array signals simulated by two techniques - the mathematical model and the finite-difference time-domain method. The parametric analysis follows in terms of the group velocity curve's shape, the array's spatial frequency, the wave velocity, and the impulse frequency in Chapter 5. Chapter 6 presents the algorithm validation using ultrasonic array signals experimentally obtained from the wood specimens. Finally, Chapter 7 presents a summary of findings, conclusions, and recommendations for future research.

2. LITERATURE REVIEW

2.1 WOOD INSPECTION METHODS

Wood is one of the main structural elements in the construction field, and wooden elements are required to have a certain level of strength to bear structural loads. However, wooden elements are made out of living organisms which have inconsistent strength even in a single tree. Thus, several studies about the evaluation of the wood strength have been developed in the past decades.

The following sections summarize the previous research works about the inspection of woods. The area of previous research includes 1) resistance drill, 2) transverse vibration, 3) electromagnetic radiation (infrared radiation, X-ray, and gamma ray), 4) electric resistivity, and 5) acoustic wave (stress wave and ultrasonic wave).

2.1.1 Resistance Drill

The resistance drill technique is a semi-destructive method that directly pricks a wood with a needle-like drill to evaluate the soundness of the wood as shown in Figure 2.1 (Isik and Li, 2003). The procedure is very straightforward, so the inspectors do not need specific training to perform measurements.

Figure 2.1: Resistance Drill in Use Reprinted from Brashaw et al. (2005)

Since the resistance drill device was developed a few decades ago, various studies about figuring out the relationship between the results of the resistance drill and the wood properties have been carried out. Comparison tests with resistance drill and the wood density were implemented to identify the relationship (Costello and Quarles, 1999; Isik and Li, 2003; Kasal, 2003; Johnstone et al., 2007). In addition to the wood density relationship, Ceraldi et al. (2001) figured out the statistical relationship between the wood density from the resistance drill and the compressive strength. Also, Calderoni et al. (2010) provided the experimental correlation between the destructive test results and the resistance drill results along the longitudinal direction and between the resistance drill longitudinal and transverse direction results on ancient timber elements. This made it possible to predict the ultimate strength perpendicular to the grain by the resistance drill transverse direction results, which are general results for in-situ inspection on structural elements.

Although the method has various advantages such as a quick inspection and simple usage, there are some drawbacks. The measurement results can be different dependent upon the operator's skill (Costello and Quarles, 1999), and the drilled holes can lead to a potential contamination of the wood specimen (Brashaw et al., 2005). Also, the knowledge about the biological structure of wood is required to understand the measurement precisely (Rinn, 2012).

2.1.2 Transverse Vibration

In contrast with the static bending test, which applies loads up to the failure to a structural system for evaluating the load capacity, the transverse vibration test is the dynamic test that provides the properties of the system without damaging it. Thus, the transverse vibration test is used as a non-destructive testing method to figure out the condition of the system. As shown in Figure 2.2, the test configuration generally consists of two parts: 1) exciting the system and 2) recording and analyzing the response. This method is called the global inspection method because the calculated dynamic properties from the obtained responses have the information of the entire system.

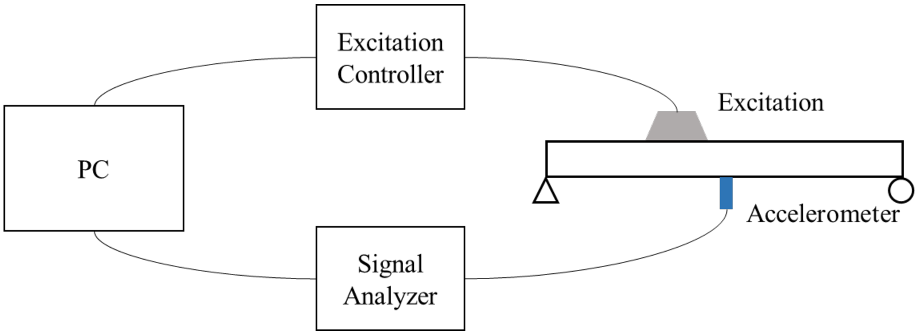

Figure 2.2: Transverse Vibration Test General Configuration

The dynamic properties of the system are a function of the mechanical properties of the system, thus the condition of the system can be estimated by the obtained dynamic properties. Various studies for evaluating the stiffness of the wood structure by the dynamic properties were carried out (Soltis et al., 1994; Ross et al., 2002; Choi et al., 2005; Hunt et al., 2007).

Even though the dynamic properties represent the condition of the system, it is hard to catch the damage location and severity directly from the dynamic properties. Thus, the Damage Index (DI) method that provides damage location and severity was proposed (Stubbs and Osegueda, 1990). The DI method determines the ratio of modal strain energies between healthy and damaged system. For a beam system, the DI value is described as

$$\beta_{ij} = \frac{(EI)_j}{(EI)_j^*} = \frac{\int_j (\phi_i''^*(x))^2 \mathrm{d}x \int_0^L (\phi_i''(x))^2 \mathrm{d}x}{\int_j (\phi_i''(x))^2 \mathrm{d}x \int_0^L (\phi_i''^*(x))^2 \mathrm{d}x} \tag{2.1}$$

where β_{ij} is the DI value of mode i and member j, $(EI)_j$ is the flexural rigidity of the member j, and ϕ_i'' is the curvature of the mode shape, ϕ_i. And it is assumed that the modal strain energy is not changed after the damage.

The normalized DI value Z_{ij} for the damage severity is given as

$$Z_{ij} = \frac{\beta_{ij} - \mu_{\beta_{ij}}}{\sigma_{\beta_{ij}}} \tag{2.2}$$

where $\mu_{\beta_{ij}}$ is the mean and $\sigma_{\beta_{ij}}$ the standard deviation of the β_{ij} for all j elements.

The DI method precisely identifies in the case of single damage. However, it leads to poor results for multiple damage. In order to solve this problem, the DI method in collaboration with artificial neural network (Dackermann et al., 2009; Samali et al., 2011) and the modified DI method (Dackermann et al., 2013) were proposed.

2.1.3 Electromagnetic Radiation

Some types of electromagnetic radiation are able to pass through materials and have a different attenuating ratio and different reflectivity depending on materials. With these phenomena, wood structures have been inspected in the non-destructive evaluation field. Below is the review of timber inspection using electromagnetic radiation technique.

2.1.3.1 Infrared Radiation

Damage in wood might be air voids or heterogeneous parts which have different thermal conductivity. Thus, if a variation of the surficial temperature exists, the infrared radiation technique can detect damage inside wood. The general type of the infrared radiation test setup is shown in Figure 2.3.

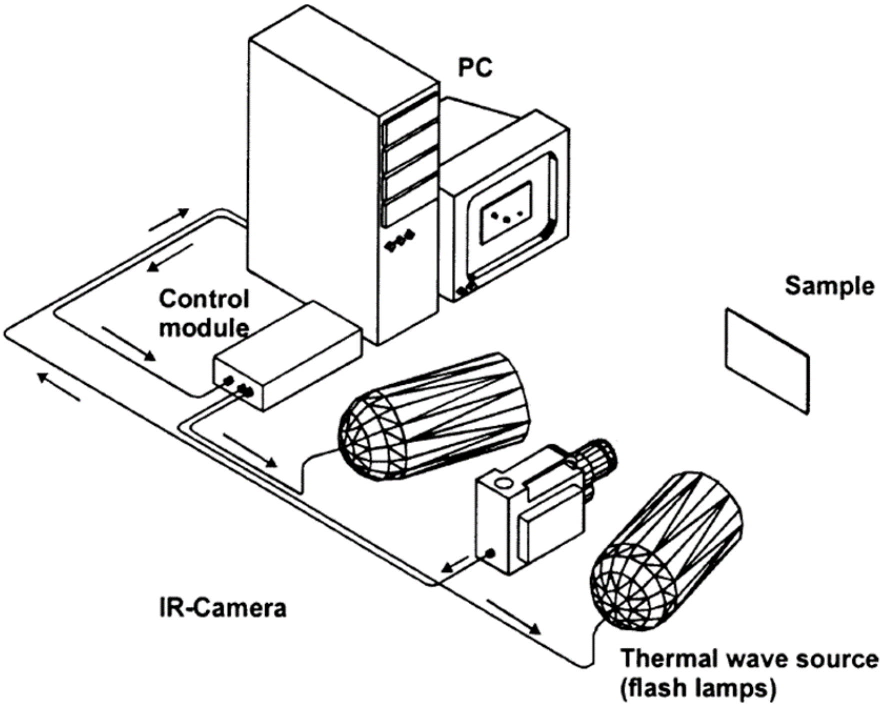

Figure 2.3: Infrared Radiation Test Setup Reprinted from Berglind (2003)

The temperature of wood sample is usually the same as the temperature of the atmosphere, hence the external heat is applied to cause a temperature variation. At first, studies about the infrared radiation for the general wood specimen with damage have been conducted (Tanaka and Divós, 2000; Wyckhuyse and Maldague, 2001; López et al., 2014). However, it has shown that the results were sensitively affected by other factors like temperature, moisture content, species and others, and it is difficult to identify the damage unless it is close to the surface (Wyckhuyse and Maldague, 2001). Hence, the research about the infrared radiation technique has been narrowed down to the inspection for flat wooden boards.

The studies about the inspection for wood boards (Wyckhuyse and Maldague, 2001; Meinlschmidt, 2005) and the research about detecting air voids in the laminated wood board (Berglind, 2003; Berglind and Dillenz, 2003) were carried out. These studies about the inspection for wood board have drawn satisfactory results.

2.1.3.2 X-ray and Gamma Ray

The capability of X-ray and gamma ray to penetrate an object without destruction helps to investigate the inside of a wood precisely. A penetrating ray is attenuated in a medium depending upon the material properties, and the intensity of the attenuated ray follows the Lambert-Beer law (Chen et al., 2010):

$$I = I_0 \exp(-\mu\sigma\rho) \tag{2.3}$$

where I_0 is the initial intensity, μ is the attenuation coefficient, σ is the thickness of the material, and ρ is the material density.

As I_0 and σ are constant values, the density of a wood can be estimated from the measured intensity if the thickness is known. The wood density is an index of the soundness of the wood (Lechner et al., 2013). For that reason, studies were carried out to determine the integrity of the wood by the estimated density using the measured ray intensity (Cown and Clement, 1983; Laufenberg, 1986; Divos et al., 1996; Lechner et al., 2013). Also, Chen et al. (2010) conducted the research about measuring the density distribution for four different wood-based panels to identify flexural properties of wood panels.

In the sawmill industry sorting out poor quality logs before cutting is one of the main factors for successful operation (Oja et al., 2001). Identifying the location and shape of the damage in a log is important in order to maximize the productivity of wood panels by achieving an optimal saw blade orientation with respect to the log (Halabe et al., 2009) as well. Thus, Oja et al. (2001) performed the study about anticipating the stiffness of sawn logs by X-ray. In other research, swan logs were scanned using computed tomography (CT), which generates a sectional profile with an advanced algorithm using a series of X-ray data, to measure the wood condition (Gupta et al., 1999; Oja, 1999).

A resulting image by the X-ray technique is more distinct compared to other inspecting methods. However, the feasibility of the X-ray technique on in-situ inspection is conditional based on the accessibility. Because a metal plate should be placed on the opposite side of an object to record penetrated radiation (Lechner et al., 2013). Besides, the X-ray technique is a high-cost and -risk (Lin et al., 2008; Veldman et al., 2011).

2.1.4 Electric Resistivity

The early stage of wood decay does not cause serious reduction of material properties, which makes it hard to be detected by the mechanical property-based inspection methods. However, it will induce the strength loss later (Müller et al., 2001). In the early stage of wood decay, a fungi growth results in the alternation of the moisture content in the infected area. The moisture content has a strong influence on the electric conductivity (Bieker et al., 2010). Therefore, the electric resistivity method can be used as an inspection method for recognizing the early stage of wood decay.

Larsson et al. (2004) used the four-point resistivity method, which applies an alternating current to a wood stem and then measures the voltage difference along the stem, to discover the wood decay in living trees. Bieker et al. (2010) utilized the electric resistivity tomography method to draw a colored sectional image for detecting white rot in Fraxinus excelsior. The results of both studies have shown many shortcomings: (1) not providing the damage location, (2) not applicable for frozen wood due to high resistivity, (3) not distinguishable between air voids and a wood decay (Larsson et al., 2004), and (4) difficulty of determining the wood decay by electric resistivity due to the overlapping between healthy wood and decayed wood boundary (Bieker et al., 2010).

2.1.5 Acoustic Wave

Acoustic wave is a particle movement in medium, and the behavior of particles is determined by the material properties. Hence, the behavior of wood particle was able to be used as an indicator of the specimen's condition.

2.1.5.1 Stress Wave

At the early stage of acoustic wave method, the attenuation shape of the wave was used to investigate the mechanical properties of wooden specimens. The general experimental setup is shown in Figure 2.4. The wave is triggered by the impact hammer and the behavior of the wave is recorded by accelerometers. The wave generated by the impact hammer is a so-called stress wave. Ross and Pellerin (1988) carried out the stress wave test on wood-based composites to evaluate the properties of specimens. They used the attenuation shape of the stress wave to predict the moduli of elasticity. The results show that a linear relationship was obtained between the stress wave and the moduli of elasticity. In the same manner, Ross et al. (1994a) used the stress wave shapes to distinguish the biologically degraded wood.

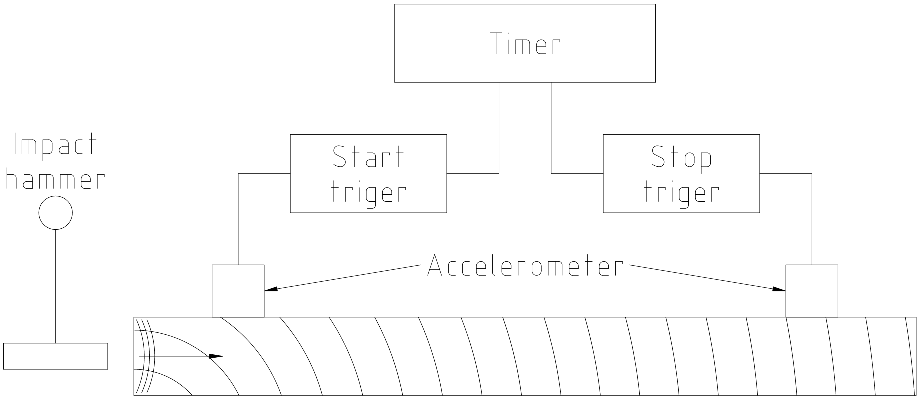

Figure 2.4: General Stress Wave Experimental Configuration for Non-Destructive Evaluation Modified from Ross et al. (1994a)

The information from the shape of the stress wave obtained even by a skillful operator is inconsistent, and the stress wave has a high noise level which disrupts the interpretation of signals. Therefore, a different type of wave information, the transit time, is used. The two accelerometers are placed at two known locations. Consquently, the velocity of the stress wave can be calculated if the transit time is measured. The velocity of the stress wave is determined by the density and the moduli of elasticity as

$$E = \rho c^2 \tag{2.4}$$

where E is the modulus of elasticity, ρ is the density, and c is the longitudinal wave velocity.

As the significant strength drop can occur without severe weight reduction, the weight cannot be used as an index of decay (Ross et al., 1999). Therefore, the stress wave velocity can be a barometer of the specimen's condition if we assume that the density of the material is a constant value. Ross et al. (1994b) conducted measuring transit time to identify the presence of infected wood on red and white oak lumber before kiln drying. The results have shown that the accuracy of the detecting mixed and severe bacterial heartwood in green red oak lumber was 84 percent while the accuracy of the nondestructive method on white oak lumber was 45 percent. Schad (1995) carried out nondestructive testing – transverse vibration and stress wave method – to evaluate the strength of wood. The results of the stress wave method have shown that the stress wave velocity appeared to be a great inspecting method for internal degradation of large wood members. Ross et al. (1999) introduced a new inspecting method, the stress wave technique, which will replace conventional methods like sounding, moisture meter, and drilling for evaluating wood. They also provided information about the effect of ring orientation, decay, moisture content, and preservative treatment on the stress wave transmission time. Wang et al. (2000) performed a nondestructive stress wave technique on standing trees to assess the strength and stiffness of the trees. The stress wave velocity was measured on the standing trees, and then, the moduli of elasticity and the rupture were calculated after cutting the trees and moving them to the laboratory. The comparison between the stress wave velocity and the mechanical properties has shown that high correlation was observed, and high variability was detected due to the small size of wood members. Ross (2001) studied the relationship between the stress wave transit time and the failure load on the Douglas-fir and eastern white pine timber removed from the service. The failure loads were measured along the parallel and perpendicular directions to the grain. The results showed that the transit times were inversely proportional to the failure loads. The linear inverse proportional relationship has been shown between them. Also, the strong relationship between the stress wave velocity and the static and dynamic moduli of elasticity was found in the study of Ross et al. (2005). In Japan, Sasaki et al. (2014) measured the stress wave velocity to predict the moduli of elasticity and investigate the status of the structure with 2D finite element method on the temple wooden structure which was scheduled for demolition. The results have revealed that the stress wave velocity method provided reliable results from the wooden structure even in the service.

2.1.5.2 Ultrasonic Wave

Although the impact hammer is simple to use, the impact hammer may not be appropriate for tests requiring a higher accuracy. The generated signals by the impact hammer are not identical and the inconsistently triggered wave signals can cause variations of the results. A highly skilled operator cannot trigger a constant wave using an impact hammer. In order to create an identical input signal, a transducer was introduced to transform an electric signal into acoustic signal. The example of the ultrasonic transducer is shown in Figure 2.5. The ultrasonic transducer typically generates an input signal with a frequency above 20 kHz, which is called ultrasound that induces high signal losses at interfaces. Therefore, a coupling agent or coupling gel is required to reduce a signal attenuation by applying to the interface between the transducer and the surface of the material. Also, dry contact and air coupled ultrasonic transducer, which does not need a coupling agent, was recently invented.

Figure 2.5: Ultrasonic Transducers (right bottom), Coupling Agent (right top), and Ultrasonic Pulse Receiver (left)

Because the behavior of the ultrasonic wave is strongly influenced by the physical properties of woods and other parameters (Sakai et al., 1990), studies about various factors on the ultrasonic behavior have been required. Sakai et al. (1990) carried out the research about the moisture content effect on the ultrasonic wave velocity and attenuation in different wood species. A nonlinear and anomalous relationship between the moisture content and the wave velocity as well as amplitude was found. Bucur and Feeney (1992) analyzed the attenuation ratio in terms of the wave frequency, the wave incidence angle, and the wood orientation. It has shown that the anisotropic properties of woods, the wave frequency, and the incidence angle of wave are influential on the attenuation of ultrasound. Sandoz (1993) investigated the effect of the moisture content and the temperature on the ultrasonic behaviors. In the study by Bucur and Böhnke (1994), an analysis of factors affecting the measurement of the ultrasound was performed. The results showed that the microstructure of wood anatomy was more influential on the ultrasonic behaviors as the ultrasonic frequency was increased. In addition to the previous studies, Oliveira et al. (2005) tried to find out the relationship between the ultrasonic velocity and the moisture content in Brazilian hardwood.

Like the stress wave which strongly related to the mechanical properties of the medium, the ultrasonic wave velocity also became a clue to the mechanical properties of woods. But, the behavior of the ultrasonic wave is influenced by various parameters such as wood species, product situations, transducer types, and other factors. Thus, there are several studies for finding out the relationship between the ultrasonic wave velocity and the parameters to verify the availability of the ultrasonic technique for evaluating woods. Sandoz (1989) used the ultrasonic wave technique to grade 341 spruce beam members from different regions. The ultrasonic test results were compared with the results of the four-point flexural bending test in terms of the moduli of elasticity and rupture. The influence of the moisture content and the knots was statistically analyzed, and the fact that the suggested method was very effective to identify the mechanical properties of the wood members was identified. Also, Sandoz (1996) employed the ultrasonic wave technique to find out how much the logs are degraded by comparing the referential ultrasonic wave speed with the measured ultrasonic wave speed. Oliveira et al. (2002) measured the ultrasonic wave velocity on Brazilian hardwoods to figure out the dynamic moduli of elasticity, and the measured values were compared with the static moduli of elasticity. Tucker and Bender (2003) applied the ultrasonic inspecting method with a water coupling system to wood-plastic composite panels to find out if the suggested method is affected by temperature. In order to get a good result, a proper wave frequency, water temperature, and incidence wave angle should have been determined. Marchetti et al. (2004) introduced a non-contact ultrasonic transducer for measuring the density of wooden panels. The measured wave velocities at the different locations of the wood samples were statistically averaged. The results revealed that the density was measured with the error of 1 to 2 percent and the presence and the location of the knot was identified. Arriaga et al. (2006) conducted the ultrasonic wave velocity test on the structural Tali timber to assess the strength and the stiffness of the specimen. The results have shown that the ultrasonic wave velocity has a strong relationship with the static moduli of elasticity with the coefficient of determination value of 0.42 to 0.74. A weak relationship was also found with the bending strength with the coefficient of determination value of 0.07 to 0.12. Oliveira and Sales (2006) investigated the effect of the wood density on ultrasonic velocity in different Brazilian tropical wood species. A relationship between the wood densities and the ultrasonic wave velocities was verified. The coefficient of determination within the species was 0.8 to 0.88, and the coefficient of determination between the species was 0.31. Dzbeński and Wiktorski (2007) estimated the mechanical properties of woods in standing trees using the ultrasonic wave velocities. It has been found that the ultrasonic wave along the trunk has strong relationship with the moduli of elasticity. Machado et al. (2009) explored the indirect ultrasonic wave technique, which places ultrasonic transducers on the same surface, for the estimation of the mechanical properties of clear woods. As the access of the structural elements in fields is constrained, the research tried to verify if the method is still effective with the constrained conditions. The results obtained showed that the ultrasonic wave velocity from the indirect method is heavily related to the ultrasonic wave velocity from the direct method with a coefficient of determinant of 0.9. Machado and Palma (2011) used the indirect ultrasonic technique again to evaluate the bending behavior of in-service pine timber structural elements, and the feasibility of the indirect ultrasonic method was verified.

In addition to the wood grading tool, the ultrasonic technique can be used as a damage detecting method, because the ultrasonic wave propagates slowly in the decayed wood medium (Emerson et al., 1999). Therefore, the transit time or the ultrasonic wave velocity can be an index of the damage presence. Ross and DeGroot (1998) measured the transmission time of the ultrasonic wave to identify the biologically degraded area in wood members. Also, they introduced the rolling ultrasonic transducer that can reduce the inspection time. Emerson et al. (1999) conducted the ultrasonic inspecting technique on the large rough-sawn creosote-treated timber beam. A square grid was drawn on the wooden beam surface, and the ultrasonic wave transit times were measured at every point. A contour map of transit timesf was generated. The results revealed that the contour map showed a similarity to the damage shape. Shaji et al. (2000) verified the feasibility of the ultrasonic inspecting technique on various damage. It has been found that the internal void, cracks, and discontinuities were detectable with the technique, and the presence of external loads was not influential on the inspection results. Carrasco and Teixeira (2012) also used the ultrasonic inspecting method to draw a damage contour map of the laminated wooden beam. The laminated wooden beam was intentionally designed to have internal cracks, holes, and voids. The ultrasonic wave velocity was calibrated at different points, and the contour map of the ultrasound velocity was drawn. The results demonstrated that the ultrasonic method provided a satisfactory output. Tallavo et al. (2012) applied the ultrasonic inspecting method to wood poles. Unlike typical wood members, wood poles have a cylindrical shape, and the effect of the anisotropic property on the ultrasonic wave propagation is huge. Thus, the sensitivity analysis about the ultrasonic wave velocity along the wave paths was performed. The reduction of the ultrasonic wave speed was identified if there was a deteriorated area on the wave path. Conde et al. (2014) used the ultrasonic inspecting method to evaluate the historical wooden structure, El Corral del Conde, in Seville. The ultrasonic technique results obtained were combined with the visual inspection results and the moisture content values to determine the status of wooden structural members. General types of ultrasonic transducers are directly attached to the surface of materials, and a coupling agent such as grease or liquid gel is applied between surfaces to reduce the energy loss for some types of transducers. However, there is a possibility that the coupling agent could penetrate a wood sample, contaminate it and affect the measured results. Also, a dry contact ultrasonic transducer, which does not require the coupling agent, has a weak reproducibility of the wave amplitude, and it is difficult to apply to an uneven surface (Sanabria et al., 2010). Hence, the demand of the noncontact ultrasonic transducer has been increasing. Fleming et al. (2005) used the noncontact ultrasonic transducer to identify the presence of exotic insects in wood packing materials. One inch thick wood samples were artificially drilled, and the larva was placed in the hole. It has shown that the noncontact ultrasonic transducer identified the artificial holes, but it did not detect the presence of the larva due to the energy loss at the interface of the wood and air. Sanabria et al. (2010) carried out the noncontact ultrasonic technique on the detecting the delamination area in the glued timber panel. The delaminated areas were detected to some degree, but there were interruptions by the heterogeneity of wood, the edge effect, and the small size of defects.

2.1.5.3 Tomography

Although the numerical value of the ultrasonic wave transit time provides an information about a wooden specimen, the provided information is one dimensional and too limited to draw the sectional profile of the specimen (Lin et al., 2008). Thus, a sensor chain was developed to gain several transit time information along various paths as shown in Figure 2.6. As it can be assumed that a transit time of a wave path represents the condition information along the wave path, the sectional profile of the specimen can be drawn with transit time information along diverse wave paths.

The basic procedure of the method is as follows. Once the geometry of the sensors' location is determined, the wave velocities along the paths can be calculated with the obtained transit time information. In Figure 2.7, the example of the wood section was scanned by the sensor chain, and the sectional profile was generated based on the calculated wave velocities.

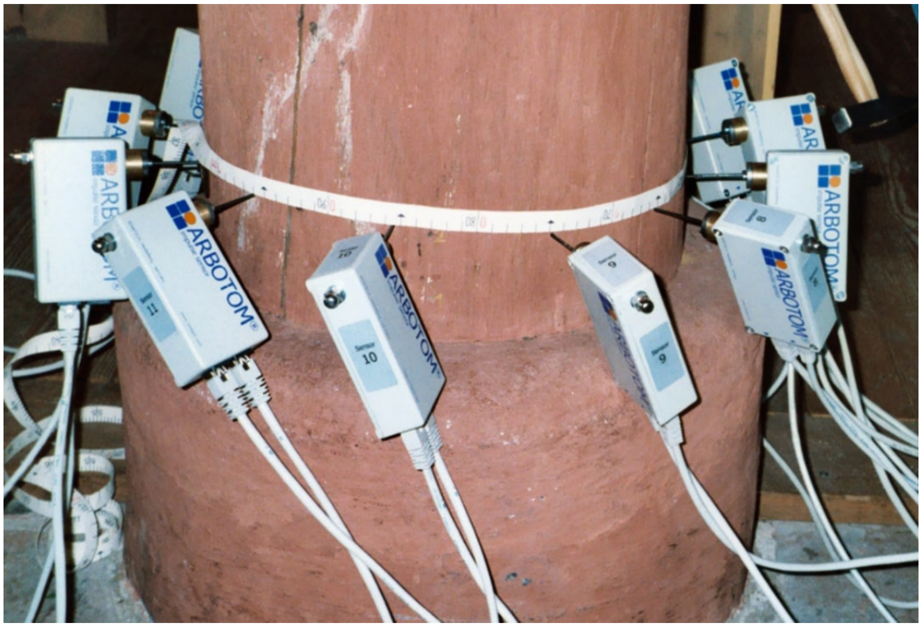

Figure 2.6: Configuration of Stress Wave Tomography Test Reprinted from Dackermann et al. (2014)

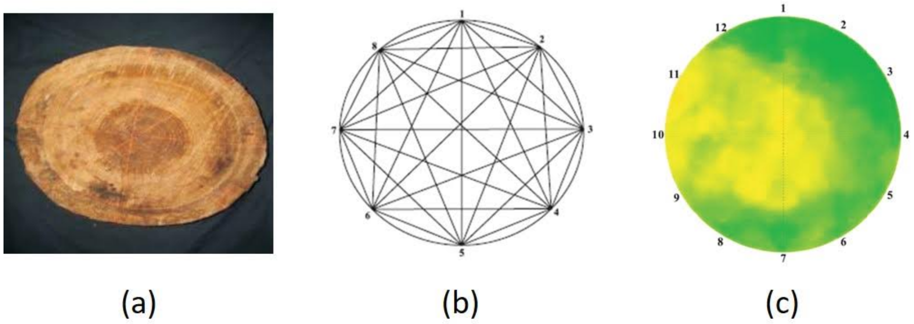

Figure 2.7: Stress Wave Tomography Reprinted from Lin et al. (2011) (a) Sectional Image of Wood Trunk, (b) Acoustic Wave Paths, and (c) Sectional Profile

The feasibility of the method has been verified on the identification of the location and the size of defects in trees in many studies (Rust, 2000; Gilbert and Smiley, 2004; Socco et al., 2004; Liang et al., 2008; Lin et al., 2008; Wang et al., 2009; França et al., 2013; Perlin et al., 2014). But, some drawbacks of the method were detected. The inaccuracy of the locational information of sensors can be potential error of the results (Rust, 2000). The area where wave paths are not densely passing like the near perimeter area has a low accuracy (Gilbert and Smiley, 2004). In addition, the inverse relationship between the wave frequency and the resolution is required as the high frequency wave does not have a high penetrating energy (Bucur, 2005). Also, elongated discontinuities like cracks and ring shakes were overestimated, and it is difficult to detect incipient decays and small size defects (Wang et al., 2009). Furthermore, the orthotropic behavior of the acoustic wave in woods affected the results (Perlin et al., 2014).

2.1.5.4 Ultrasonic Echo

Most non-destructive testing methods are based on capturing the transmitted wave, and it requires accessing both sides of the element. However, the ultrasonic echo technique can evaluate the element with one side access, which is more applicable for in-situ evaluation (Hasenstab et al., 2003). One of the ultrasonic echo transducers is presented in Figure 2.8. The transmitted wave signal penetrates the medium and is reflected at the back-walls or discontinuities. In the recorded signal plot in terms of time, which is called an A-scan, is shown in Figure 2.9. The location of damage can be identified if the wave velocity is known. Also, the combination of the A-scans along the movement of the transducer, which is called B-scan, is also shown in Figure 2.9. The B-scan gives the sectional image information of the specimen.

Figure 2.8: Ultrasonic Echo Sensor with Wooden Specimen

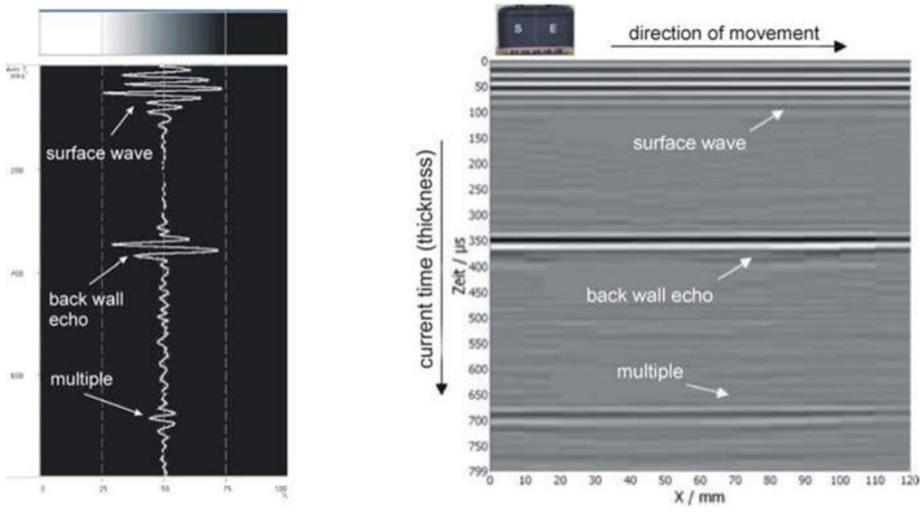

(a)

(b)

Figure 2.9: Ultrasonic Echo Reprinted from Maack and Krause (2008) (a) A-scan and (b) B-scan

Because B-scan images provide the intuitional information, various studies on the ultrasonic echo technique were conducted. Hasenstab et al. (2005) employed the ultrasonic echo technique to localize defects in the pine wood specimen. The damage area was reflected in the B-scan images, but it was found that the low frequency wave, which has a small absorption effect, should be used to minimize the attenuation of the signal. Maack and Krause (2008) applied the ultrasonic echo technique to the historical wooden church building, and Hasenstab and Osterloh (2009) carried out the ultrasonic echo technique on the glued laminated beam to detect damage.

2.1.5.5 Ultrasonic Array

Ultrasonic array techniques have been widely used on the concrete structure but rarely on the wooden structure. That is because of the fact that the image reconstruction algorithm, synthetic aperture focusing technique (SAFT) for timber structures has not been developed yet. Ultrasonic array consists of a number of ultrasonic transducers and receives several signals with a single scan. Basically, obtained raw signals are hard to be interpreted without prerequisite knowledge. Therefore, post processing is necessary to transform the obtained raw data into an understandable image data. That post processing algorithm is called SAFT. Generally, the SAFT algorithm assumes that the ultrasonic wave in the medium behaves in an isotropic manner due to the relatively small size of the concrete aggregates compared to the wavelength. In wood, however, the ultrasonic wave behaves much more in an orthotropic manner because of large annual rings. Therefore, a new type of SAFT algorithm with orthotropic properties is required to be applied to the timber inspection.

Krause et al. (2013) conducted the ultrasonic imaging technique on the structural timber elements using anisotropic SAFT algorithm. The SAFT algorithm in the study is a time-domain method and it uses group velocity information when reconstructing the image. The proposed algorithm was tested with the simulation data generated by the elastodynamic finite integration technique and the experimental data. Then this technique was applied to the real structure, a timber pedestrian bridge. The results have shown that the obtained reconstructed images were quite straightforward and easy to understand.

2.2 SAFT ALGORITHM

The SAFT is an image reconstruction algorithm that generates a sectional image using signal data from an ultrasonic array system (Stepinski and Lingvall, 2010). The algorithm provides a recognizable sectional image from obscure raw data.

An ultrasonic array system has an array of ultrasonic transducers and generates several raw signal data with a single scan. The measuring scheme of the ultrasonic array system is depicted in Figure 2.10.

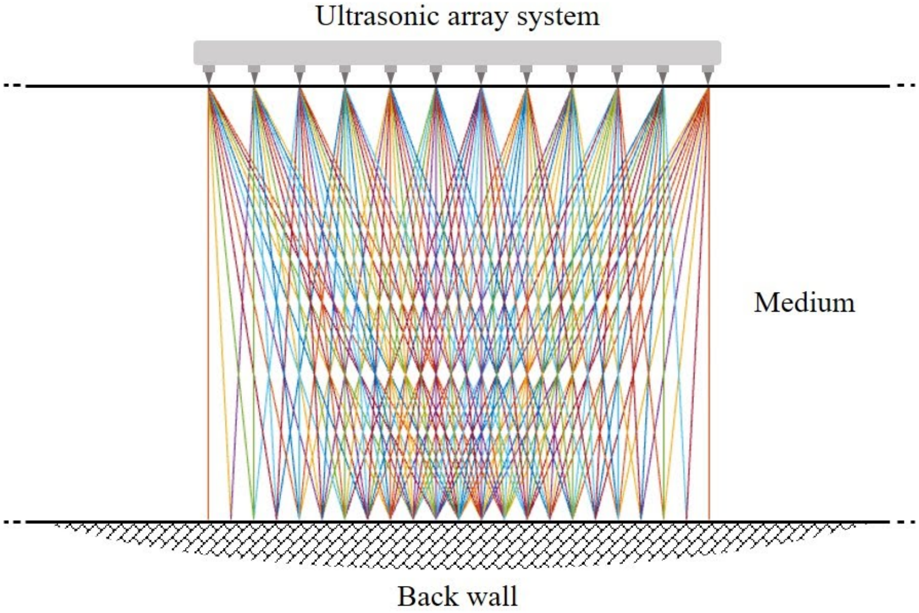

Figure 2.10: Ultrasonic Array System Measuring Scheme

The mathematical definition of the received signal data e is expressed as

$$e(t, x_T, x_R) = \int\int f(x, z)\delta(t - t_d)\mathrm{d}x\mathrm{d}z \tag{2.5}$$

where t is the time, x_T and x_R are the transmitter and the receiver locations, respectively, x and z are the horizontal and vertical locations of the target point, respectively, f is the reflectivity function, δ is the Dirac delta distribution and t_d is the delayed time which is defined as

$$t_d(x, z, x_T, x_R) = \frac{1}{c}\left(\sqrt{z^2 + (x - x_T)^2} + \sqrt{z^2 + (x - x_R)^2}\right) \tag{2.6}$$

where c is the propagating wave velocity depending on materials properties.

The reflectivity function f is heterogeneities in the cross section, which means that the function tells the shape of damage in the section. Because the SAFT algorithm calculates the damage field from the obtained signal data, the SAFT algorithm is called an inverse problem.

There are two different types of SAFT algorithms based on the domain. One is the time-domain SAFT algorithm that utilizes the signal data in the time-domain. The algorithm is also called the delay-and-sum method. This method calculates the value at a certain pixel point by adding up all values in the obtained signal data at the corresponding delayed time. The algorithm is straightforward and simple, but a lot of computation time and a large amount of memory is required. The other is the frequency-domain SAFT algorithm that exploits the signal data in the frequency-domain. The algorithm is based on the strict mathematical background and guarantees a fast computational speed if a high-performance processor is used. The flowcharts of both algorithms are shown in Figure 2.11.

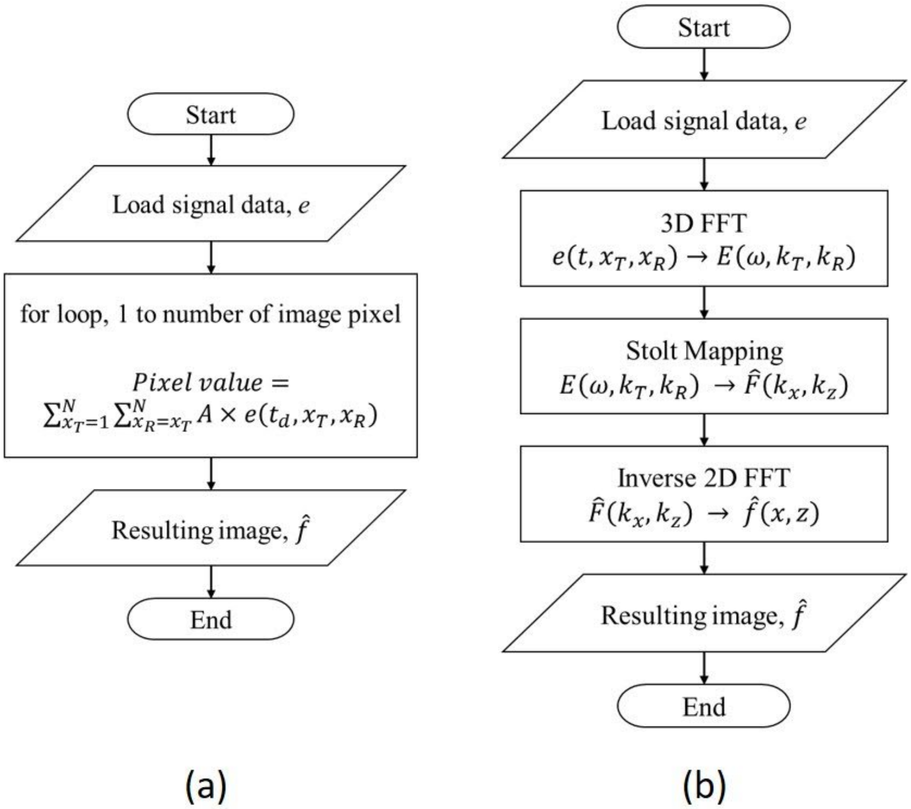

Figure 2.11: Flowchart of Time-Domain SAFT Algorithm (left) and Frequency-Domain SAFT Algorithm (right)

2.2.1 Time-Domain SAFT Algorithm

The imaging geometry for the time-domain SAFT algorithm is shown in Figure 2.12. A value at each pixel is calculated by combining values from all signal pairs at the corresponding delayed time t_d.

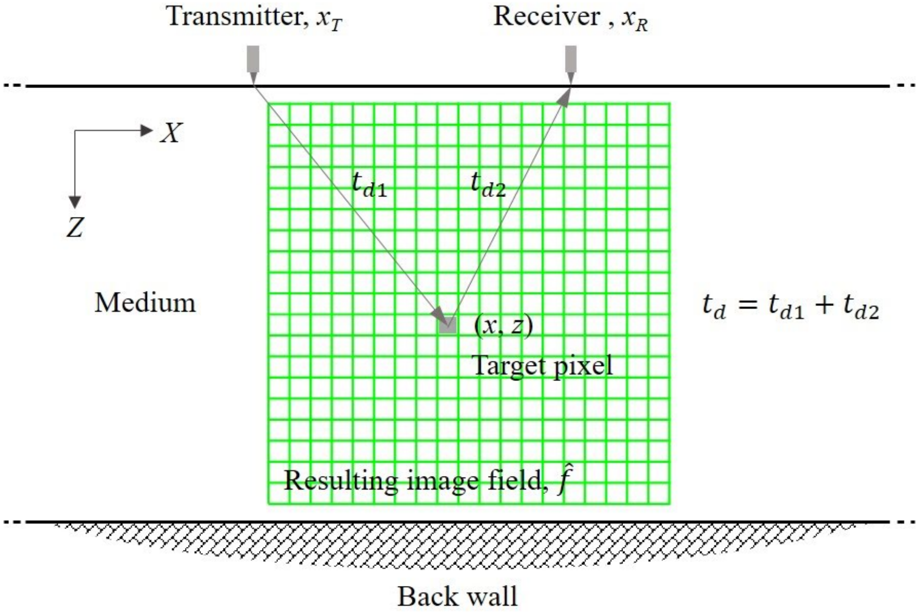

Figure 2.12: Imaging Geometry of Time-Domain SAFT Algorithm

The resulting image $\hat{f}$ of the algorithm is defined as

$$\hat{f}(x,z) = \sum_{x_T=1}^{N} \sum_{x_R=x_T}^{N} A(x,z,x_T,x_R)e(t_d,x_T,x_R) \tag{2.7}$$

where A is a weighting factor called the apodization factor that improves the lateral resolution of the resulting image by weakening values at large angle (Skjelvareid, 2012). Although there are various types of apodization factors, a Hann window is used in this dissertation. The equation of the apodization factor is represented as

$$A(x,z,x_T,x_R) = \alpha_{Hann}(x,z,x_T) \times \alpha_{Hann}(x,z,x_R) \tag{2.8}$$

$$\alpha_{Hann}(x,z,x^*) = \begin{cases} \frac{1}{2}[1+\cos(2\pi\hat{x})], & |\hat{x}| < \frac{1}{2} \\ 0, & otherwise \end{cases} \tag{2.9}$$

where $\hat{x} = (x - x^*)/\Delta x(z)$ is normalized X coordinates, $\Delta x(z) = 2z\tan(\Delta\theta/2)$, and $\Delta\theta$ is the angular beam width of the transducer. The illustration of the apodization factor is shown in Figure 2.13.

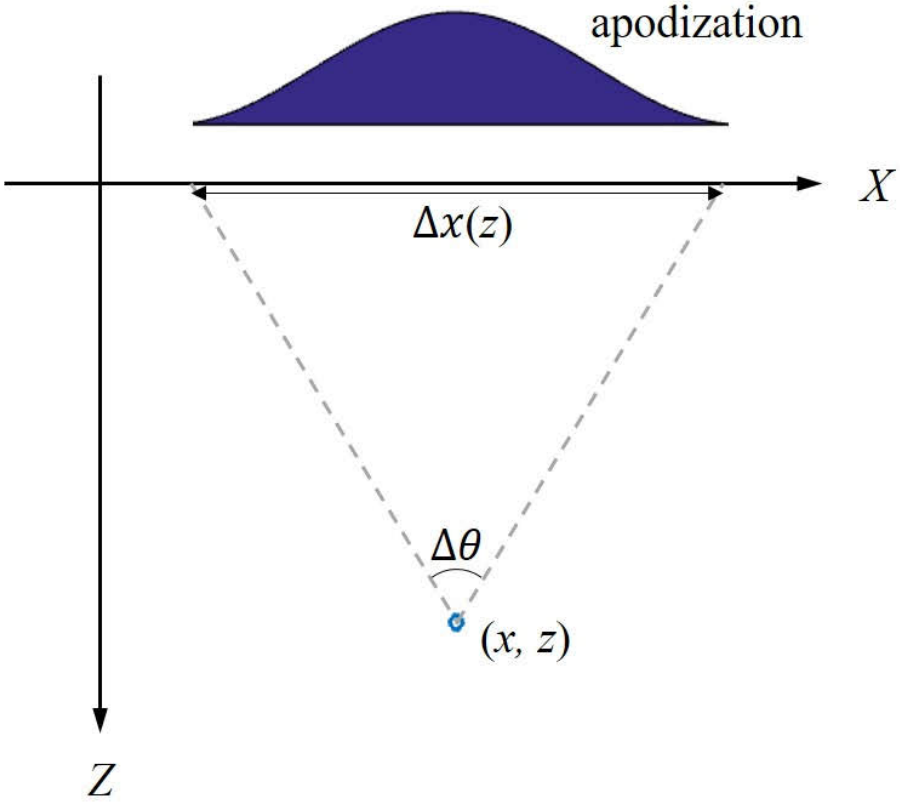

Figure 2.13: Illustration of Apodization Factor

Although the apodization factor increases the lateral resolution of a resulting image, it narrows down the scope of a detectable area to the area just below an ultrasonic array. In order to analyze the pure performance of SAFT algorithm, the apodization factor in this study is assumed as one.

The time-domain SAFT algorithm for orthotropic media is similar to the time-domain SAFT algorithm for isotropic media. The only difference between the two algorithms is the wave velocity. If the media is orthotropic, the wave velocity c in Equation (2.6) of the delayed time t_d will be varying along the direction.

2.2.2 Wave Velocity in Orthotropic Media

Unlike a constant wave velocity in an isotropic media, a wave in orthotropic media has a changing velocity along the propagation direction. There are two types of wave velocities in orthotropic media: phase velocity and group velocity. The phase velocity is the speed of the wave orthogonal to the wavefront, and the group velocity is the speed of the energy propagation (Tsvankin, 2012) as shown in Figure 2.14. Because the shape of the wavefront is not spherical in orthotropic media, phase and group velocities are not identical. Since the delayed time t_d in Equation (2.6) is the traveling time along the wave path from the wave source to the receiver, the group velocity should be used for the wave velocity c in the time-domain SAFT algorithm for orthotropic media.

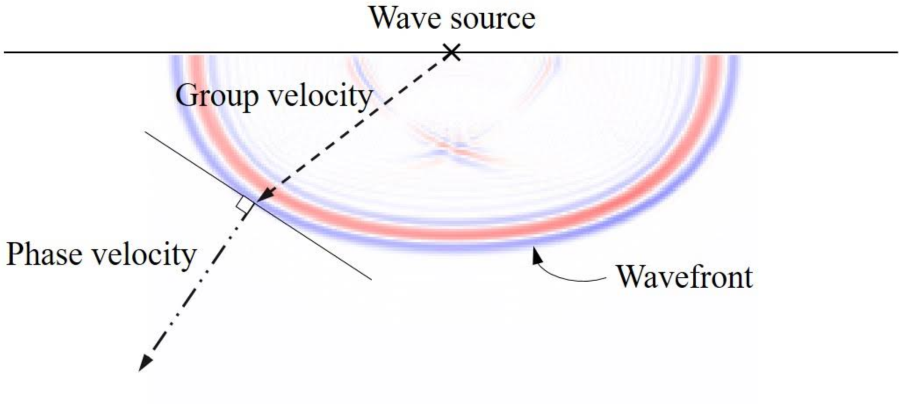

Figure 2.14: Phase and Group Velocity in Orthotropic Media

2.2.3 Group Velocity

The group velocity can be calculated from the phase velocity function which is obtained from the wave equation (Tsvankin, 2012). The homogeneous anisotropic wave equation is given as

$$\rho\frac{\partial^2 u_i}{\partial t^2} - c_{ijkl}\frac{\partial^2 u_k}{\partial x_j \partial x_l} = 0 \tag{2.10}$$

where ρ is the density, u is the displacement, t is the time, c is the stiffness tensor, and x is the Cartesian coordinate.

In order to solve the homogeneous anisotropic wave equation, we can plug the steady-state plane wave representation into Equation (2.10). The steady-state plane wave can be written as

$$u_k = U_k e^{i\omega(n_j x_j/V - t)} \tag{2.11}$$

where U is the polarization, ω is the angular frequency, n is the unit vector perpendicular to the wave front, and V is the phase velocity.

Plugging Equation (2.11) into Equation (2.10) leads to the so-called Christoffel equation expressed by

$$\begin{bmatrix} C_{11}-\rho V^2 & C_{12} & C_{13} \\ C_{21} & C_{22}-\rho V^2 & C_{23} \\ C_{31} & C_{32} & C_{33}-\rho V^2 \end{bmatrix} \begin{bmatrix} U_1 \\ U_2 \\ U_3 \end{bmatrix} = 0 \tag{2.12}$$

where C_{ik} is the so-called Christoffel matrix that is defined by

$$C_{ik} = c_{ijkl} n_j n_k \tag{2.13}$$

This is the eigenvalue problem that can be directly solved if $\det[C_{ik} - \rho V^2 \delta_{ik}] = 0$. For orthotropic media, the stiffness matrix is written as

$$c = \begin{bmatrix} c_{11} & c_{12} & c_{13} & 0 & 0 & 0 \\ c_{21} & c_{22} & c_{23} & 0 & 0 & 0 \\ c_{31} & c_{32} & c_{33} & 0 & 0 & 0 \\ 0 & 0 & 0 & c_{44} & 0 & 0 \\ 0 & 0 & 0 & 0 & c_{55} & 0 \\ 0 & 0 & 0 & 0 & 0 & c_{66} \end{bmatrix} \tag{2.14}$$

Therefore, the Christoffel matrix for orthotropic media becomes

$$C_{11} = c_{11}n_1^2 + c_{66}n_2^2 + c_{55}n_3^2 \tag{2.15}$$

$$C_{22} = c_{66}n_1^2 + c_{22}n_2^2 + c_{44}n_3^2 \tag{2.16}$$

$$C_{33} = c_{55}n_1^2 + c_{44}n_2^2 + c_{33}n_3^2 \tag{2.17}$$

$$C_{23} = (c_{23} + c_{44})n_2n_3 \tag{2.18}$$

$$C_{13} = (c_{13} + c_{55})n_1n_3 \tag{2.19}$$

$$C_{12} = (c_{12} + c_{66})n_1n_2 \tag{2.20}$$

where the tensor notation is transformed into the matrix form according to the Voigt notation.

In SAFT algorithm, a 2D wave propagation is considered. If the wave is constrained in the $x_1 - x_3$ plane ($n_2 = 0$), the Christoffel equation becomes

$$\begin{bmatrix} c_{11}n_1^2 + c_{55}n_3^2 - \rho V^2 & 0 & (c_{13} + c_{55})n_1n_3 \\ 0 & c_{66}n_1^2 + c_{44}n_3^2 - \rho V^2 & 0 \\ (c_{13} + c_{55})n_1n_3 & 0 & c_{55}n_1^2 + c_{33}n_3^2 - \rho V^2 \end{bmatrix} \begin{bmatrix} U_1 \\ U_2 \\ U_3 \end{bmatrix} = 0 \tag{2.21}$$

In this form, Equation (2.21) can be divided into two individual equations: shear horizontal wave (SH-wave, $U_1 = U_3 = 0$) and pressure and shear vertical wave (P- and SV-wave, $U_2 = 0$). By representing unit vector n with respect to the phase angle θ ($n_1 = \sin\theta$ and $n_3 = \cos\theta$) as shown in Figure 2.14, two individual equations are obtained.

For SH-wave,

$$\begin{bmatrix} c_{66}\sin^2\theta + c_{44}\cos^2\theta - \rho V^2 \end{bmatrix} \begin{bmatrix} U_2 \end{bmatrix} = 0 \tag{2.22}$$

For P- and SV-wave,

$$\begin{bmatrix} c_{11}\sin^2\theta + c_{55}\cos^2\theta - \rho V^2 & (c_{13}+c_{55})\sin\theta\cos\theta \\ (c_{13}+c_{55})\sin\theta\cos\theta & c_{55}\sin^2\theta + c_{33}\cos^2\theta - \rho V^2 \end{bmatrix} \begin{bmatrix} U_1 \\ U_3 \end{bmatrix} = 0 \tag{2.23}$$

In order to avoid a trivial solution, letting $\det[C_{ik} - \rho V^2 \delta_{ik}] = 0$ yields the phase velocities of each mode.

The phase velocity of SH-wave is

$$V_{SH}(\theta) = \sqrt{\frac{c_{66}\sin^2\theta + c_{44}\cos^2\theta}{\rho}} \tag{2.24}$$

The phase velocities of P- and SV-wave are

$$\begin{aligned} V^2(\theta) = \frac{1}{2\rho}\Bigg[&(c_{11}+c_{55})\sin^2\theta + (c_{33}+c_{55})\cos^2\theta \\ &\pm \sqrt{[c_{11}-c_{55})\sin^2\theta - (c_{33}-c_{55})\cos^2\theta]^2 + 4(c_{13}+c_{55})\sin^2\theta\cos^2\theta}\Bigg] \end{aligned} \tag{2.25}$$

where the plus sign in front of the square root means the P-wave, and the minus sign means the SV-wave.

The group velocities can be obtained in terms of the phase velocity V, the phase angle θ, and the group angle ψ (Tsvankin, 2012):

$$V_{G-SH} = \frac{V_{S0}\sqrt{1+2\gamma}}{\sqrt{1+2\gamma\cos^2\psi}} \tag{2.26}$$

$$V_{G-P,SV} = \sqrt{V^2 + (\mathrm{d}V/\mathrm{d}\theta)^2} \tag{2.27}$$

where $V_{S0} = \sqrt{c_{44}/\rho}$ is the vertically propagating SH-wave ($\theta = 0°$), $\gamma = (c_{66} - c_{44} = 2c_{44})$ is the anisotropic parameter, and the relationship between the phase angle θ and the group angle ψ is defined by

$$\tan\psi = \frac{\tan\theta + \dfrac{1}{V}\dfrac{\mathrm{d}V}{\mathrm{d}\theta}}{1 - \dfrac{\tan\theta}{V}\dfrac{\mathrm{d}V}{\mathrm{d}\theta}} \tag{2.28}$$

2.2.4 Frequency-Domain SAFT Algorithm for Isotropic Media

The frequency-domain SAFT algorithm for isotropic media is derived based on the wavenumber algorithm using full matrix data (Hunter et al., 2008). The crucial part of the algorithm is transforming signal data from the measuring domain to resulting image domain. The transforming relation between the domains is derived from the mathematical definition of the signal data.

Signal data e is thought as the superposition of point reflection signals.

$$E(\omega, x_T, x_R) = \int_{-\infty}^{\infty}\int_{-\infty}^{\infty} f(x,z)G(\omega, x - x_T, z)G(\omega, x - x_R, z)\mathrm{d}x\mathrm{d}z \tag{2.29}$$

where E is the Fourier transform of signal data e with respect to time, f is the reflectivity function, and $G(\omega, r) = \frac{-i}{4}H_0^{(2)}(\omega r/c)$ is the 2D free space inward Green's function. The Green's function can be expressed in the decomposed form by Weyl's identity (Chew, 1995) as

$$G(\omega, x, z) = \frac{-i}{4\pi} \int_{-\infty}^{\infty} \frac{\exp(ik_x x - i|z|\sqrt{k^2 - k_x^2})}{\sqrt{k^2 - k_x^2}} \mathrm{d}k_x \tag{2.30}$$

where k_x and k_z are the wavenumbers in the x and z axis, respectively, and the dispersion relationship is $k^2 = \frac{\omega^2}{c^2} = k_x^2 + k_z^2$.

Substituting Equation (2.30) into Equation (2.29) yields to

$$\begin{aligned} E(\omega, x_T, x_R) = \frac{-1}{(4\pi)^2} \int_{-\infty}^{\infty} \int_{-\infty}^{\infty} \Bigg(\frac{\exp(ik_T x_T + ik_R x_R)}{\sqrt{k^2 - k_T^2}\sqrt{k^2 - k_R^2}} \Bigg[\int_{-\infty}^{\infty} \int_{-\infty}^{\infty} f(x, z) \\ \cdot \exp\Bigg(- ix(k_T + k_R) - i|z| \Bigg(\sqrt{k^2 - k_T^2} + \sqrt{k^2 - k_R^2} \Bigg) \Bigg) \Bigg] \mathrm{d}x\mathrm{d}z \Bigg) \mathrm{d}k_T \mathrm{d}k_R \end{aligned} \tag{2.31}$$

where k_T and k_R are the wavenumbers in the transmitter and receiver axis.

The expression in the square bracket in Equation (2.31) can be recognized as the 2D spatial Fourier transform of the reflectivity function. Taking the Fourier transform of Equation (2.31) in terms of x_T and x_R yields

$$E(\omega, k_T, k_R) = \frac{-F\left(k_T + k_R, \sqrt{k^2 - k_T^2} + \sqrt{k^2 - k_R^2}\right)}{(4\pi)^2 \sqrt{k^2 - k_T^2}\sqrt{k^2 - k_R^2}} \tag{2.32}$$

From Equation (2.32), the mapping relation for isotropic media can be derived.

$$k_x = k_T + k_R \tag{2.33}$$

$$k_z = \sqrt{k^2 - k_T^2} + \sqrt{k^2 - k_R^2} \tag{2.34}$$

The wavenumber k_z resulting from Equation (2.34) is nonlinearly distributed unlike k_T and k_R as shown in Figure 2.15. For FFT or inverse FFT, input data should be linearly distributed. Thus, the interpolation method so-called Stolt mapping is needed to distribute k_z data linearly.

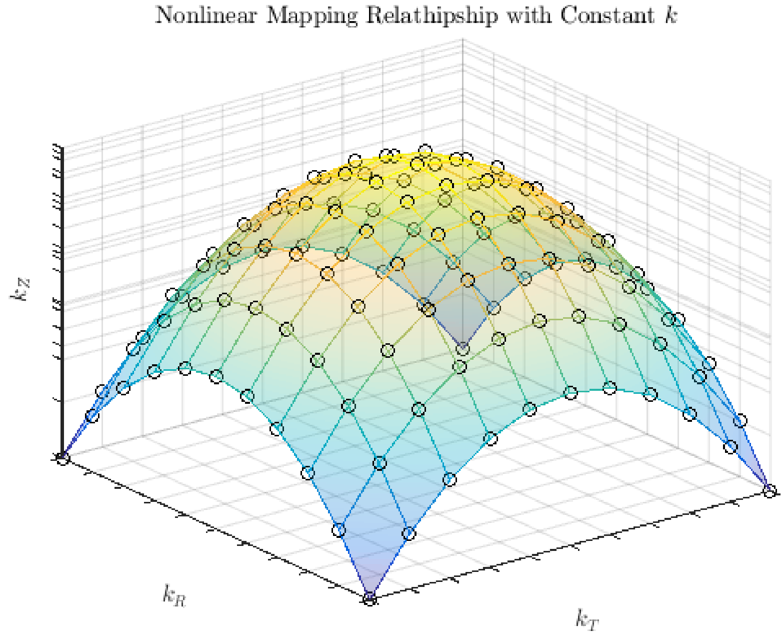

Figure 2.15: Nonlinear Mapping Relationship between k_T, k_R, and k_z with Constant k

Since the transformation is from three arguments to two arguments, it is ill-determined. Therefore, the transformation is conducted with holding one of the parameters constant, e.g., k_T, resulting to

$$F(k_x, k_z|k_T) = -(4\pi)^2\sqrt{k^2 - k_T^2}\sqrt{k^2 - k_R^2}E(\omega, k_R|k_T) \tag{2.35}$$

The Fourier transform of the reflectivity function can be obtained by integrating the two dimensional slice along in terms of k_T values.

$$F(k_x, k_z) = \int_{-\infty}^{\infty} F(k_x, k_z | k_T) \mathrm{d}k_T \tag{2.36}$$

Finally, the resulting image $\hat{f}$ is obtained by performing the inverse Fourier transform of Equation (2.36).

$$\hat{f} = \frac{1}{(2\pi)^2} \int_{-\infty}^{\infty} \int_{-\infty}^{\infty} F(k_x, k_z) \exp(ik_x x + ik_z z) \mathrm{d}k_x \mathrm{d}k_z \tag{2.37}$$

2.3 STRUCTURAL WOOD PRODUCTS

Wood is strong, renewable, durable, and inexpensive enough for structural usage. Thus, various types of products have been developed and utilized to construct buildings. However, problems of wood such as its variability and vulnerability to environmental conditions should be properly handled before use in order for wood products to have required mechanical strength (Stalnaker and Harris, 1997). In this section, wood specimens types and wood processing methods are explained. Then, the structural wood products and a target wood component for this study are described.

2.3.1 Wood Species Types

Many different wood species are being used as structural wood products and can be categorized into two groups: softwood and hardwood. Softwood is coniferous while hardwood is deciduous. However, these terminologies are not necessarily a description of the mechanical properties of the wood (Breyer et al., 1999). The majority of structural wood components are made of softwood (Ozelton and Baird, 2006). Hardwood is used in limited applications such as harbor works, restoration works, farm building, etc.

2.3.2 Cutting Patterns

Lumber may be cut from a log in three different patterns as shown in Figure 2.16. The only difference between patterns is the orientation of growth rings relative to the wide face of a wood piece.

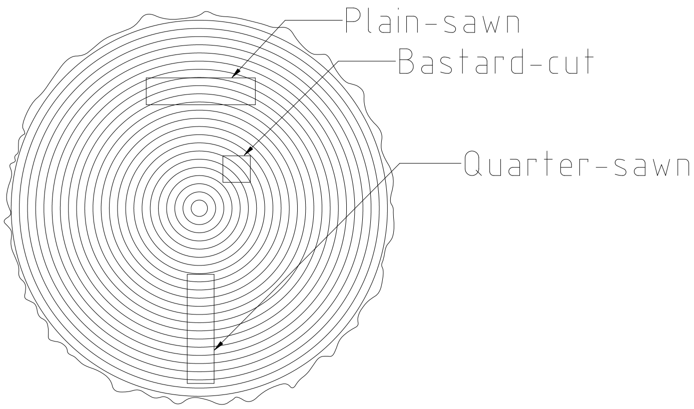

Figure 2.16: Wood Cutting Patterns: Plain-sawn, Quarter-sawn, and Bastard Cut

The most important effect of these patterns on the wood piece is the shrinkage or warping from a structural perspective. The shrunk shapes of three wood cutting patterns with the loss of moisture content are depicted in Figure 2.17. A shrinkage in lumber is larger in a direction parallel to the growth rings than in any other direction. As a result, the plain-sawn piece is distorted noticeably as it dries because the growth rings are not exactly parallel or square to the surfaces. The quarter-sawn piece, on the other hand, shows little distortions on short edges. The bastard-cut piece is deformed in a diamond-shape.

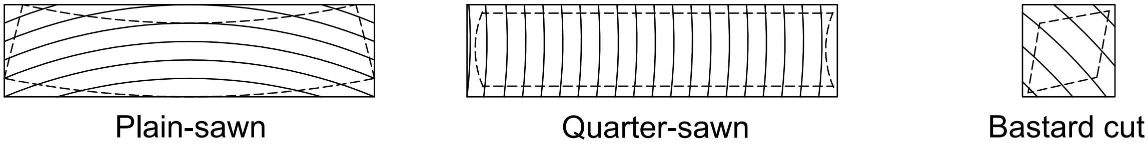

Figure 2.17: Shrunken Shape after Drying: Plain-sawn (left), Quarter-sawn (middle), and Bastard Cut (right)

Although the quarter-sawn pattern is the best selection for structural components, the most popular cutting pattern is the plain-sawn (Stalnaker and Harris, 1997). In Figure 2.18, two common methods for cutting logs are presented. Another cutting method may be a combination of these two methods. To create as much quarter-sawn lumber as possible from a log, the log has to be turned frequently, and much waste is generated. This causes additional work steps, increased costs, and reduced yield.

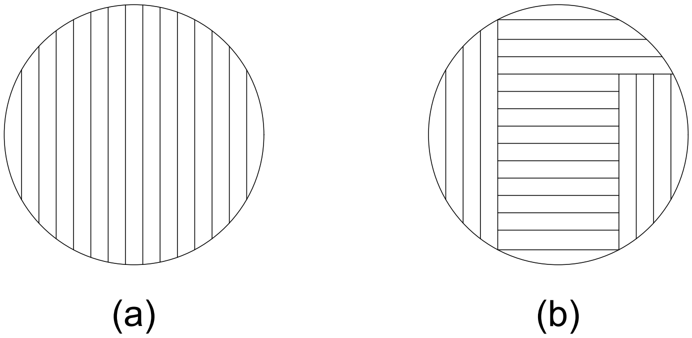

Figure 2.18: Two Common Sawing Patterns

2.3.3 *Treatments*

For wood products to have strength enough to support structural load demands without environmental impacts, it is crucial to prevent the wood from being destroyed by several different instruments such as decay, termites, marine borers, fire, etc. Thus, proper treatment should be a priority.

One of the important wood treatments is drying. Since the moisture content is an important factor that influences the strength as well as shrinkage and decay, drying the wood can prevent such phenomena resulting from the high moisture content. The size of the wood becomes decreased as the wood dries, and the decay by fungi can be prevented by letting the moisture content of the wood below approximately 18 percent, which is known as the dry state (Breyer et al., 1999). Figure 2.19 describes the relationships between the longitudinal compressive strength of timber and moisture content. If the moisture content in a timber element is above 25 percent also known as the green state, the timber element will lose its strength significantly. Conversely, the strength of the timber element will increase as the moisture content drops down to 18 percent.

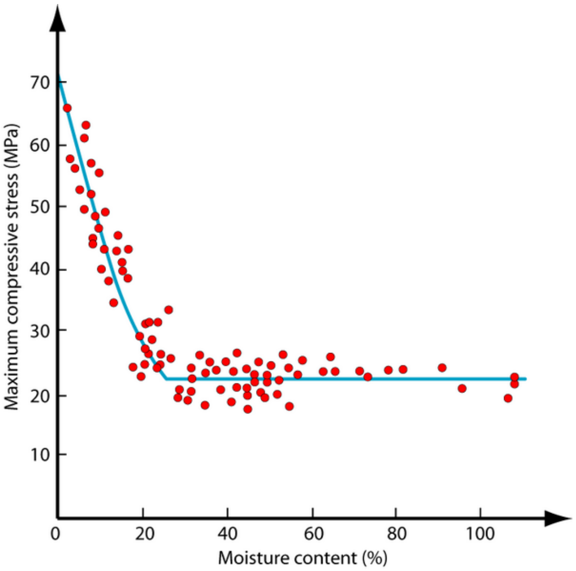

Figure 2.19: Relationship between Compressive Longitudinal Strength of Timber and Moisture Content Reprinted from Dinwoodie (1975)

Two popular methods for wood drying are air-drying and kiln-drying (or oven drying). The air-drying method stacks the sawn-timber on a raised foundation in a clean, cool, dry and shady place as shown in Figure 2.20(a). This method is less expensive and produces a high-quality wood product. However, it is strongly influenced by the climate and can take several months to many years to dry the wood. The kiln-drying is an artificial drying method that uses an oven called kiln to dry the wood as shown in Figure 2.20(b). This method applies specific environmental conditions to the wood with a deliberate control of temperature, relative humidity, and air circulation. Although this method is expensive, most wood production mills use the kiln-drying method because of the short drying time.

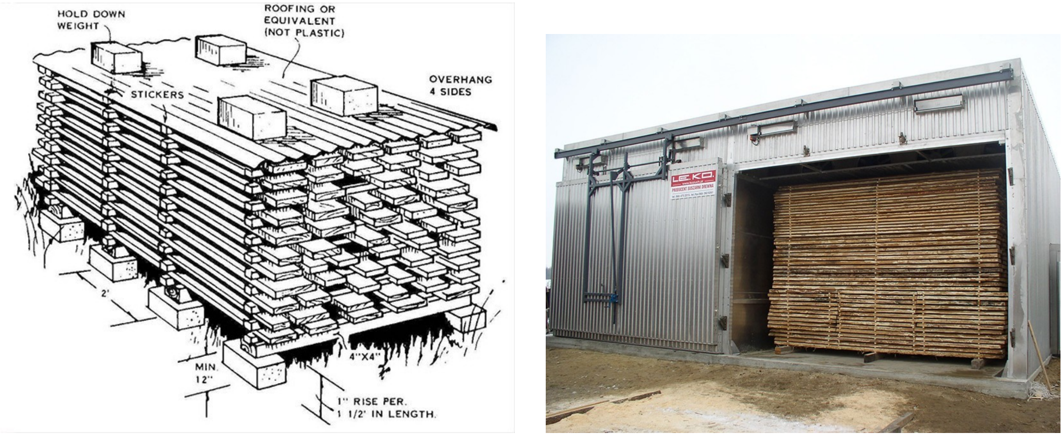

(a) (b)

Figure 2.20: Two Common Wood Drying Processes Reprinted from Nicholson (2013) (a) Air Drying and (b) Kiln Drying

Another treatment for the wood products is adding preservatives. Three basic types of preservatives are creosote, oilborne treatments, and waterborne salts. There are many preservatives in the last two categories, and the selection of preservative type is determined by the application.

The most common method to add preservatives is the pressure process. The wood products filled with preservatives are exposed to extreme conditions such as high temperature, vacuum, and high load pressure. This allows the preservatives to penetrate deeply. Also, the non-pressure process exists. This treatment can be applied if the demands on wood products are not directly related to structural safety and the exposed weather condition is not harsh. This method uses putting the wood products in a bathtub or spray/brush to apply preservatives to the surface. This does not allow a great penetration of the preservatives but shows enough effectiveness.

An additional way to treat the wood is densifying for increasing the strength. After the chemical treatment, the wood is mechanically hot-pressed at 100°C. The illustration of wood densification is shown in Figure 2.21. This leads to a reduction in thickness of about 80 percent and an increment of the strength of about 1,000 percent (Song et al., 2018). Even though the consequences of this treatment are quite exceptional, the densifying method for a large scale with fast speed is not established yet. Additional research for this issue is required.

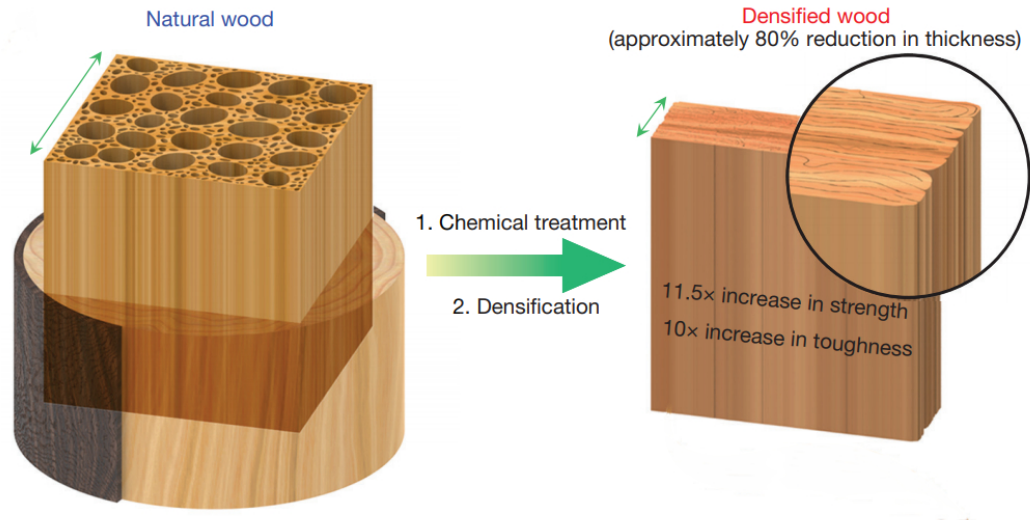

Figure 2.21: Illustration of Wood Densification Reprinted from Song et al. (2018)

2.3.4 Structural Wood Products Types

Wood products generally used in the structural field are listed in Table 2.1, and popular structural wood products are shown in Figure 2.22. Lumber and plywood are wood products that have been widely used in building construction during the 20th century as a result of their inexpensiveness. As the demand for a wood product with reliable quality has increased, other types of wood products that reduce the uncertainty in strength properties have been developed (Moody and Ritter, 1990). One of the wood products is the laminated timber, which is made of multiple layers of lumber. Since it is fabricated from multiple pieces of fine lumber, it has a flexible size and enough strength to be used as a structural element. The laminated timber product has become more competitive than other construction materials like steel and concrete as a result of the decreased manufacturing cost of laminated timber products and skillful marketing strategies by timber product companies (Abbott and Whale, 1987).

However, despite increased usages of wood products in construction, research about preventing failure in timber structures has not been fully conducted yet. According to the comprehensive failure analysis report by Frese and Blaß (2011), nearly 90 percent of damaged elements among collapsed timber structures in Germany in 2006 were comprised of glulam, a laminated timber product. Therefore, evaluating laminated timber products might be essential.

Table 2.1: Wood Products in Structural Field

Name	Description
Lumber	Sawn lumber having rectangular shape, which is cut from wood logs. Based on the cutting orientation, lumber is divided into plain and quarter sawn lumber. Plain sawn lumber has annual rings parallel to the face of the board, and quarter sawn lumber has annual rings perpendicular to the face of the board
Plywood	Wood board consists of layers of wood veneers that are glued together. Grain of each layer is cross-glued to adjacent layers
Pole	Round timber that is the most close to the original shape of wood. It is just debarked, treated with preservation, and cut in length
Particleboard	Wood board manufactured from shavings, particles, wood chips and even sawdust with adhesive
Laminated Wood	Engineered wood product that comprises layers of wood products. The difference with the plywood is that grains of each layer in laminated wood have the same orientation. Due to its reliable strength, it could be utilized as beam and column for multi-story buildings

2.4 TECHNICAL NEEDS

There are many studies about developing the SAFT algorithm for isotropic media, but little research about the SAFT algorithm for orthotropic media was conducted. Among the studies about the SAFT algorithm for orthotropic media, the SAFT

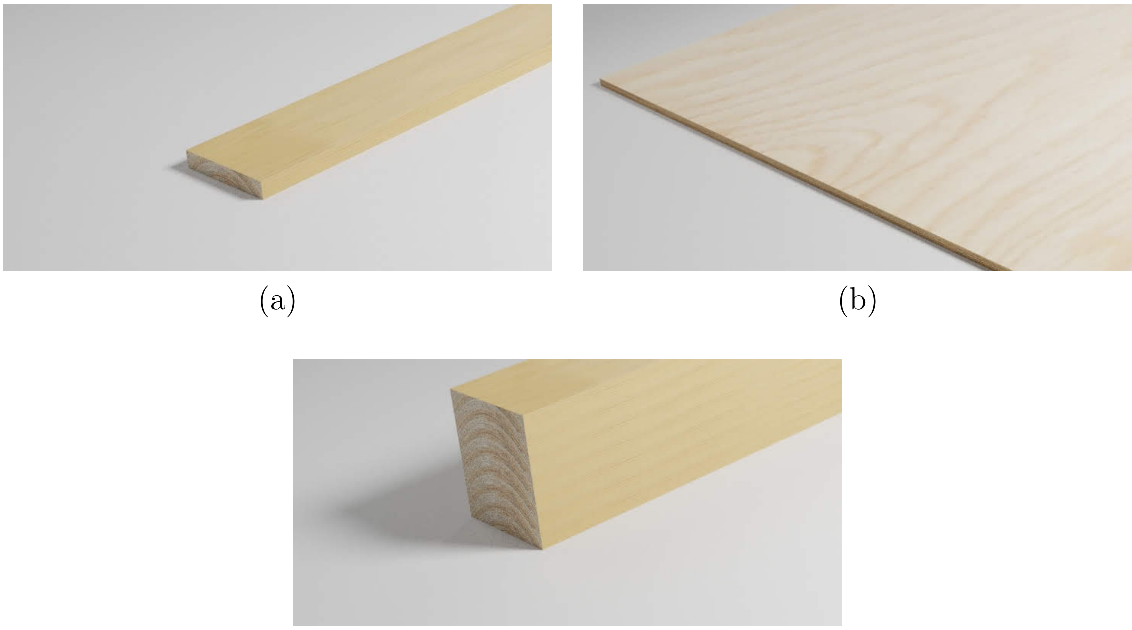

(a)

(b)

(c)

Figure 2.22: Popular Structural Wood Products (a) Lumber, (b) Plywood, and (c) Glulam

algorithm in frequency-domain, which is available for an in-situ timber structure inspection method, has not been studied yet.

The frequency-domain algorithm which has a fast computational speed for orthotropic media has to be developed. Since the algorithm has not been derived yet and will be realized using the programming language MATLAB where discrete numbers are used and truncation errors exist, the strict mathematical derivation of the algorithm has to be performed.

In addition, the algorithm has to calculate a resulting image within a couple of seconds. An ultrasonic array device investigates a single section with a single scan, and it requires multiple scans to inspect the entire range of the specimen. Therefore, a short computational time is essential for in-situ inspection methods for the ultrasonic array system to estimate the structure.

Furthermore, the technique has to have enough detectable depth to inspect a timber element. The transverse ultrasonic wave signal can be significantly attenuated if the timber element inherently has many air voids or high moisture content. Also, the longitudinal ultrasonic wave that can propagate in a liquid or gas can yield an unrecognizable image if noise is severe. Thus, post-processing of the signal data is suggested if the signal has a lot of noise.

3. FREQUENCY-DOMAIN SAFT ALGORITHM FOR ORTHOTROPIC MEDIA

The difference between the frequency-domain SAFT algorithm for orthotropic and isotropic media is the solution of the wave equation, Green's function. The Green's function for anisotropic media is given by Tsvankin (2012) and is presented by

$$G_{ortho}(\omega, \mathbf{X}) = \frac{1}{(2\pi)^3\omega^2}\int_{-\infty}^{\infty} \mathbf{H}^{-1}\mathbf{F}e^{-i\mathbf{k}x}\mathrm{d}\mathbf{k} \tag{3.1}$$

where H is the matrix related to the Christoffel matrix C_{ik} with the relation $H_{ik} = C_{ik}/V^2 - \rho\delta_{ik}$, $\mathbf{F}$ is the force vector, and $\mathbf{k}$ is the wavenumber vector.

Reducing Equation (3.1) as a superposition of plane-wave solutions of the homogeneous wave equation leads to

$$G_{ortho}(\omega, \mathbf{X}) = \frac{-i\omega}{4\pi^2}\sum_{\nu=1}^{3}\int_{-\infty}^{\infty}\int_{-\infty}^{\infty} \mathbf{U}^{(\nu)}(p_1, p_2)e^{-i\omega(p_1x_1+p_2x_2+p_3^{(\nu)}x_3)}\mathrm{d}p_1\mathrm{d}p_2 \tag{3.2}$$

with

$$\mathbf{U}^{(\nu)}(p_1, p_2) = res\left[\frac{1}{D(p_3)}\mathbf{H}^{ad}\mathbf{D}\right]_{p_3^{(\nu)}} \tag{3.3}$$

where $\mathbf{H}^{ad}$ is the adjoint matrix of $\mathbf{H}$, $D(p_3) = \det[H_{ik}]$, and $p_3^{(\nu)}$ are the poles of the internal kernel in Equation (3.1).

For the SAFT algorithm which has a 2-D coordinate ($x_1 - x_3$ plane, $x_2 = p_2 = k_2 = 0$), Equation (3.2) can be reduced to

$$G_{ortho}(\omega,\mathbf{X}) = \frac{-\,i\omega}{4\pi^2}\sum_{\nu=1}^{3}\int_{-\infty}^{\infty}\mathbf{U}^{(\nu)}(p_1,0)e^{-i\omega(p_1x_1+p_3^{(\nu)}x_3)}\mathrm{d}p_1 \tag{3.4}$$

or

$$G_{ortho}(\omega,\mathbf{X}) = \frac{-\,i}{4\pi^2}\sum_{\nu=1}^{3}\int_{-\infty}^{\infty}\mathbf{U}^{(\nu)}(k_1,0)e^{-i\omega(k_1x_1+k_3^{(\nu)}x_3)}\mathrm{d}k_1 \tag{3.5}$$

with $p = k/\omega$.

Inserting Equation (3.5) into Equation (2.29) results to

$$\begin{aligned} &E(\omega,x_T,x_R) = \\ &\qquad \frac{-\,1}{\left((4\pi)^2\right)^2}\int_{-\infty}^{\infty}\int_{-\infty}^{\infty}\Bigg[\mathbf{U}^{(\nu)}(k_T,0)\mathbf{U}^{(\nu)}(k_R,0)\exp(ik_Tx_T+ik_Rx+R) \\ &\cdot\left(\int_{-\infty}^{\infty}\int_{-\infty}^{\infty}f(x,z)\exp(-i(k_T+k_R)x_1-i(k_{3,T}^{(\nu)}+k_{3,R}^{(\nu)})x_3)\mathrm{d}x\mathrm{d}z\right)\Bigg]\mathrm{d}k_T\mathrm{d}k_R \end{aligned} \tag{3.6}$$

Recognizing the big round bracket in Equation (3.6) as a Fourier transform of the scatter distribution $F(k_x,k_z)$ and taking a Fourier transform with respect to x_T and x_R yields

$$E(\omega,x_T,x_R) = \frac{-\,1}{\left((4\pi)^2\right)^2}\mathbf{U}^{(\nu)}(k_T,0)\mathbf{U}^{(\nu)}(k_R,0)F\left(k_T+k_R,k_{3,T}^{(\nu)}+k_{3,R}^{(\nu)}\right) \tag{3.7}$$

From Equation (3.7), the mapping relation for orthotropic media can be derived.

$$k_x = k_T + k_R \tag{3.8}$$

$$k_z = k_{3,T}^{(\nu)} + k_{3,R}^{(\nu)} \tag{3.9}$$

Since it is an ill-determined problem as well, the transformation of the coordinates is conducted slice by slice as described in Section 2.2.4.

$$F(k_x, k_z|k_T) = \frac{-\,(4\pi)^2}{\mathbf{U}^{(\nu)}(k_T, 0)\mathbf{U}^{(\nu)}(k_R, 0)} E(\omega, k_R|k_T) \tag{3.10}$$

$$F(k_x, k_z) = \int_{-\infty}^{\infty} F(k_x, k_z|k_T)\mathrm{d}k_T \tag{3.11}$$

Finally, the resulting image $\hat{f}$ is obtained by performing an inverse Fourier transform of Equation (3.11).

$$\hat{f}(x, z) = \frac{1}{(2\pi)^2} \int_{-\infty}^{\infty} \int_{-\infty}^{\infty} F(k_x, k_z) e^{(ik_x x + ik_z z)} \mathrm{d}k_x \mathrm{d}k_z \tag{3.12}$$

The procedure of the FD-ORTHO-SAFT algorithm is summarized as follows:

1. Obtain an ultrasonic array signal $e(t, x_T, x_R)$
2. Perform a 3D fast Fourier transform $e(t, x_T, x_R) \rightarrow E(\omega, k_T, k_R)$
3. Transform a coordinate from the signal to the image domain slice by slice $E(\omega, k_T, k_R) \rightarrow F(k_x, k_z|k_T)$
4. Add the slices together $F(k_x, k_z|k_T) \rightarrow \hat{F}(k_x, k_z)$
5. Conduct a 2D inverse fast Fourier transform to obtain a B-scan image $\hat{F}(k_x, k_z) \rightarrow \hat{f}(x, z)$

4. VALIDATION OF SAFT ALGORITHM BY SIMULATION

To validate the FD-ORTHO-SAFT algorithm, an ultrasonic array data is simulated using two different simulation methods - the mathematical model and the finite-difference time-domain (FDTD) method. The mathematical model using the steady-state wave equation solution creates an ultrasonic array data without derivative wave phenomena like multiple reflections, surface waves, mode conversion, and others, which helps to evaluate the pure performance of the SAFT algorithm. In contrast to the mathematical model, the FDTD method calculates all wave field conditions every iteration step based on the wave equation. Figure 4.1 shows a snapshot of the FDTD method. With the simulated array signal by the FDTD method including wave phenomena, the feasibility of the SAFT algorithm on implementation in the field can be tested. In this simulation, it is assumed that the material property is known.

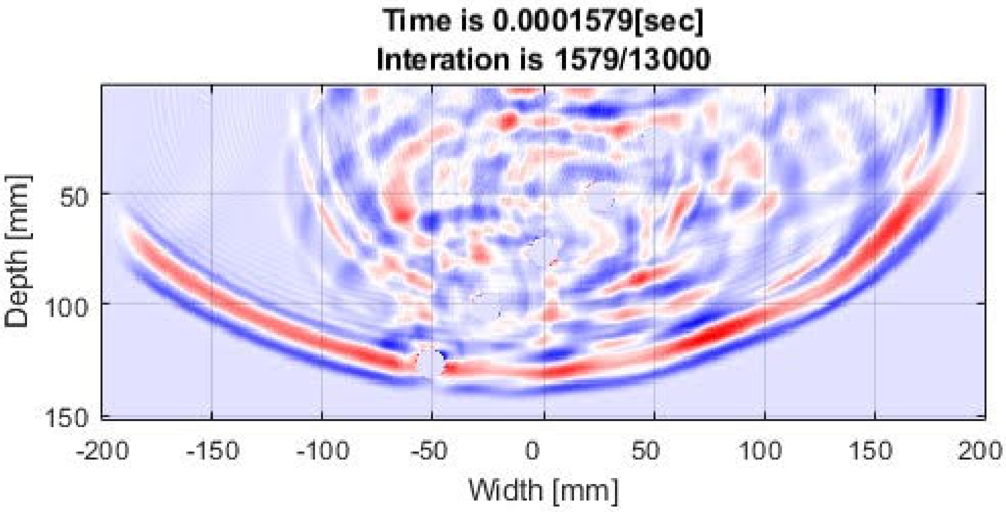

Figure 4.1: Snapshot of FDTD Method for Simulation

4.1 SIMULATION BY MATHEMATICAL MODEL

The wave propagation in the 2D free space can be represented as a Green's function of the 2D wave equation. For the simulation of an ultrasonic array signal, the impulse wave is emitted from a transmitter, reflected at damage, then recorded at a receiver. Thus, an array signal can be written as

$$E_n(\omega, x_T, x_R) = P(\omega)G(\omega, r_{T,n})G(\omega, r_{R,n}) \tag{4.1}$$

where E_n is the array signal for the n^{th} damage in the frequency-domain, ω is the angular frequency, x_T and x_R are the transmitter and the receiver, respectively, P is the amplitude spectrum of the impluse signal, G is the 2D free-space Green's function, r_n is the distance from the transducer to the n^{th} damage. The geometry for the mathematical model is plotted in Figure 4.2.

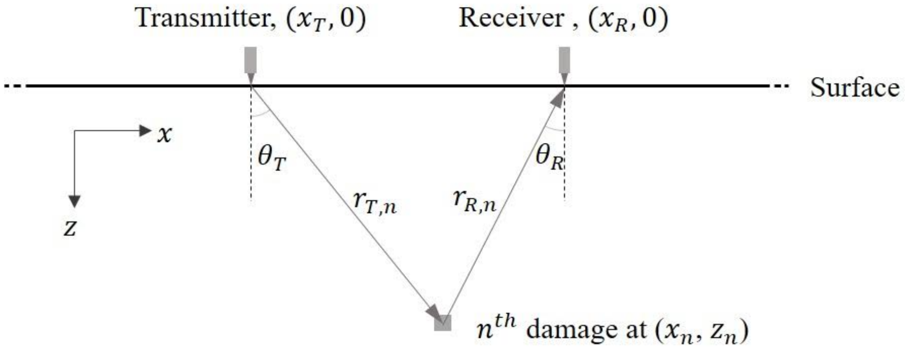

Figure 4.2: Schematic Geometry for Mathematical Model

The Green 's function of the 2D wave equation is represented by Hankel function,

$$G(\omega, r) = \frac{-\,i}{4} H_0^{(2)}(kr) \tag{4.2}$$

where $H_0^{(2)}$ is the Hankel function of the second kind, and k is the wavenumber.

If the wavefield satisfies the far-field approximation, the Green's function can be expressed in another form

$$G(\omega, r) \approx \frac{-\,1}{\sqrt{i8\pi kr}} \exp(-ikr) \tag{4.3}$$

In Equation (4.3), the wavenumber k will be constant if the medium is isotropic. This wavenumber k for the orthotropic media is a can be changed and can be written as a function of the wave propagation direction, $k(\theta) = \omega/c(\theta)$. The procedure of calculating the group velocity curve using the stiffness matrix is explained in Section 2.2.3.

For a multiple-damage case, the total array signal can be calculated by the summation of the array signal of individual damage

$$E(\omega, x_T, x_R) = \sum_{n=1}^{N} E_n(\omega, x_T, x_R) \tag{4.4}$$

where N is the number of damage.

Finally, the simulated ultrasonic array signal e is calculated via the inverse Fourier transform of the total array signal in the angular frequency-domain

$$e(t, x_T, x_R) = \frac{1}{2\pi} \int_{-\infty}^{\infty} E(\omega, x_T, x_R) \exp(i\omega t) \mathrm{d}\omega \tag{4.5}$$

4.2 SIMULATION BY FINITE-DIFFERENCE TIME-DOMAIN METHOD

The FDTD method estimates the wave field from the governing equations of the wave motion. The ultrasonic wave motion is governed by Newton's law of motion and by stress-strain relations.

Newton's law of motion in 2D is given by

$$\rho(\mathbf{x})\frac{\partial v_i(\mathbf{x},t)}{\partial t} = \frac{\partial \tau_{ij}(\mathbf{x},t)}{\partial x_j} + F_i(\mathbf{x},t) \qquad i,j = 1,3 \tag{4.6}$$

where ρ is the density, v_i is the particle velocity, $\mathbf{x}$ is the position, t is the time, τ_{ij} is the internal force, and F_i is the external force.

The stress-strain relationship can be written as

$$\tau_{ij}(\mathbf{x},t) = c_{ijkl}(\mathbf{x})e_{kl}(\mathbf{x},t) + I_{ij}(\mathbf{x},t) \qquad i,j,k,l = 1,3 \tag{4.7}$$

where c_{ijkl} is the stiffness tensor, e_{kl} is the strain, and I_{ij} is the external stresses.

The stiffness tensor for the orthotropic media can be reduced to the stiffness matrix in Equation (2.14), and the strain has the relationship with the velocity as follows:

$$\frac{\partial e_{ij}(\mathbf{x},t)}{\partial t} = \frac{1}{2}\left(\frac{\partial v_i(\mathbf{x},t)}{\partial x_j} + \frac{\partial v_j(\mathbf{x},t)}{\partial x_i}\right) \qquad i,j = 1,3 \tag{4.8}$$

In order to calculate the wave field status at every iteration step, solving the first-order differential equations of Equation (4.6) and (4.7) is required. Solving the first-order differential equation is not a recommended way for numerical method, Thus, the staggered-grid technique introduced by Yang (2008) is used. This technique calculates the wave field at every step without solving the first-order differential equations.

Initial conditions for all parameters are assumed as zero, and the boundary conditions for the sides and top/bottom are absorbing and fixed boundary conditions, respectively.

4.3 SIMULATION PARAMETERS AND SIMULATED SIGNALS

The material is simulated similar to typical glued laminated timber, which has a strong stiffness along the longitudinal axis and a relatively weak stiffness perpendicular to the longitudinal axis. Therefore, the group velocity curve for the simulated material has a form of a vertically compressed semi-circle as shown in Figure 4.3. The simulation parameters are summarized in Table 4.1. The stiffness values of the material are calculated based on the measured group velocities and density. To compare the performance of the algorithm at different depths, five damages at different depths are simulated. For the mathematical model, point damage is assumed. On the other hand, 12.7 mm diameter cavity is assumed as damage.

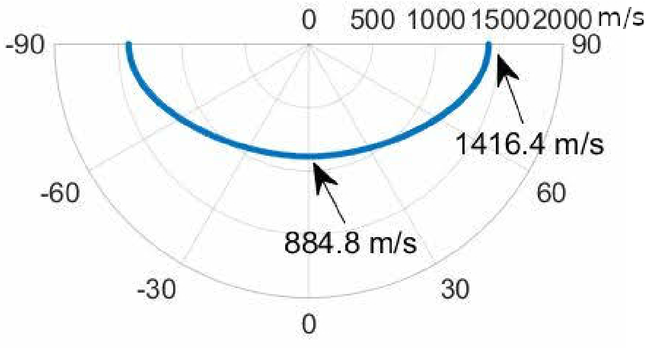

Figure 4.3: Group Velocity Curve for Simulated Material

Table 4.1: Ultrasonic Array Simulation Parameters

Parameters	Values
# of transducers	12
Transducer spacing	30 mm
Transmitting wave frequency	50 kHz
Data sampling frequency	1 MHz
Stiffness matrix for material	$\begin{array}{cc} & \begin{array}{ccc} xx & zz & xz \end{array} \\ \begin{array}{c} xx \\ zz \\ xz \end{array} & \left[\begin{array}{ccc} 1.5227 & 0.15 & 0 \\ 0.15 & 0.5942 & 0 \\ 0 & 0 & 0.35 \end{array}\right] \end{array}$ GPa
Material density	759 kg/m^3

Since the developed SAFT algorithm will be applied to the commercial ultrasonic tomography device A1040 MIRA, the MIRA parameters are used. The device has 12 arrays of transducers with a spacing of 30 mm, emits an impulse with a frequency of 50 kHz, and records data at 1 MHz.

Figure 4.4 shows the simulated array signals by the mathematical model and the FDTD method. The simulated array signal by the mathematical model contains only pure reflection from five damages. On the contrary, the simulated array signal by the FDTD method embraces various wave phenomena like surface waves, back wall reflection, multiple reflections from diverse reflectors, and so on.

4.4 SAFT RESULTS OF SIMULATED SIGNAL

The simulated signals are processed using four different SAFT algorithms: time-domain SAFT algorithm for isotropic media (TD-ISO-SAFT), frequency-domain SAFT algorithm for isotropic media (FD-ISO-SAFT), time-domain SAFT algorithm for orthotropic media (TD-ORTHO-SAFT), and frequency-domain SAFT algorithm for orthotropic media (FD-ORTHO-SAFT). In the SAFT algorithm for orthotropic

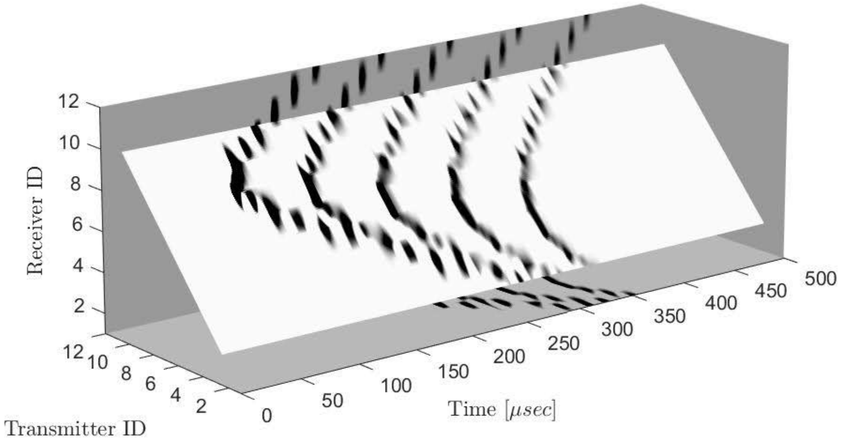

(a) Simulated signal by the mathematical model

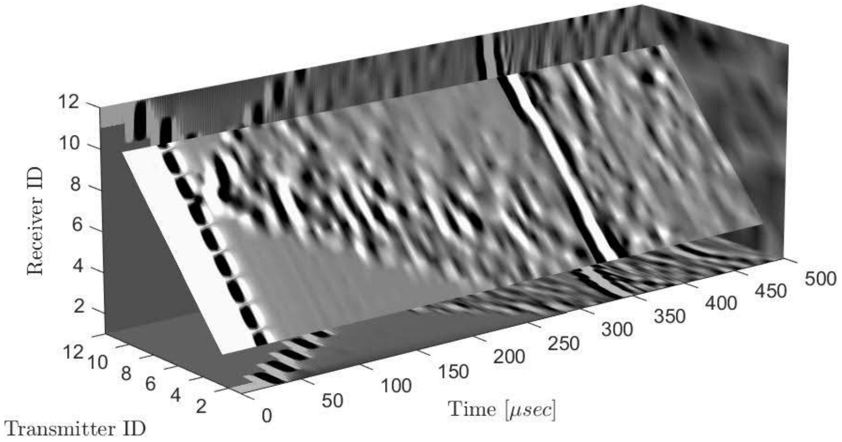

(b) Simulated signal by the FDTD method

Figure 4.4: Simulated Ultrasonic Array Signals

media (ORTHO-SAFT), the group velocity curve is calculated from the known material property. The vertical direction group wave velocity of 884.8 m/s is used as a wave velocity in the SAFT algorithm for isotropic media (ISO-SAFT).

The resulting B-scan images are plotted in Figures 4.5 to 4.8 using the mathematical model and the FDTD method. The location of the damage is marked as “x”, and the transducer array is indicated by inverse triangles.

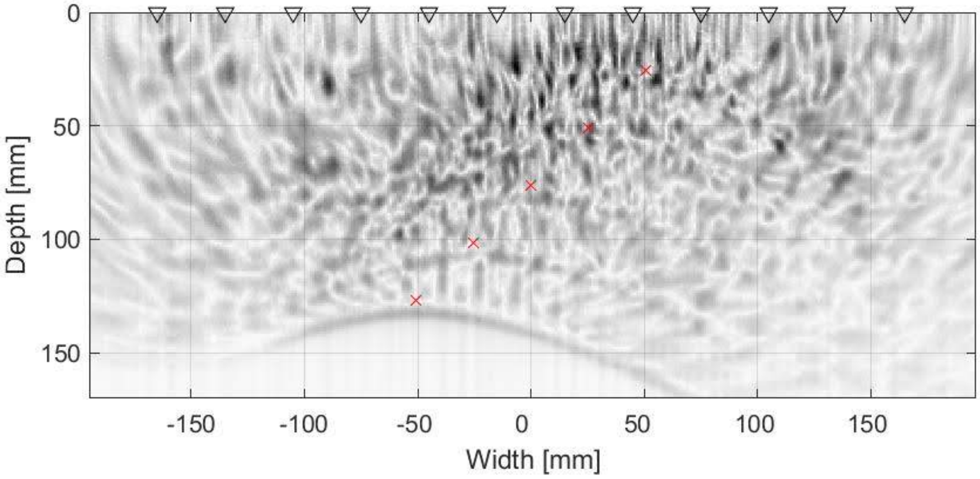

(a) B-scan by TD-ISO-SAFT

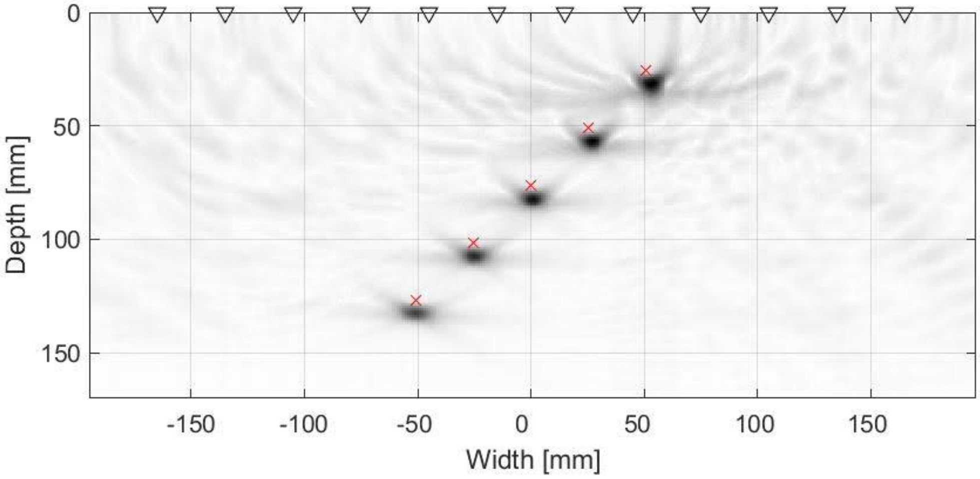

(b) B-scan by TD-ORTHO-SAFT

Figure 4.5: B-scan Results of Mathematical Model by TD-SAFT

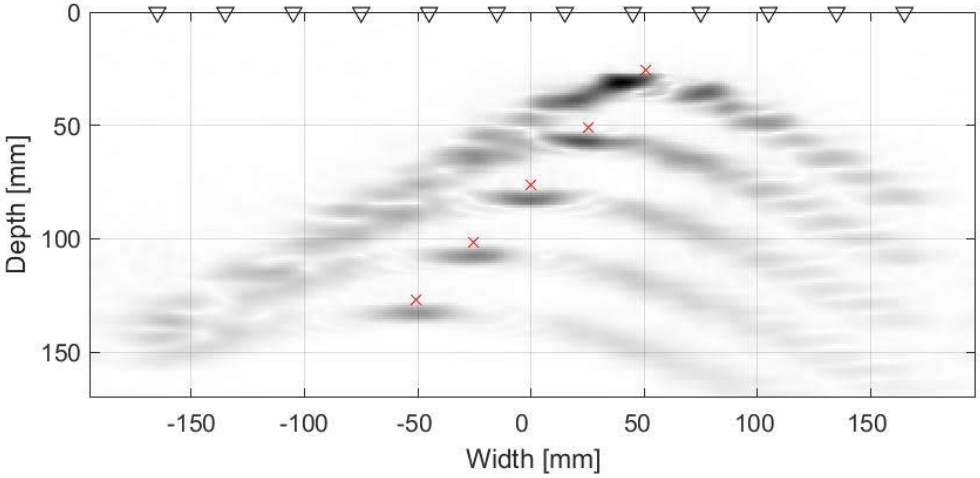

(a) B-scan by FD-ISO-SAFT

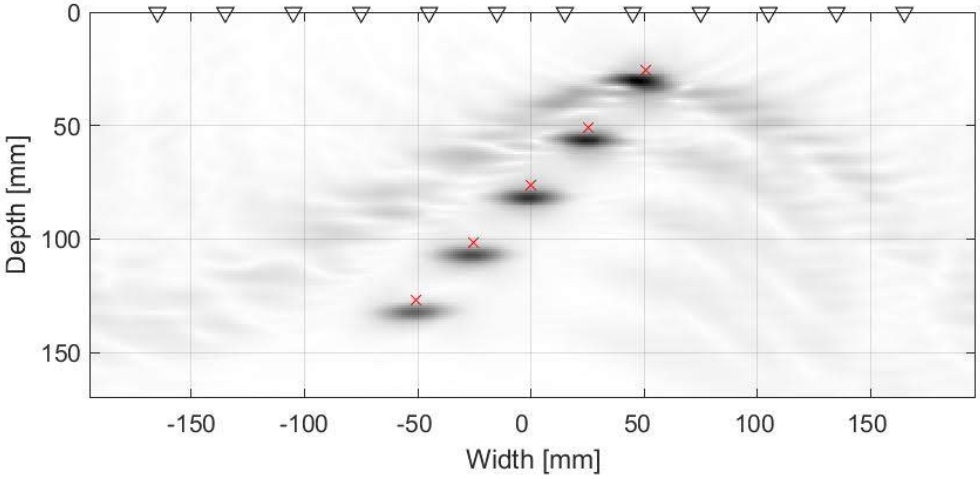

(b) B-scan by FD-ORTHO-SAFT

Figure 4.6: B-scan Results of Mathematical Model by FD-SAFT

With Figure 4.5 and 4.6 for the mathematical model, the pure performance of the algorithm can be analyzed. Results show that the ORTHO-SAFT can predict the exact damage location while the ISO-SAFT indicates the damage location only approximately. Because the vertical group velocity value is used for the algorithm, the algorithm only detects the depth of the damage, not the shape of the damage.

And, since the ISO-SAFT algorithm considers the wave velocity is constant, the expected damage shape is stretched horizontally because of the higher horizontal group velocity than the vertical group velocity.

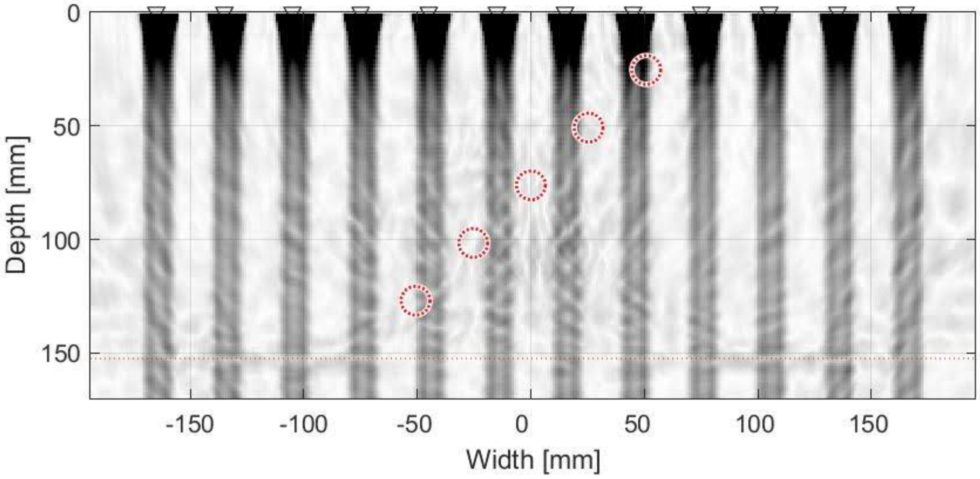

(a) B-scan by TD-ISO-SAFT

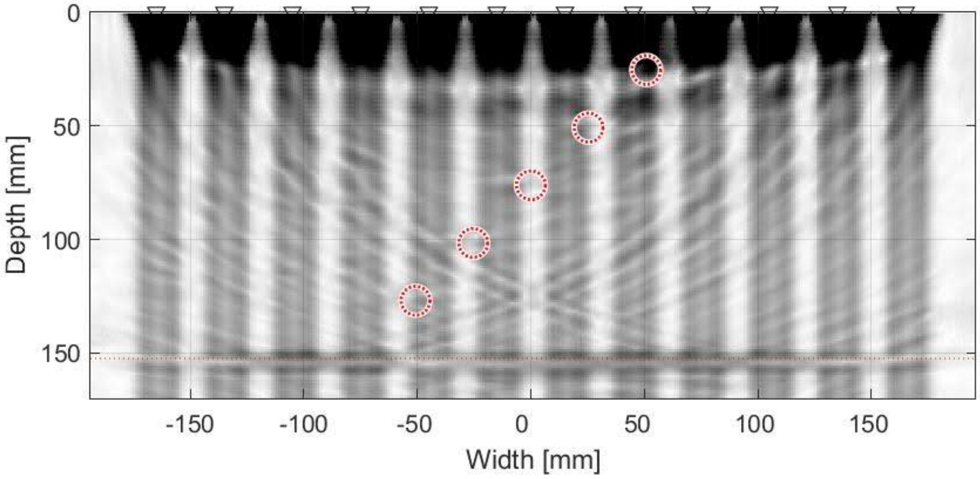

(b) B-scan by TD-ORTHO-SAFT

Figure 4.7: B-scan Results of FDTD Method by TD-SAFT

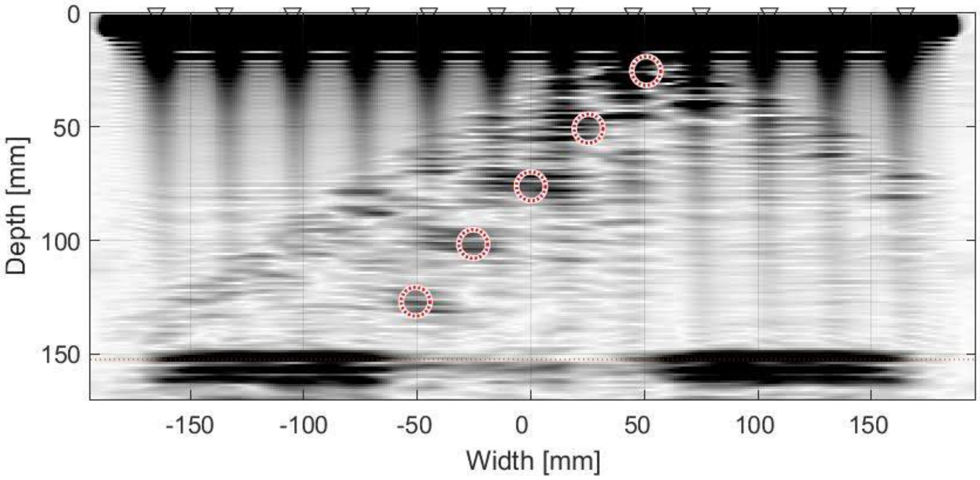

(a) B-scan by FD-ISO-SAFT

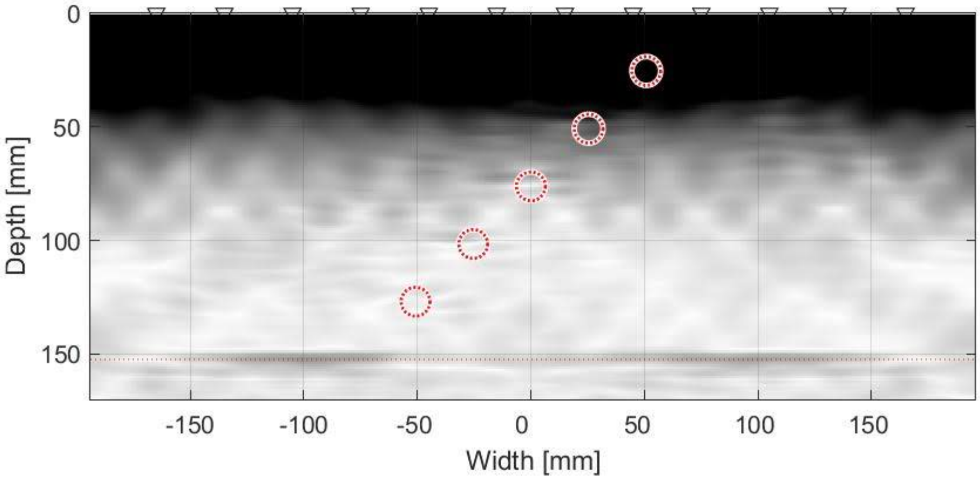

(b) B-scan by FD-ORTHO-SAFT

Figure 4.8: B-scan Results of FDTD Method by FD-SAFT

Since the simulated array signal by the FDTD method contains pure reflections from damages as well as other wave phenomena, the B-scan results of the FDTD signal have a lot of noise all over the region. Strong reflections are placed near the array for both the TD-SAFT and the FD-SAFT algorithms because of the surface noise. The relatively weak reflections are placed at the damage locations. In contrast, the B-scan results of the signal by the mathematical model show more clear images than the FDTD method.

The TD-SAFT algorithm shows an eroded result if the velocity in the algorithm is not matched with the material velocity. However, the TD-SAFT algorithm shows a clearer result once the material properties are known. The FD-SAFT algorithm shows a reasonable result even if the limited velocity information is used. Once the intact group velocity information is used, the noise decreases, and the resolution of the B-scan image increases.

It is observed from all B-scan images that the expected damage location is slightly downshifted. This is because that the SAFT algorithm computes a reflection value based on the amplitude of a signal, and the maximum amplitude of a sinusoidal impulse starts at a quarter of the wavelength after triggering. For this simulation, a quarter wavelength of the input signal in the vertical direction equals to 4.42 mm. Thus, all expected reflections are shifted down by 4.42 mm from the exact locations.

5. PARAMETRIC STUDY

In this chapter, multiple parameters affecting the performances of the SAFT algorithm are investigated. First, quantifying the performance of the algorithm is explained with respect to the resolution of images. Then, the effects of the operational frequency, the number of transducers, and the shape of the group velocity curve on the algorithm performance are evaluated. Second, the shapes of expected damages are analyzed with the potential damage curve. Finally, the computation times of the FD-ORTHO-SAFT and TD-ORTHO-SAFT are compared to check the feasibility for in-situ inspection.

5.1 PERFORMANCE OF SAFT ALGORITHM

In the mathematical model for simulating ultrasonic array signals, the damage is assumed as a point. Thus, the performance of a SAFT algorithm is good if the area of an expected damage shape calculated by the SAFT algorithm is small. To quantify the performance of a SAFT algorithm using this concept, the array performance indicator (API) is explained in the study by Holmes et al. (2005). The equation of the API is defined as

$$API = \frac{A}{\lambda} \tag{5.1}$$

where A is the intersecting area between a resultant image surface and a flat surface down from the maximum reflection, e.g., -6dB, which is perpendicular to the z-axis as described in Figure 5.1, and λ is the wavelength of the impulse wave.

The API is a unitless value showing the performance of a SAFT algorithm regardless of an impulse operating frequency. However, a wavelength for orthotropic

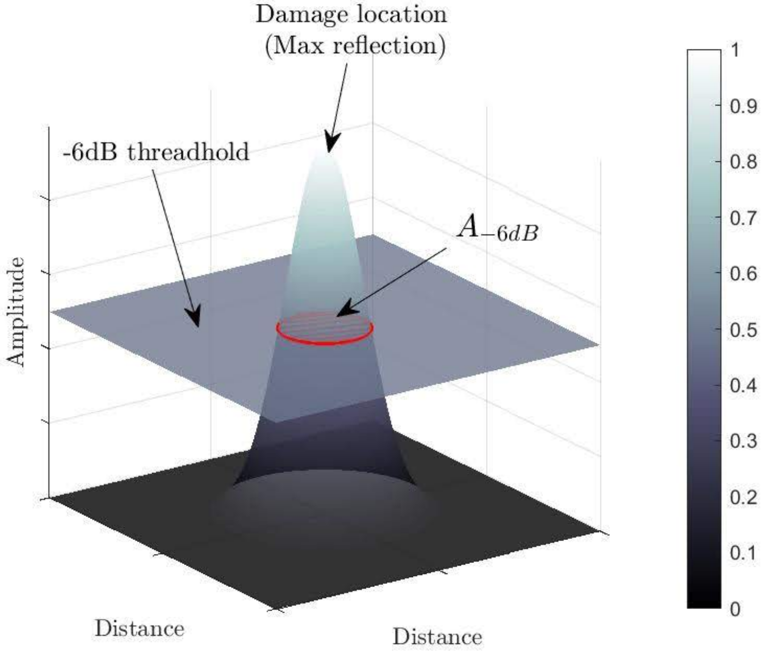

Figure 5.1: Concept of API

media is not a constant value. Hence, the modified API, API_m, is used for the ORTHO-SAFT algorithm to have a consistency, which described as

$$API_m = \frac{A}{\lambda_v} \tag{5.2}$$

where λ_V is the wavelength along the vertical direction.

In this study, -6dB is used as the threshold. The API values of the TD-ORTHO-SAFT and the FD-ORTHO-SAFT for five damage simulations by the mathematical model are summarized in Table 5.1. The FD-ORTHO-SAFT provides better performance than the TD-ORTHO-SAFT on average. Specifically, the FD-ORTHO-SAFT shows a high performance near the array and the center of the array, and the TD-ORTHO-SAFT shows a high performance near the array and the side of the array.

Table 5.1: API of TD-ORTHO-SAFT and FD-ORTHO-SAFT for Damage in Different Locations

Damage location (mm)	TD-ORTHO-SAFT API (unitless)	FD-ORTHO-SAFT API (unitless)
(50.8, 25.4)	0.2783	0.2304
(25.4, 50.8)	0.2987	0.2032
(0, 76.2)	0.3129	0.2326
(-25.4, 101.6)	0.3173	0.2444
(-50.8, 127)	0.2828	0.3388
Average	0.2980	0.2499

If a point damage is simulated at multiple locations and the API at each point is calculated, a contour map of API, called the performance map, can be created. The performance map shows the performance of an algorithm over the 2-D space.

5.1.1 Effect of Group Velocity Curve's Shape

Three different materials are considered in this subsection, and the corresponding group velocity curves are plotted in Figure 5.2. One isotropic and two orthotropic properties are used and a horizontal velocity of 1432 m/s is identical for all three media. The group velocities along the vertical direction for three materials are presented in Figure 5.2.

Performance map parameters are summrized in Table 5.2. These parameters are used in the following parametric studies unless otherwise noted.

Figures 5.3(a) and 5.3(b) show the performance maps of the TD-ORTHO-SAFT and the FD-ORTHO-SAFT for the three different media, respectively. The performances of both algorithms are considerably affected by the shape of the group velocity curve. When the group velocity curve is compressed vertically, the performance

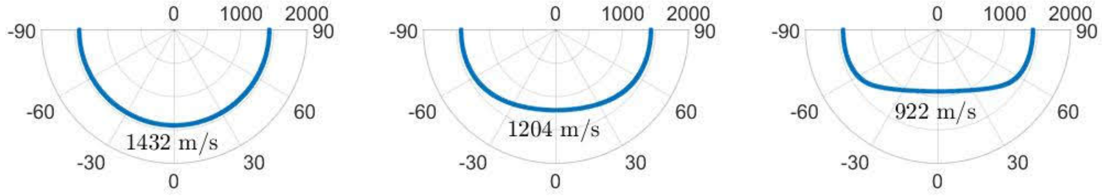

(a) Isotropic media (b) Orthotropic media #1 (c) Orthropic media #2

Figure 5.2: Three Different Group Velocity Curve Shapes for Parametric Study

Table 5.2: Parameters of Performance Map

Parameters	Values
Grid size	27 by 24
Grid spacing	30 mm
# of transducers	12
Impulse frequency	25 kHz
Sampling frequency	1 MHz

maps of both SAFT algorithms are compressed as well. The sharp performance reduction of both algorithms occurs around 203 mm deep at the center of the array for the 3rd media case. While the FD-ORTHO-SAFT shows a relatively strong performance near the center of the array when the group velocity curve is vertically compressed, the TD-ORTHO-SAFT shows a high performance at the edge of the array. The TD-ORTHO-SAFT shows a stable performance over the width, whereas the FD-ORTHO-SAFT shows a performance variation at the side of the array.

In the process of the FD-ORTHO-SAFT, the damage field $F(k_x, k_z)$ in the wavenumber domain is superimposed with respect to the transmitter transducer wavenumber k_{x_T}. This process yields a high spatial frequency near the center of the array and a low spatial frequency near the side of the array. This phenomenon results in the

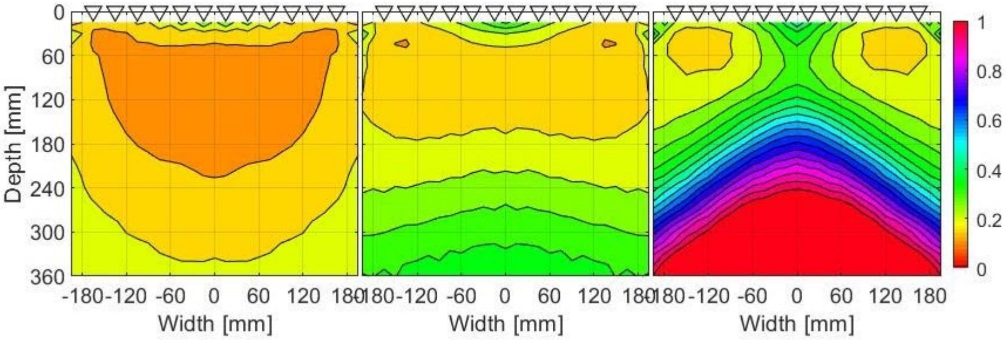

(a) Performance map by the TD-ORTHO-SAFT

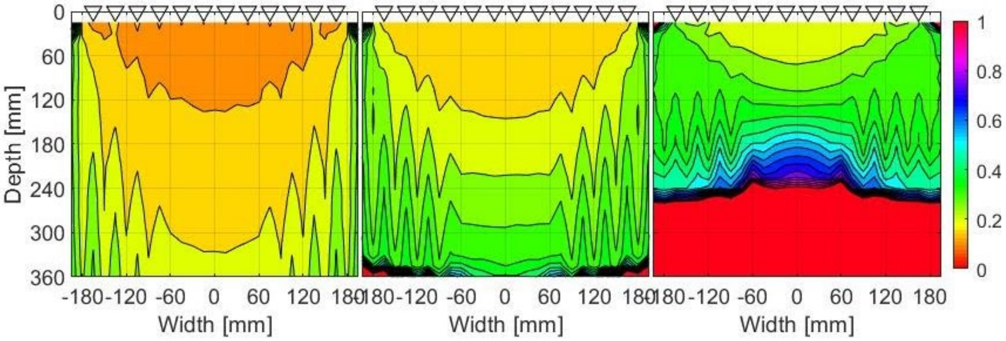

(b) Performance map by the FD-ORTHO-SAFT

Figure 5.3: Performance Map for Three Different Group Velocity Curves

spatial frequency aliasing and the irregular contour map near the side of the array. Thus, the performance at the edge of the array for the FD-ORTHO-SAFT can be improved if the spatial frequency of the array increases, or if the length of the array becomes longer and the transducer spacing is kept the same. The phenomenon of the relative reduction of performance in the TD-ORTHO-SAFT will be addressed in the next subsection.

5.1.2 Effect of Array's Spatial Frequency

The effect of the spatial frequency of the ultrasonic array on the performance is studied in this subsection. The spatial frequency of the ultrasonic array is equivalent to a reciprocal number of spacing between transducers. The spatial frequency increases from $(30\text{mm})^{-1}$ to $(5\text{mm})^{-1}$. The number of transducers increases from 12 to 67. The performance maps for three different media in Figure 5.2 using the TD-ORTHO-SAFT and the FD-ORTHO-SAFT are plotted in Figures 5.4(a) and Figure 5.4(b).

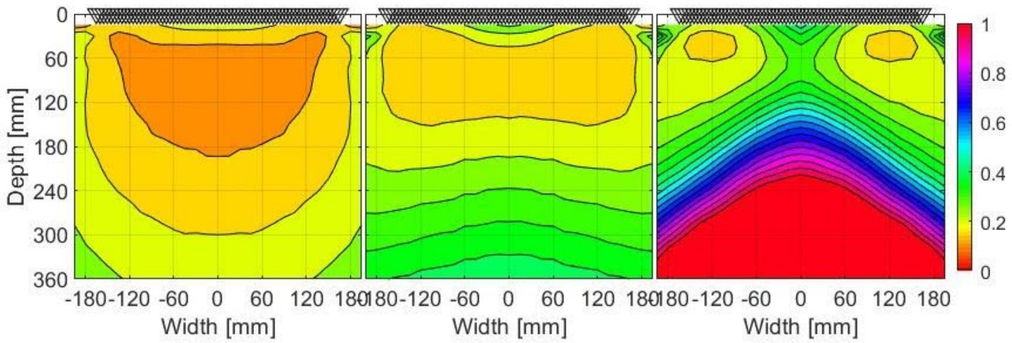

(a) Performance map by the TD-ORTHO-SAFT

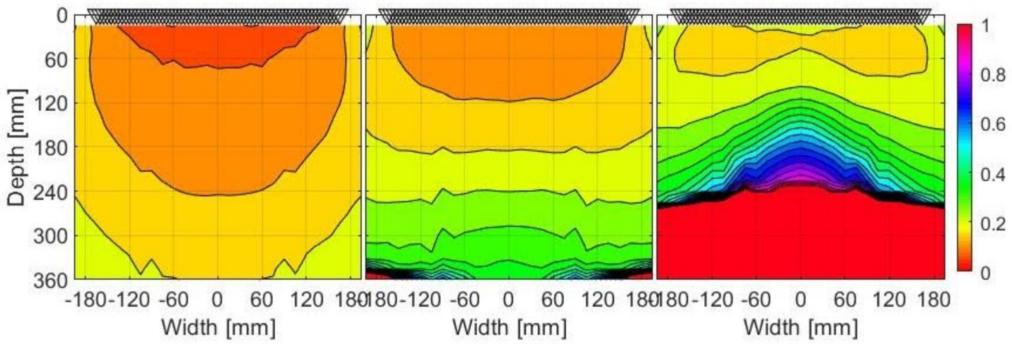

(b) Performance map by the FD-ORTHO-SAFT

Figure 5.4: Performance Map for Three Different Group Velocity Curves with Increased Spatial Frequency of $(5\text{mm})^{-1}$

For the TD-ORTHO-SAFT, there is no significant difference between low and high spatial frequency. On the contrary, the FD-ORTHO-SAFT shows a distinct improvement in the performance map. The resolutions at the entire area increase, and the performance near the side of the array becomes stable. Although the performance of the FD-ORTHO-SAFT increases with the increased spatial frequency, the performance increment at the center of the array is relatively slower than other regions if the group velocity curve is vertically compressed.

5.1.3 Effect of Wave Velocity

The performance maps with different wave velocities are calculated. The materials are isotropic and have different wave velocities. The group velocity curves are plotted in Figure 5.5.

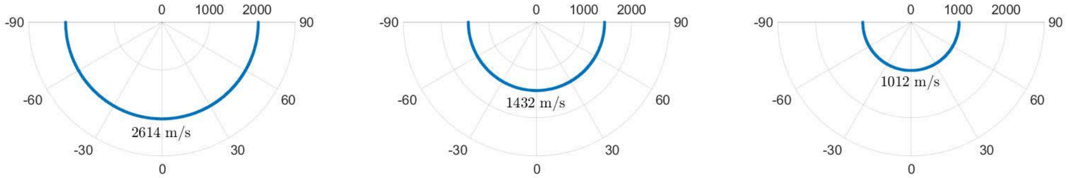

(a) $v = 2614 m/s$ (b) $v = 1432 m/s$ (c) $v = 1012 m/s$

Figure 5.5: Three Different Group Velocity Curves for Parametric Study of Wave Velocity

Figure 5.6 shows performance maps of different wave velocities. The TD-ORTHO-SAFT has a consistent performance with different wave velocities. However, the performance of the FD-ORTHO-SAFT is improved as the wave velocity increases. For the case of the wave velocity of 2614 m/s, the performance of the FD-ORTHO-SAFT is better than the TD-ORTHO-SAFT. Although the performance of both algorithms can be comparable, the actual performance of SAFT algorithm depends on the algorithm interpolation, impulse wave frequency, material properties, array system, wave velocity, and others.

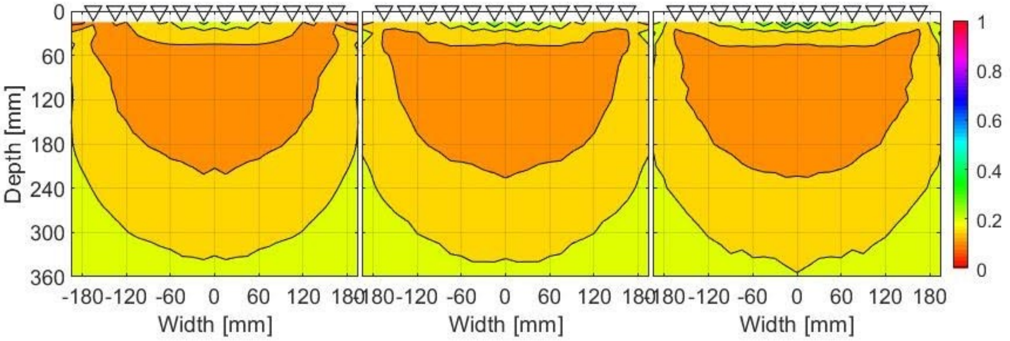

(a) Performance map by the TD-ORTHO-SAFT

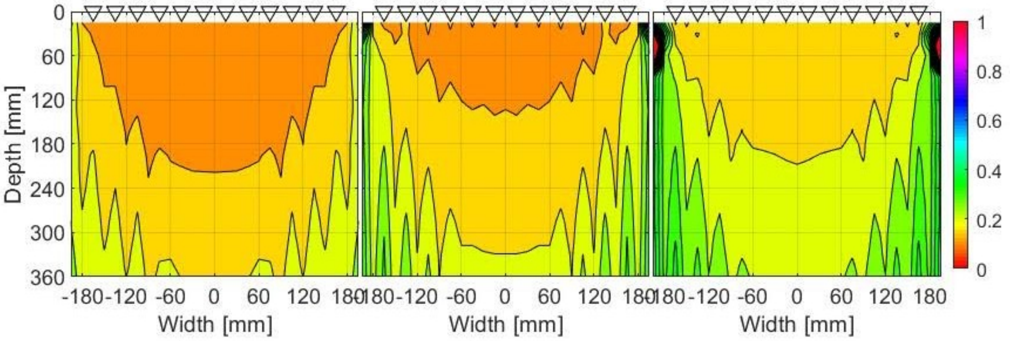

(b) Performance map by the FD-ORTHO-SAFT

Figure 5.6: Performance Map for Different Wave Velocities of 2614, 1432, and 1012 m/s

5.1.4 Effect of Impulse Operating Frequency

The performances of both the TD-OFTHO-SAFT and the FD-ORTHO-SAFT are compared in two different media types: isotropic and orthotropic. The group velocity curves for both media are plotted in Figure 5.7. The impulse operating frequencies of 45 and 85 kHz are used.

Figures 5.8 and 5.9 show the resulting B-scan images by both algorithms for

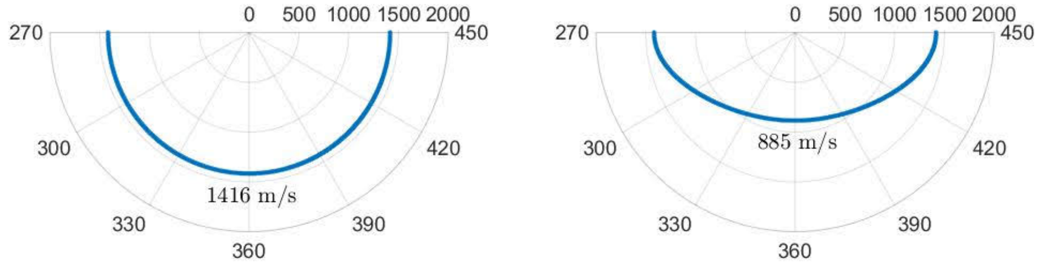

(a) Isotropic media

(b) Orthotropic media

Figure 5.7: Group Velocity Curve for Parametric Study of Impulse Operating Frequency Change

isotropic media with different impulse operating frequencies of 45 and 85 kHz. As the impulse operating frequency increases the resolutions of the resulting images for both algorithms increase as well. The TD-ORTHO-SAFT shows a higher lateral resolution than the FD-ORTHO-SAFT.

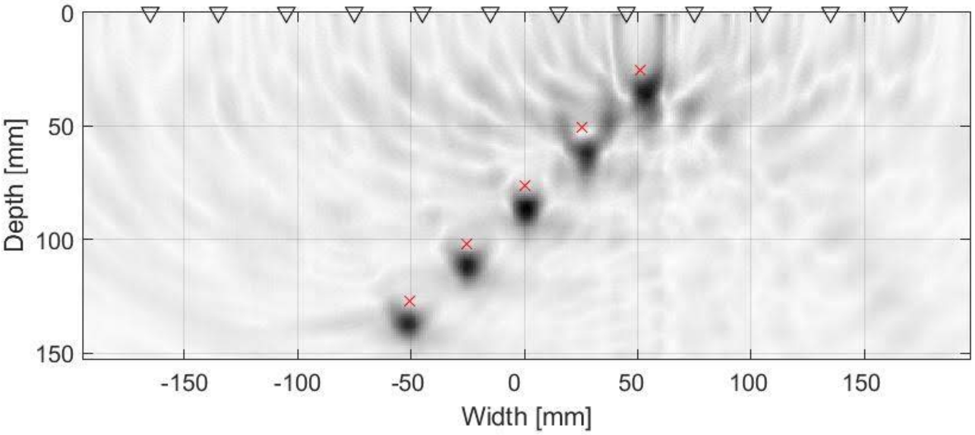

(a) B-scan by the TD-ORTHO-SAFT with the impulse operating frequency of 45 kHz

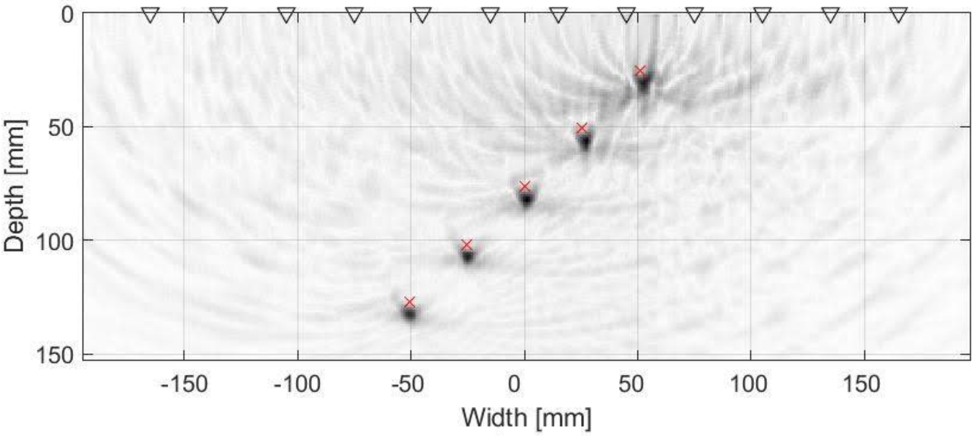

(b) B-scan by the TD-ORTHO-SAFT with the impulse operating frequency of 85 kHz

Figure 5.8: B-scan by TD-ORTHO-SAFT for Isotropic Media with Different Impulse Operating Frequencies of 45 and 85 kHz

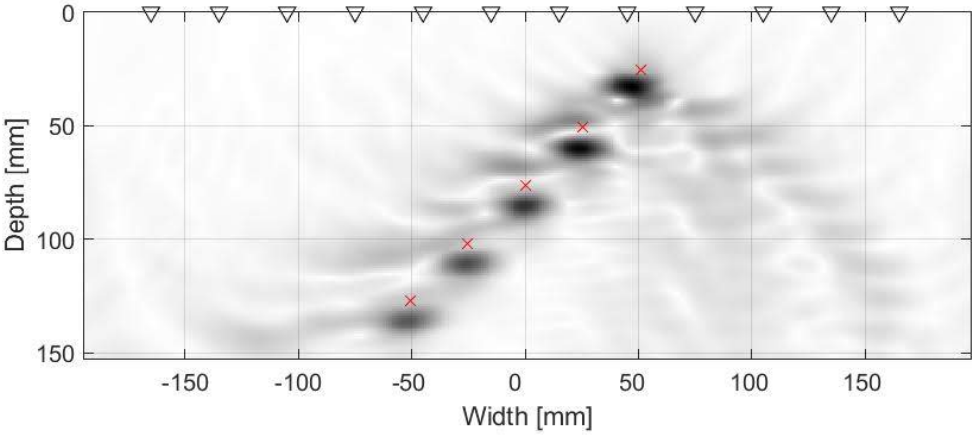

(a) B-scan by the FD-ORTHO-SAFT with the impulse operating frequency of 45 kHz

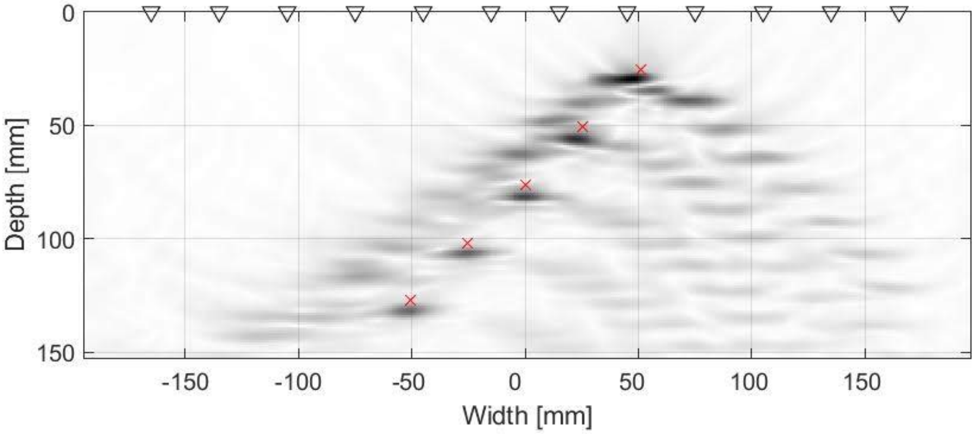

(b) B-scan by the FD-ORTHO-SAFT with the impulse operating frequency of 85 kHz

Figure 5.9: B-scan by FD-ORTHO-SAFT for Isotropic Media with Different Impulse Operating Frequencies of 45 and 85 kHz

Figures 5.10 and 5.11 show the resulting B-scan images by both algorithms for orthotropic media with different impulse operating frequencies of 45 and 85 kHz. The impulse operating frequency increment raises the resolution of the resultant B-scan images in orthotropic media as well. The shape of the focused reflection is compressed vertically as the group velocity curve is compressed vertically.

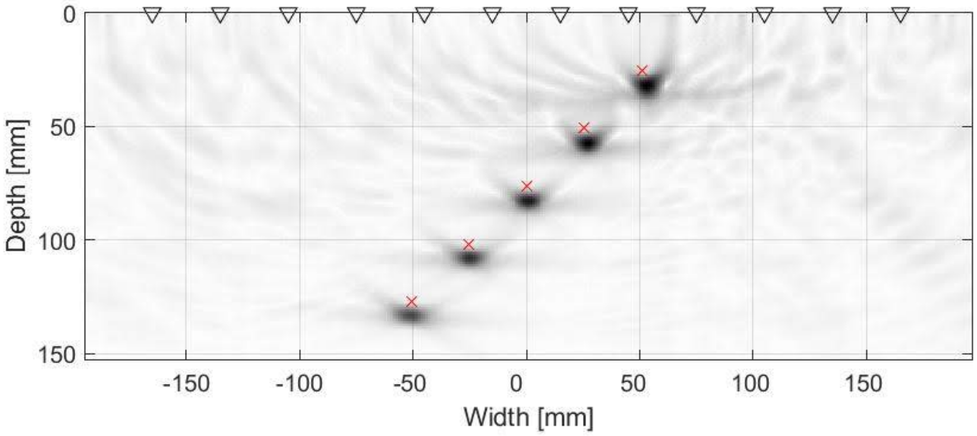

(a) B-scan by the TD-ORTHO-SAFT with the impulse operating frequency of 45 kHz

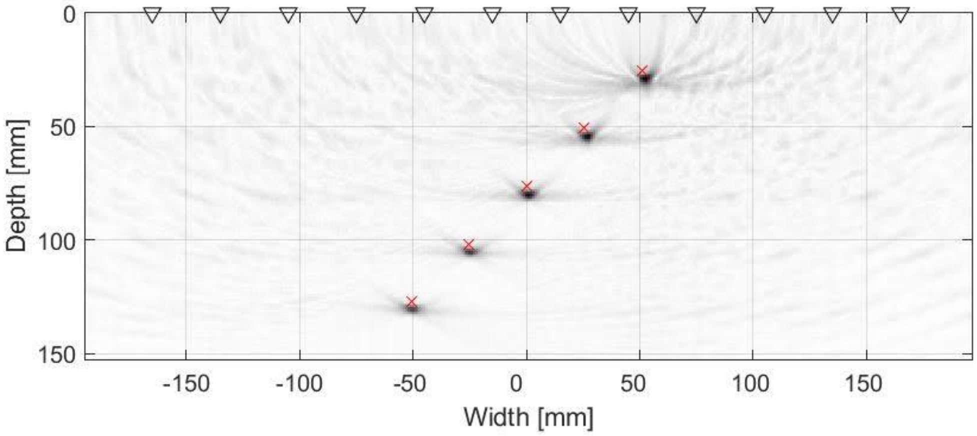

(b) B-scan by the TD-ORTHO-SAFT with the impulse operating frequency of 85 kHz

Figure 5.10: B-scan by TD-ORTHO-SAFT for Orthotropic Media with Different Impulse Operating Frequencies of 45 and 85 kHz

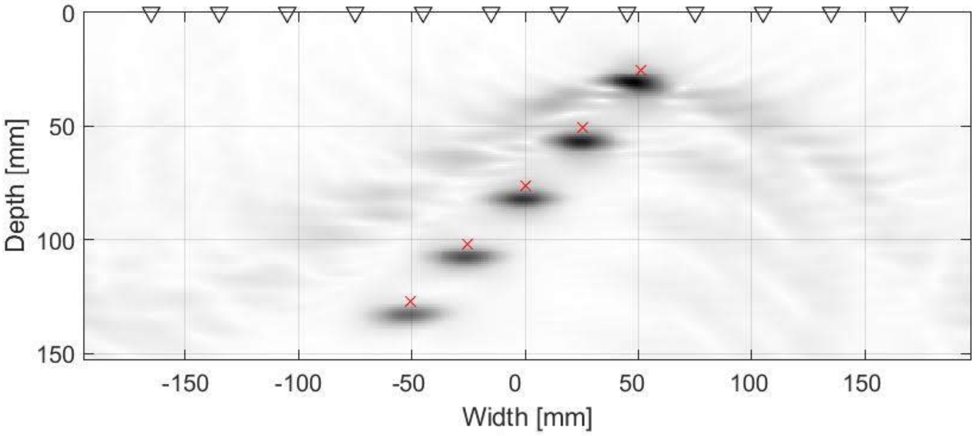

(a) B-scan by the FD-ORTHO-SAFT with the impulse operating frequency of 45 kHz

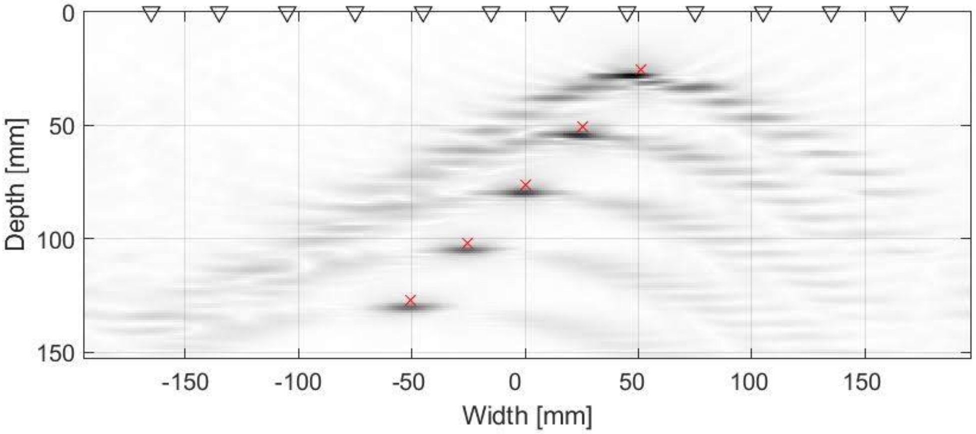

(b) B-scan by the FD-ORTHO-SAFT with the impulse operating frequency of 85 kHz

Figure 5.11: B-scan by FD-ORTHO-SAFT for Orthotropic Media with Different Impulse Operating Frequencies of 45 and 85 kHz

The API values for B-scan results by both algorithms with isotropic and orthotropic media are summarized in Table 5.3. Generally speaking, the performance of the algorithm decreases when the impulse operating frequency increases except for the case of the TD-ORTHO-SAFT in orthotropic media. This means that the resolution of the final B-scan images rises with the increment of the impulse operating frequency's growth, though the performance of the algorithm does not rise like the increment of the impulse operating frequency. To get the best performance of the algorithm, the impulse operating frequency of an impulse has to be carefully chosen based on the shape of a group velocity curve, the location of the expected damage, and other parameters.

Comparing the standard deviation values of APIs in Table 5.3, the performance of the FD-ORTHO-SAFT over different depths is more consistent than the TD-ORTHO-SAFT. Regarding the average values of APIs, the FD-ORTHO-SAFT shows better performance over different depths for isotropic media while the TD-ORTHO-SAFT shows better performance over different depths for orthotropic media.

Table 5.3: APIs for Parametric Study of Impulse Operating Frequency Change by TD-ORTHO-SAFT and FD-ORTHO-SAFT with Isotropic and Orthotropic Media

	APIs							
	TD-ORTHO-SAFT				FD-ORTHO-SAFT			
	Iso		Ortho		Iso		Ortho	
Damage Loc. (mm, mm)	45 (kHz)	85 (kHz)	45 (kHz)	85 (kHz)	45 (kHz)	85 (kHz)	45 (kHz)	85 (kHz)
(50.8, 25.4)	0.2096	0.2764	0.2389	0.2261	0.2304	0.3741	0.3505	0.6045
(25.4, 50.8)	0.2329	0.3804	0.1911	0.1973	0.2291	0.3817	0.3324	0.5030
(0, 76.2)	0.2894	0.5339	0.1914	0.1777	0.2465	0.4097	0.3443	0.5791
(-25.4, 101.6)	0.3174	0.4722	0.1988	0.1857	0.2576	0.4173	0.3715	0.5030
(-50.8, 127)	0.0598	0.0788	0.2150	0.2353	0.0723	0.1594	0.3809	0.5964
σ	0.1003	0.1793	0.0203	0.0252	0.0763	0.1072	0.0199	0.0503
μ	0.2218	0.3483	0.2070	0.2044	0.2072	0.3484	0.3559	0.5572

σ: standard deviation

μ: average

5.2 POTENTIAL DAMAGE CURVE

A potential damage curve is a collection of possible damage locations for a transducer pair if a group velocity and travel time are given. The concept of the curve is depicted in Figure 5.12. The red 'x' mark is the actual damage location, and the other black dots are possible damage locations with given information. If the curves for all transducer pairs are drawn, the shape of reflection field can be estimated. Since the curve is the location of a potential damage, the more the curve is overlapped, the higher the reflection is expected.

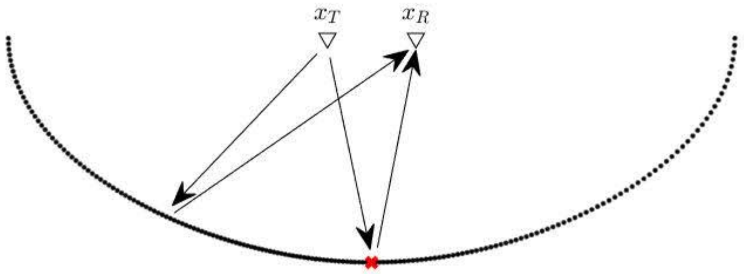

Figure 5.12: Concept of Potential Damage Curve

If the group velocity curve for a material is unknown, the reflection of an expected damage will not be focused well in a resulting image. The potential damage curve can provide an expected reflection shape if the group velocity curve for a material is not given. Figure 5.13(a) shows the case where the group velocity of the material is the same as for the SAFT algorithm. All lines intersect at the exact damage location. Figure 5.13(b) shows the case of different group velocity curves for the material and SAFT algorithm. The group velocity for the material is used to calculate the travel time. The algorithm uses a constant group velocity of 884.8 m/s. This is the same as the ISO-SAFT algorithm. In this figure, the curves do not intersect completely at the damage location, but pass near the damage location because the same vertical velocity is used. A parabolic pattern of intersection is observed.

An intersecting angle is the spreading-out angle from the damage location in potential damage curves for all transducers pairs. The intersecting angle is related to the shape of reflections, which is strongly related to the performance. The potential damage curve for damage which is located far away from the array and at the center of the array and which is located close to the array and at the side of the array in Figure 5.14. The intersecting angles and the API values of both algorithms for different damage locations with the vertically compressed group velcity curve are

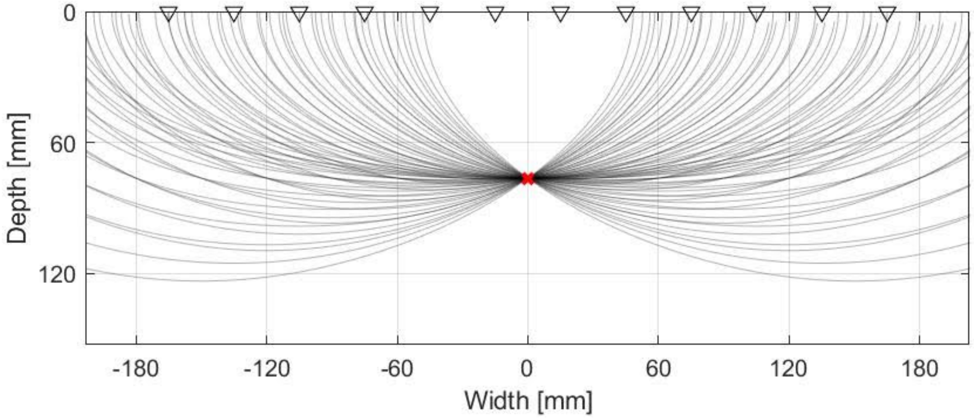

(a) Identical Group Velocity Curve for Material and SAFT Algorithm

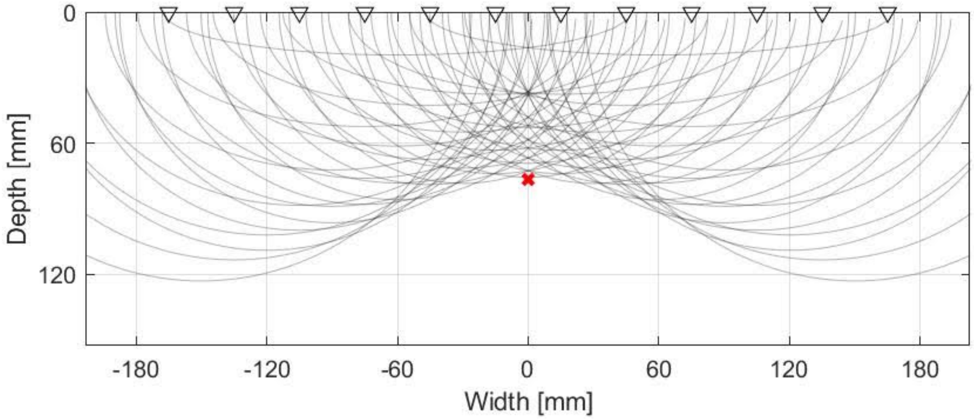

(b) Nonidentical Group Velocity Curve for Material and SAFT Algorithm

Figure 5.13: Potential Damage Curve for Single Damage with Identical and Nonidentical Group Velocity Curve for Material and SAFT Algorithm

summarized in Table 5.4.

The relatiopship between the intersecting angle and the performance of the SAFT algorithm can be seen in this table. An expected damage location that has a large intersecting angle shows a small API value. But, not every damage location that has a large intersecting angle has a good performance. In the case of the TD-ORTHO-SAFT in Table 5.4, a damage near the side of the array shows a better

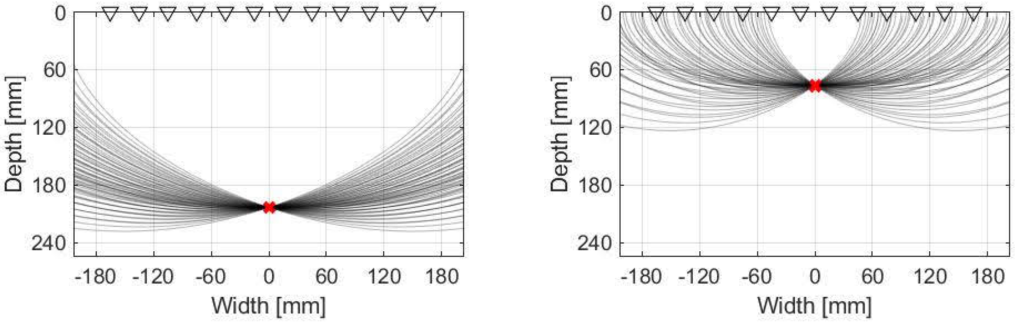

(a) Damage at (0, 76.2) mm (b) Damage at (0, 203.2) mm

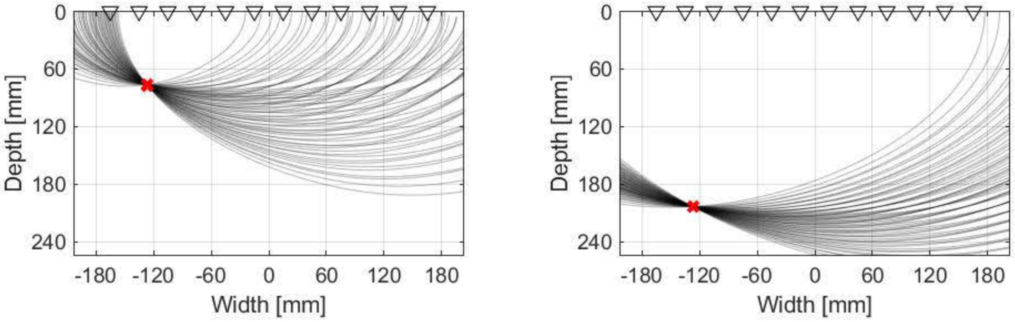

(c) Damage at (-127, 76.2) mm (b) Damage at (-127, 203.2) mm

Figure 5.14: Potential Damage Curve with Different Damage Locations

Table 5.4: Intersecting Angles, and API Values by TD-ORTHO-SAFT and FD-ORTHO-SAFT for Different Damage Locations

		API Values	
Damage Loc. (mm)	Intersecting Angle (deg)	TD-ORTHO-SAFT (unitless)	FD-ORTHO-SAFT (unitless)
(0, 76.2)	65.7	0.3129	0.2326
(0, 203.2)	34.8	0.8157	0.5363
(-127, 76.2)	59.6	0.1969	0.4859
(-127, 203.2)	32.9	0.4717	0.5081

performance than near the center of the array, but the FD-ORTHO-SAFT shows a better performance for a damage at the side of the array than near the center of the array. This could be because of the shape of the group velocity curve that is compressed vertically as well as the characteristic of the algorithm. For a vertically compressed group velcity curve, the FD-ORTHO-SAFT algorithm shows a better performance at the center of the array than the TD-ORTHO-SAFT.

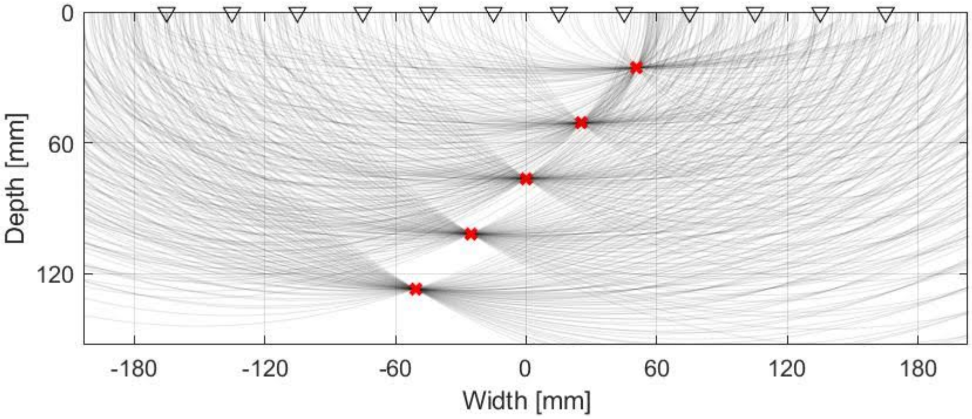

(a) Identical Group Velocity Curve for Material and SAFT Algorithm

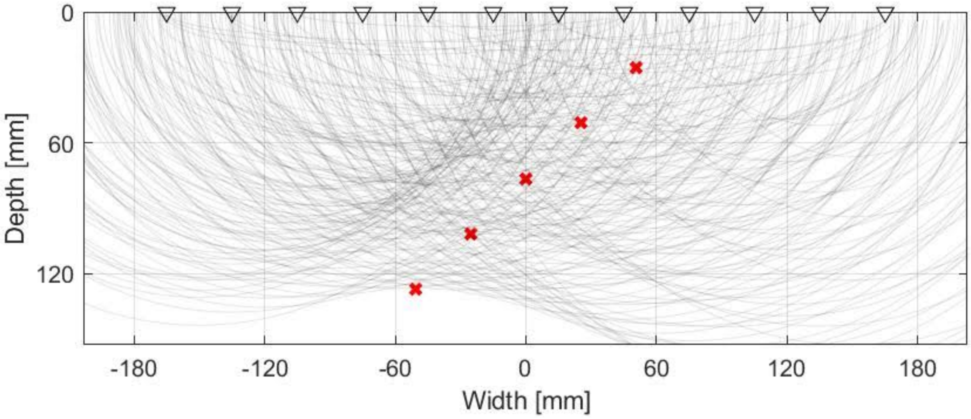

(b) Nonidentical Group Velocity Curve for Material and SAFT Algorithm

Figure 5.15: Potential Damage Curve for Five Damages with Different Depths with Identical and Nonidentical Group Velocity Curve for Material and SAFT Algorithm

Figures 5.15(a) and 5.15(b) depict the case of five damages for identical and non-identical group velocity curves, respectively. Comparing curves with the simulation results in Figures 4.5 and 4.6, the parabolic patterns are seen in the resulting image by the TD-ISO-SAFT algorithm. Also, the FD-ISO-SAFT shows a higher lateral resolution than the TD-ISO-SAFT algorithm in the same condition.

For wood products which are usually accessible to the surface parallel to the longitudinal axis, a vertically-compressed group velocity curve is typical for inspection. Hence, the FD-ORTHO-SAFT, which has a higher performance at the center of an array than the TD-ORTHO-SAFT, would provide a better result.

5.3 COMPUTATION TIME

The computation time of the algorithm can be estimated using the time complexity of the algorithm. Although the computation time is quite dependent on the computer system, the time complexity can tell the trend of the computation time for the algorithm. The time complexity of the TD-ISO-SAFT and the FD-ISO-SAFT are explained by Hunter et al. (2008) as follows:

$$c_{TD-SAFT} = \mathcal{O}(MNJ^2) \tag{5.3}$$

$$c_{FD-SAFT} = \mathcal{O}(MNJ + J^2Klog_2(J^2K) + MNlog_2(MN)) \tag{5.4}$$

where (M, N) is the resultant image's horizontal and vertical size, J is the number of transducers, and K is the length of signal data.

The TD-ISO-SAFT computes each pixel, $\mathcal{O}(MN)$, by superimposing data from all signal pairs, $\mathcal{O}(J^2)$. The FD-ISO-SAFT performs a 3-D FFT of the array data, $\mathcal{O}(J^2Klog_2(J^2K))$, transferring the domain, $\mathcal{O}(MN)$, slice by slice, $\mathcal{O}(J)$, and a 2-

D inverse FFT of the transferred data, $\mathcal{O}(MNlog_2(MN))$. For the ORTHO-SAFT algorithm, accessing the group velocity data corresponding to the wave orientation at each step is required. The interpolation method can be used to pick out the velocity at each iteration step. If the length of the group velocity data is assumed as V, the computation time to access the group velocity data vector until finding out the right data will increase by $\mathcal{O}(log_2(log_2(V)))$. This would cause the increment of computer resources' usage and computation time. Therefore, picking out the nearest data, $\mathcal{O}(1)$, from the group velocity data is recommended instead of interpolation in order to avoid a long computation time. If picking out the nearest data is used, the computation complexity for the FD-ORTHO-SAFT will be the same as Equations 5.3 and 5.4.

Figure 5.16 shows the computation complexity plot in terms of the number of pixels. Each term in the computation complexity for the FD-ORTHO-SAFT is designated. The MIRA parameters, $J = 12$ and $K = 2048$, are used in order to check the feasibility of the FD-ORTHO-SAFT algorithm in the MIRA environment. When the image size is small, the computation complexity of the TD-ORTHO-SAFT is smaller than the FD-ORTHO-SAFT, because the 3-D FFT calculation in the FD-ORTHO-SAFT requires a consistent computation time. In constrast to the small-sized image, the FD-ORTHO-SAFT shows a smaller computation complexity than the TD-ORTHO-SAFT as the size of the image increases. Among the computation complexity components in the FD-ORTHO-SAFT, the 2D inverse FFT calculation is the largest computation cost if the size of the image is large.

The measured computation times of the TD-ORTHO-SAFT and the FD-ORTHO-SAFT for various image sizes are summarized in Table 5.5. The TD-ORTHO-SAFT algorithm calculates faster than the FD-ORTHO-SAFT when the image is small, but the computation time of the TD-ORTHO-SAFT becomes slower than the FD-

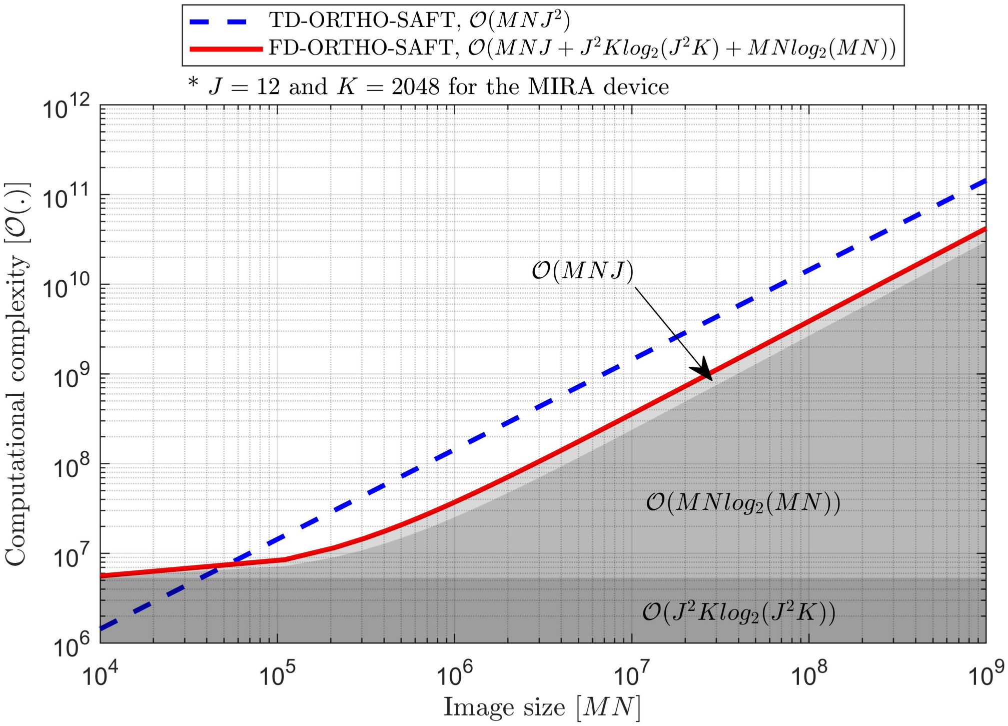

Figure 5.16: Computation Complexity for TD-ORTHO-SAFT and FD-ORTHO-SAFT

ORTHO-SAFT as the image becomes bigger. The size of the resultant B-scan image for the MIRA device is 296 pixels by 432 pixels, which is 127,872 square pixels. The TD-ORTHO-SAFT and the FD-ORTHO-SAFT will take over one second and below one second, respectively, to process the image if a similar processor is used.

Table 5.5: Computation Time of TD-ORTHO-SAFT and FD-ORTHO-SAFT

Image size $M \times N$ (pixel)	TD-ORTHO-SAFT (s)	FD-ORTHO-SAFT (s)
1,000	0.018	0.083
5,000	0.064	0.129
10,000	0.129	0.111
50,000	0.638	0.120
100,000	1.218	0.137
500,000	6.127	0.321
1,000,000	9.794	0.591
5,000,000	54.52	2.167
10,000,000	103.4	4.496

* Processor: Intel(R) Xeon(R) Gold 6148 CPU @ 2.40 GHz, 2.39 GHz

6. EXPERIMENTAL PROGRAMS

The feasibility of the developed FD-ORTHO-SAFT algorithm is tested with actual wood specimens. Once the wood specimens are scanned by the ultrasonic array device A1040 MIRA, ultrasonic array signals are extracted from the A1040 MIRA device. The B-scan images by the FD-ORTHO-SAFT are compared with the B-scan images by the TD-ORTHO-SAFT as well as the SAFT-C algorithm, which is the embedded time-domain SAFT algorithm in the A1040 MIRA device.

6.1 WOOD SPECIMENS

The wood specimens are made similar to a glued laminated timber beam. Hardwood Beech, which has a higher density than a typical softwood, is used to minimize the attenuation of a shear wave by air cavities. The type of lumber is plain-sawn lumber, which is typical, and the dimension of the lumber segment is 19.05 by 152.4 mm (0.75 by 6 inches). The general wood specimen for this experiment is plotted in Figure 6.1.

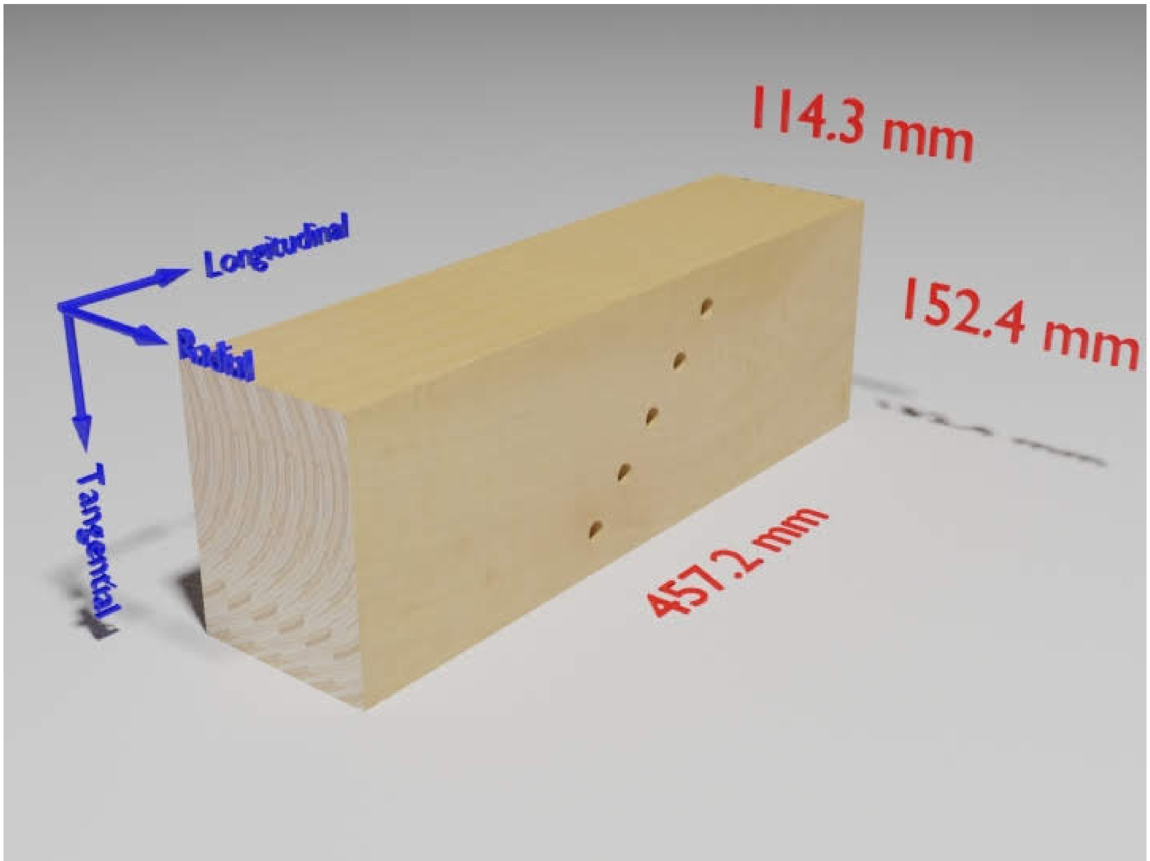

Figure 6.1: Wood Specimen with Coordinates and Dimensions

In order to glue the lumber segments together, a Titebond melamine glue as shown in Figure 6.2(a) is used. This glue has a lower strength than a typical wood glue to protect lumber from splitting after drying. After applying the glue, pressure is placed on the wood specimen by using parallel clamps as shown in Fiure 6.2(b).

An ultrasonic array is placed along the longitudinal axis and an ultrasonic wave will propagate in the longitudinal-tangential axis. Damage in the wood specimen is mimicked by circular holes through all layers. The dimension and the deployment of damage vary based on the damage scenario shown in Table 6.1.

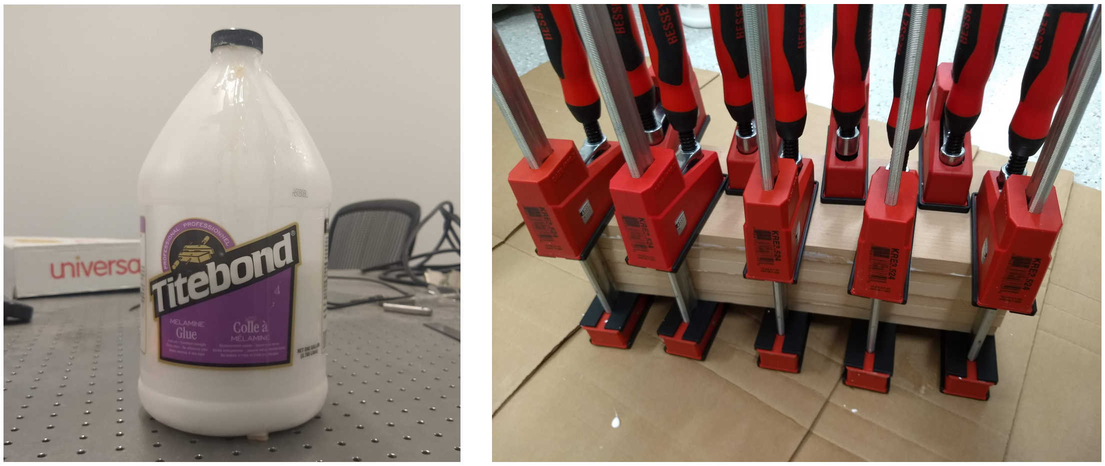

(a) (b)

Figure 6.2: Construction of Wood Specimen: (a) Melamine Wood Glue for Wood Specimen and (b) Clamping Wood Specimen

Table 6.1: Damage Scenarios for Experiment

Damage Scenario (Num.)	Damage Count (Num.)	Damage Diameter, ⌀ (mm)	Operating Frequency (kHz)	Damage Location[1)]
1	1	12.7	45	C
2	5	12.7	25,45,65, and 85	A, B, C, D, and E
3	5	25.4	25,45,65, and 85	A, B, C, D, and E
4	3	25.4	25,45,65, and 85	C, F, and G

[1)] A, B, C, D, E, F, and G: (-50.8, 127), (-25.4, 101.6), (0, 76.2), (25.4, 50.8), (50.8, 25.4), (-50.8, 101.6), and (50.8, 50.8) mm

6.2 ULTRASONIC ARRAY DEVICE

The ultrasonic array device used for the experiment is the A1040 MIRA as shown in Figure 6.3. The device using shear waves consists of four by twelve transducers. Four transducers behave like one transducer by averaging values to increase the accuracy of the device. Thus, this device acts like twelve transducers. This transducer is a dry contact probe that does not require a couplant which reduces a signal attenuation between surfaces. And it is supported by a spring to be applied to a rough surface.

Figure 6.3: Ultrasonic Tomography Device A1040 MIRA

Once the device is triggered, the first set of transducers emits an impulse and the remaining sets of transducers start recording. After that, the second set of transducers emits an impulse and the remaining set of the third to the last transducers start recording. And this procedure continues until the last set of transducers records an impulse fired from the eleventh set of transducers. Then, 66 pairs of signals are generated. Collecting data takes less than one second.

The A1040 MIRA's image reconstruction algorithm is called SAFT-C (Synthetic Aperture Focusing Technique with Sombinational sounding). This embedded SAFT algorithm is one of the time-domain SAFT algorithms and was developed for isotropic media like concrete. After processing of collected data, the A1040 MIRA displays a B-scan image on its screen. It usually takes 2∼3 seconds to display a result after triggering.

The A1040 MIRA provides two options for wave velocity for the embedded SAFT algorithm. An operator can input a number manually for wave velocity or use a wave velocity calculated by the device. Wave velocity is calculated with the known travel distance of transducer spacing and the measured travel time from a recorded signal.

6.3 MEASUREMENT OF GROUP VELOCITY

It is essential to know the group velocity curve of the wood specimen for reflections to be focused at the exact locations in the resultant B-scan images for the ORTHO-SAFT. The group velocity curve for the wood specimen is assumed to be an ellipse. Then, the velocities along the longitudinal and tangential axis are calculated with the measured travel time along both axes.

The low-frequency ultrasonic flaw detector A1220 Monolith and the drypoint contact shear wave transducer S1802, shown in Figure 6.4, are used to record travel signal. The travel times are manually selected from the recorded signals. Travel signals are recorded ten times per each axis. The measured velocities and the average velocities are summarized in Table 6.2.

Figure 6.4: Low-Frequency Ultrasonic Flaw Detector A1220 Monolith (Electronic Equipment) and Drypoint Contact Shear Wave Transducer S1802 (Probe)

Table 6.2: Measurement of Group Velocity

	Tangential	Longitudinal
Measured velocity [m/s]	881	1422
	889	1440
	873	1329
	977	1361
	866	1323
	826	1445
	863	1458
	915	1463
	932	1405
	844	1547
Average velocity [m/s]	885	1416

6.4 EXPERIMENTAL RESULTS

A collection of raw ultrasonic array signal data can be extracted from the A1040 MIRA device. The extracted raw file has a form of 2D matrix and is transformed into 3D matrix form to be used as an input data of the SAFT algorithm. The input signal is analyzed by using both the TD-ORTHO-SAFT and the FD-ORTHO-SAFT algorithms. The damage and the back wall are marked with a red-dotted line in B-scan images.

6.4.1 Scenario 1: One ⌀12.7 mm Damage at Center

The damage for Scenario 1 is located at the center of the specimen as shown in Figure 6.5, and the ultrasonic array is placed along the longitudinal axis. An impulse with a frequency of 45 kHz is used. The B-scan image by the embedded SAFT-C algorithm in A1040 MIRA device is plotted in Figure 6.6. The measured wave velocity of 1416.4 m/s in the tangential coordinate is used for the embedded SAFT algorithm in the device.

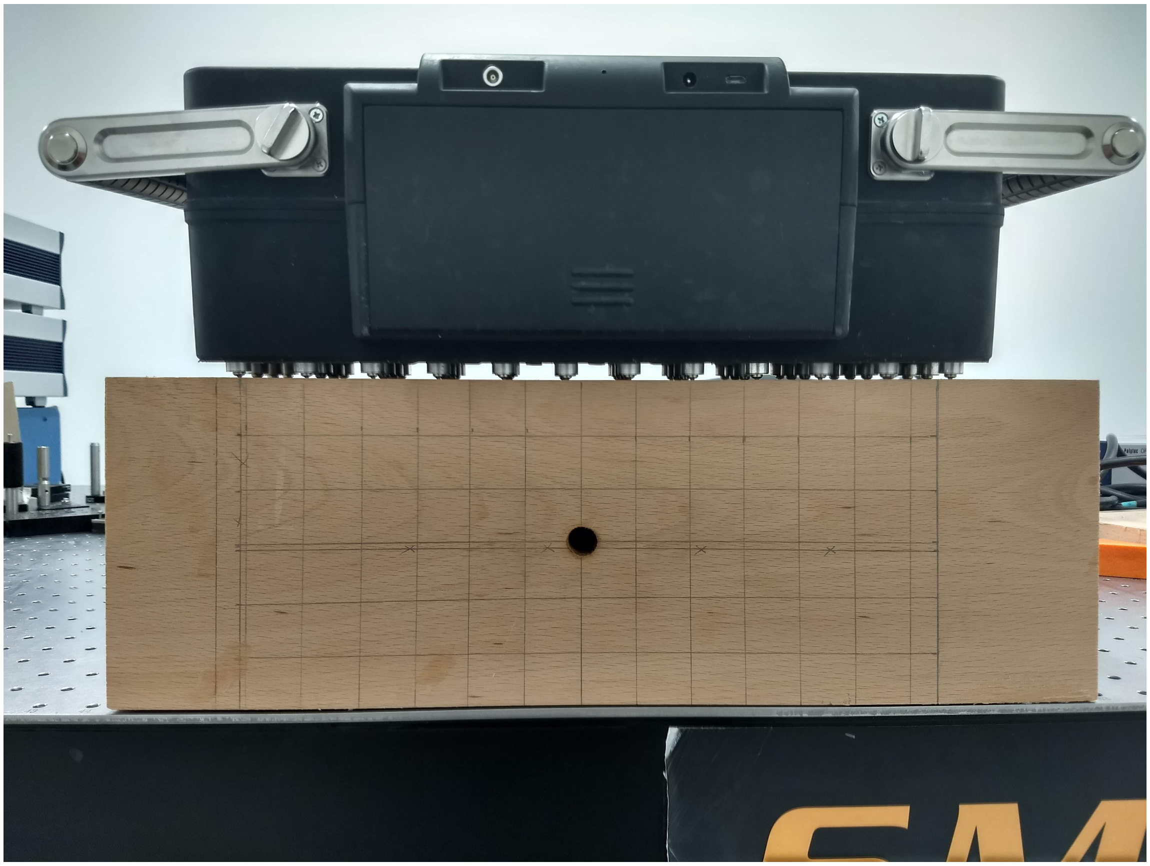

Figure 6.5: Wood Specimen with One ⌀12.7 mm Damage at Center

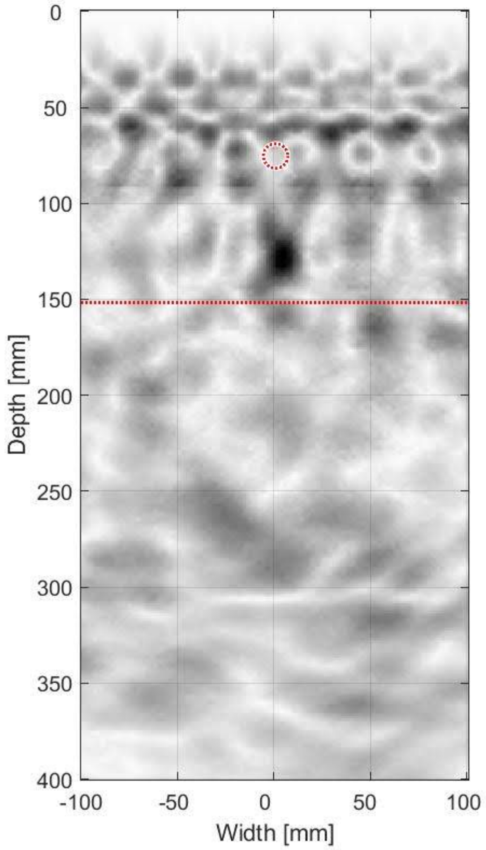

Figure 6.6: B-scan Image of Wood Specimen with One ⌀12.7 mm Damage at Center by A1040 MIRA

A well-focused reflection is located 50 mm down from the exact damage location. This is because the actual wave velocity is slower than the wave velocity in the SAFT algorithm. And, the similar wave velocity to the actual horizontal wave velocity creates a horizontally focused reflection.

Since the specimen is porous wood, significant signal scattering exists near the array, and that phenomenon is expressed as a dense reflection near the array in the B-scan image.

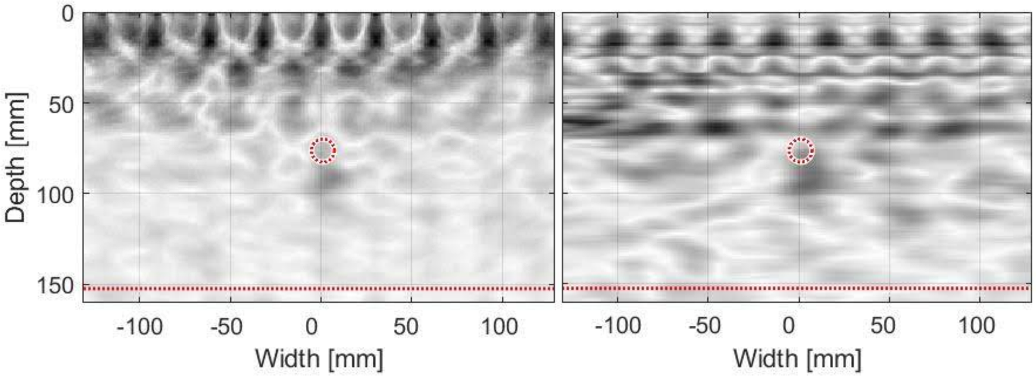

Figure 6.7: B-scan Images of Wood Specimen with One ⌀12.7 mm Damage at Center by the TD-ORTHO-SAFT (left) and by the FD-ORTHO-SAFT (right)

Figure 6.7 shows B-scan images of Scenario #1 by both algorithms. Since the full group velocity information was used in the SAFT algorithm, the expected damage reflection went up close to the exact damage location. Although the location of the reflection came close to the exact damage location, the location of the expected damage reflection is still shifted down from the exact location. This is because of the incorrect group velocity information. In order to obtain more accurate B-scan results, the group velocity information should be measured more accurately to focus reflections at the exact locations.

Intense noise is still located near the surface. This might be because of the natural porosity of the wood and the shear wave's characteristic of not penetrating the liquid or air. If the damage was located near the surface, the damage might not be identifiable.

6.4.2 Scenario 2: Five ⌀12.7 mm Damage at Different Depth

Five ⌀12.7 mm damages are placed at different depths on a specimen as shown in Figure 6.8. Four different frequencies of 25, 45, 65, and 85 kHz are used for an impulse frequency. The corresponding B-scan images by the A1040 MIRA device are plotted in Figure 6.9.

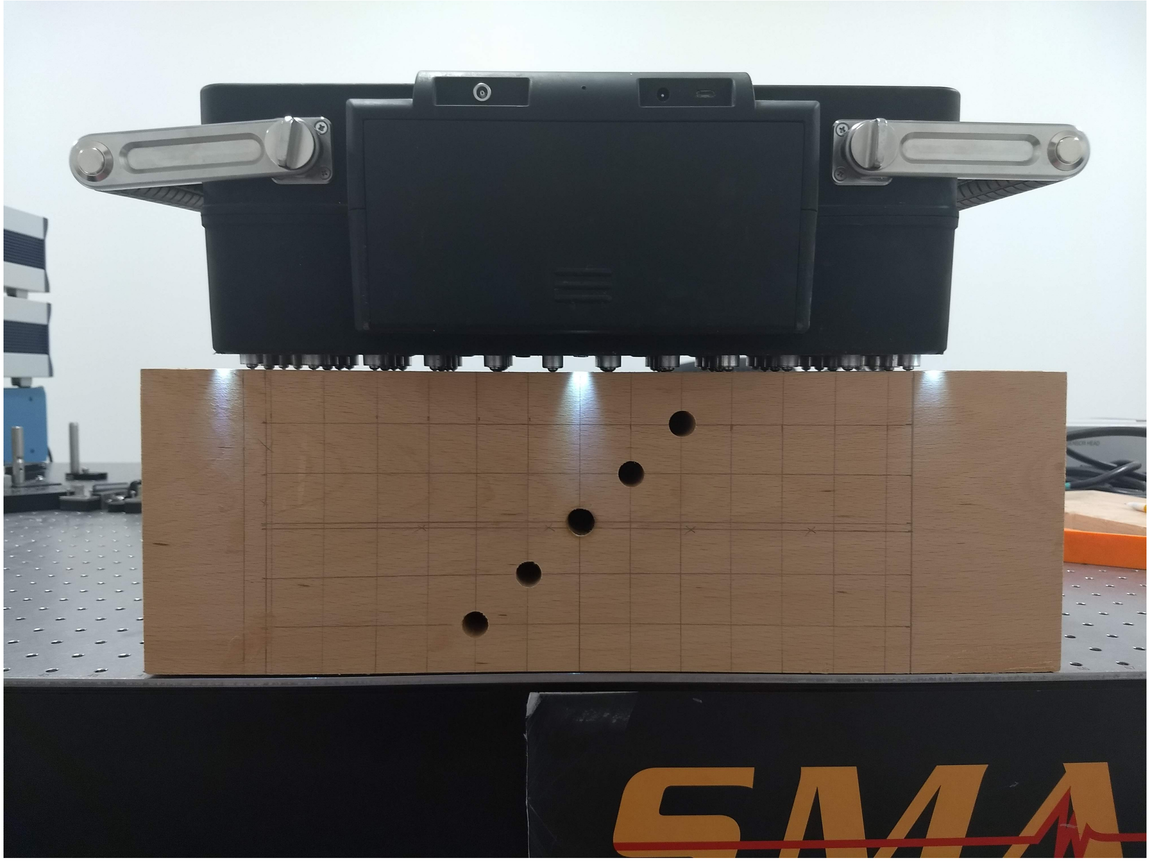

Figure 6.8: Wood Specimen with Five ⌀12.7 mm Damage at Different Depth

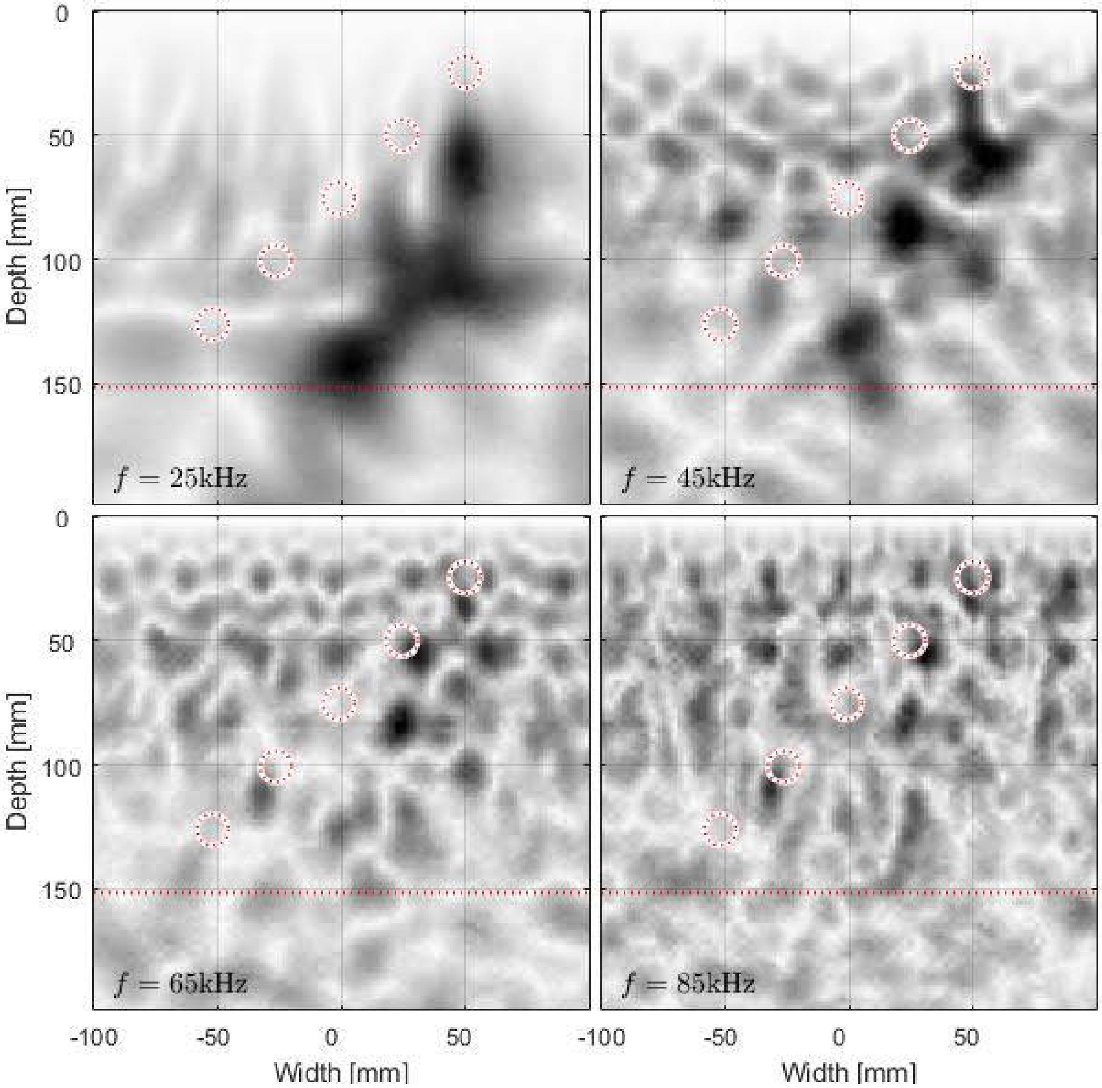

Figure 6.9: B-scan Images of Wood Specimen with Five ⌀12.7 mm Damage at Different Depth and with Different Frequencies by the A1040 MIRA

The measured wave velocity along the tangential coordinate is also used in these B-scan images. Because the group velocity curve for the SAFT algorithm is not identical for the material, expected damage reflections are placed down from the exact damage locations.

As the frequency of the impulse increases, the resolution of the B-scan images is improved, but the noise near the array becomes dense because of the small wavelength of the impulse that cannot pass through the air void in wood. This weakened impulse signal by the small air void cannot go deeper.

The B-scan images by the TD-ORTHO-SAFT and the FD-ORTHO-SAFT algorithm are plotted in Figure 6.10. With the measured group velocity curve, both algorithms show strong reflections going upward in B-scan images compared to the B-scan image by the A1040 MIRA. But, the expected damage locations are still lower than the actual damage locations. This means that the actual group velocity for the wood specimen has a smaller wave velocity than the measured wave velocity in the tangential coordinate.

A cloud-like weak reflection exists diagonally near the damage in the B-scan image by the TD-ORHTO-SAFT for the frequency of 25 kHz. This reflection comes into focus as the impulse frequency increases. However, the faint reflection is hard to be identified among the noise in the wavefield in the B-scan image with a high impulse frequency. Only an overall damage arrangement is indistinctly identifiable in the B-scan image at a low impulse frequency by the TD-ORTHO-SAFT.

Comparing to the B-scan images by the TD-ORTHO-SAFT, the FD-ORTHO-SAFT generates strong reflections. Three isolated damage reflections near the array are identified. Although three damages near the array are identifiable in the B-scan image with the frequency of 25 kHz, nonthing is identifiable in the B-scan image with the frequency of 85 kHz when the diameter of the circular damage is 12.7 mm.

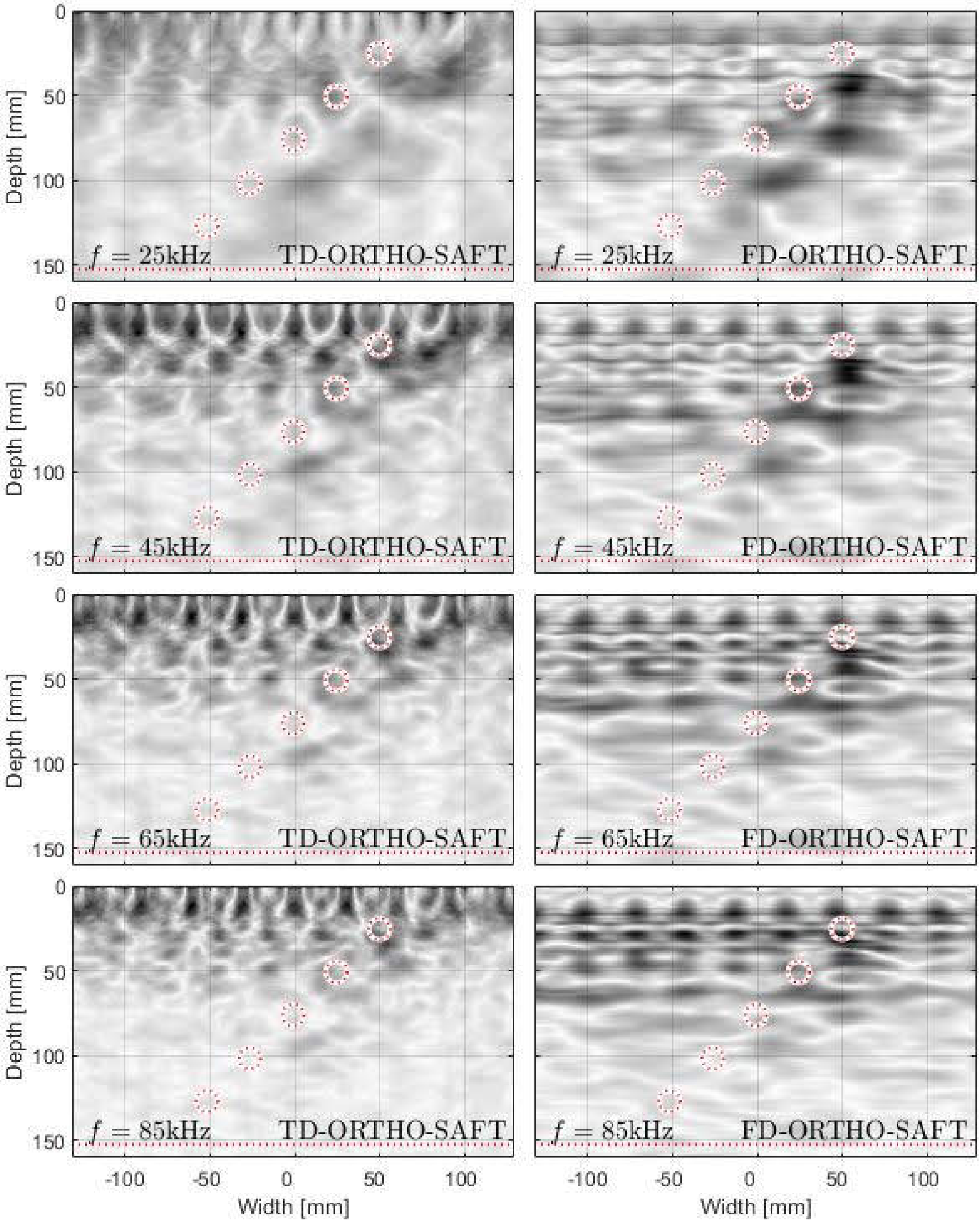

Figure 6.10: B-scan Images of Wood Specimen with Five ⌀12.7 mm Damage at Different Depth and with Different Frequencies by the TD-ORTHO-SAFT (left) and by the FD-ORTHO-SAFT (right)

6.4.3 Scenario 3: Five ⌀25.4 mm Damage at Different Depth

The damage size for Scenario 3 increases from 12.7 mm to 25.4 mm. The arrangement of damage equals to Scenario 2. The wood specimen for Scenario 3 is shown in Figure 6.11.

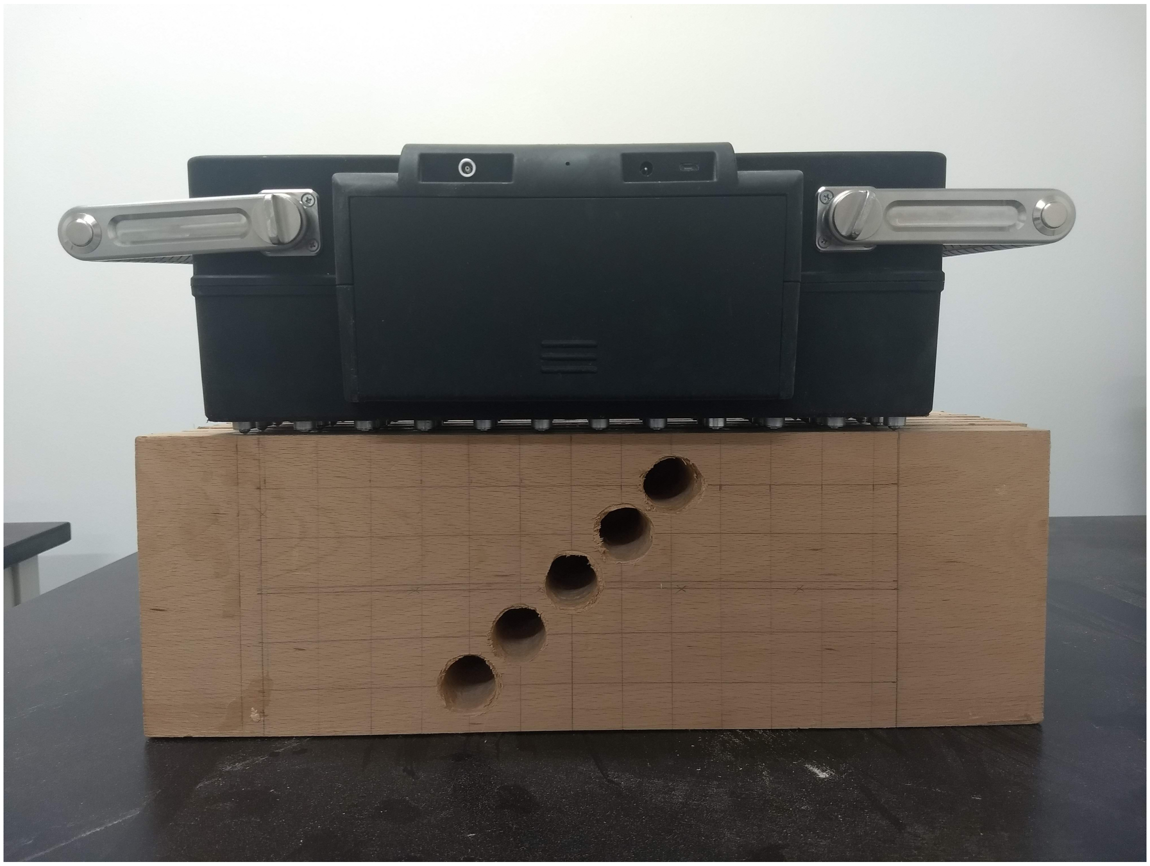

Figure 6.11: Wood Specimen with Five ⌀25.4 mm Damage at Different Depth

B-scan images by the A1040 MIRA device are shown in Figure 6.12. In this figure, the expected damage reflection seems to be stronger than the one in the B-scan image for smaller damage. Besides, an extra reflection exists below the expected damage reflections. Generally speaking, there is a phenomenon called a secondary reflection

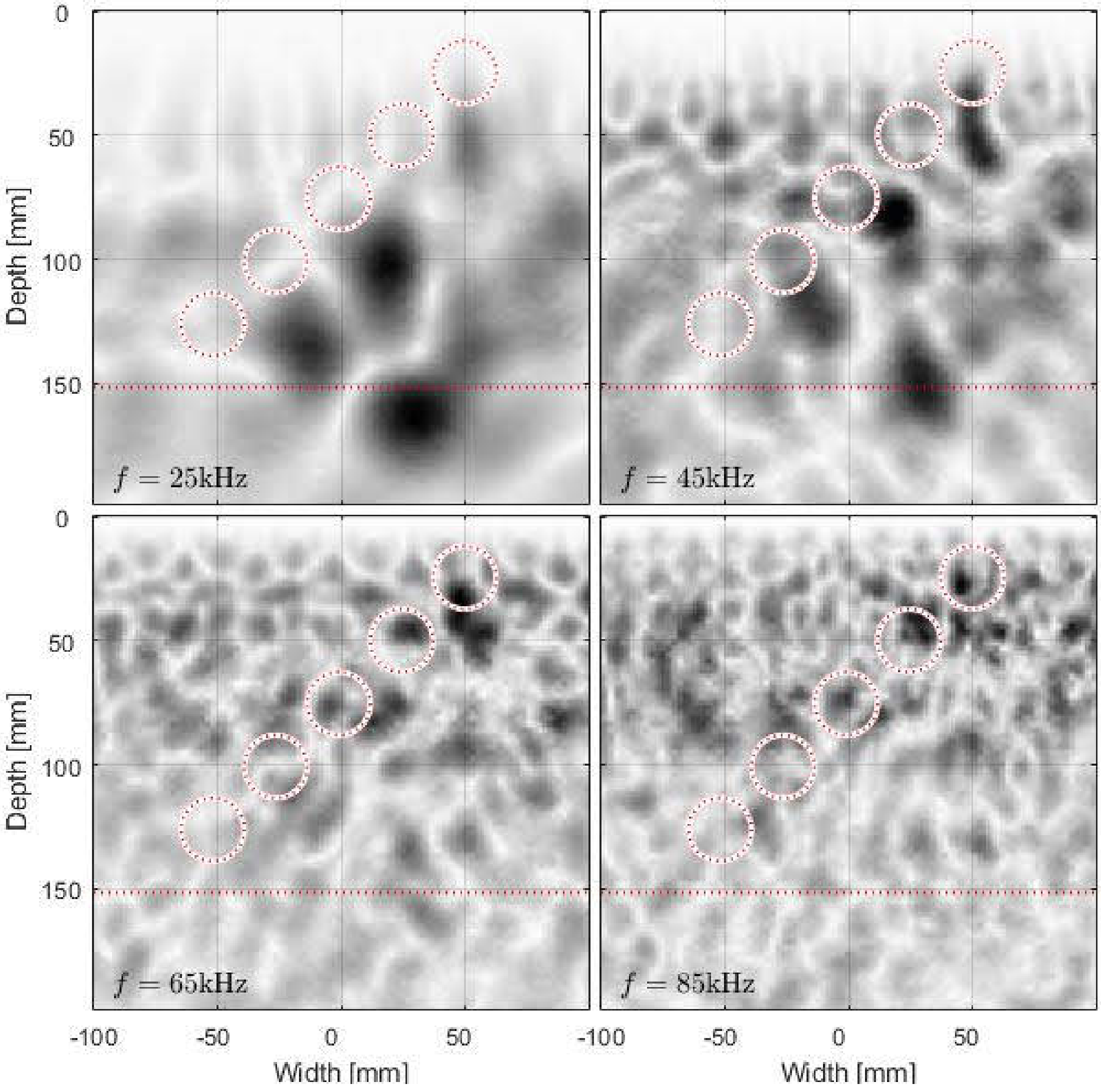

Figure 6.12: B-scan Images of Wood Specimen with Five ⌀25.4 mm Damage at Different Depth and with Different Frequencies by the A1040 MIRA

in a B-scan image. Once an impulse is fired at a transmitter, the impulse is reflected at damage or reflector, then recorded at a receiver. If the reflected signal is strong enough, the reflected signal will penetrate again toward the wave field and is recorded again at the receiver after the re-reflection at the damage or reflector. This secondary reflection creates a weaker reflection than an original one below the expected damage location in a B-scan image. The location of the secondary reflection is exactly twice as far as the original reflection is from the array. However, the reflection at the bottom side in the B-scan image for the frequency of 25 kHz is equivalent or more intense than the reflection above it, and the distance to the reflection is not exactly twice as far from the array as from the above reflection. Therefore, it might be concluded that the reflection indicates innate damage on the wood specimen. A different intensity and location of this reflection in other B-scan images makes the reflection to be seen as a secondary reflection.

The B-scan images by the TD-ORTHO-SAFT and the FD-ORTHO-SAFT are shown in Figure 6.13. Since these algorithms use the measured group velocity curve, the expected damage locations get closer to the actual damage locations. The FD-ORTHO-SAFT shows intenser reflections near the actual damage than the TD-ORTHO-SAFT while reflections in the B-scan image by the TD-ORTHO-SAFT are hard to be distinguished by noise in the wave field.

Compared with the B-scan images for ⌀12.7 mm damage, reflections do not tell the individual damage. This might be because of the large size of the holes which make the entire damage to be seen as single big diagonal damage. A secondary reflection can be seen in the B-scan image by FD-ORTHO-SAFT just below the expected damage location. Since the shapes of the reflections are irregular from image to image, it is hard to say that it is innate damage or a secondary reflection.

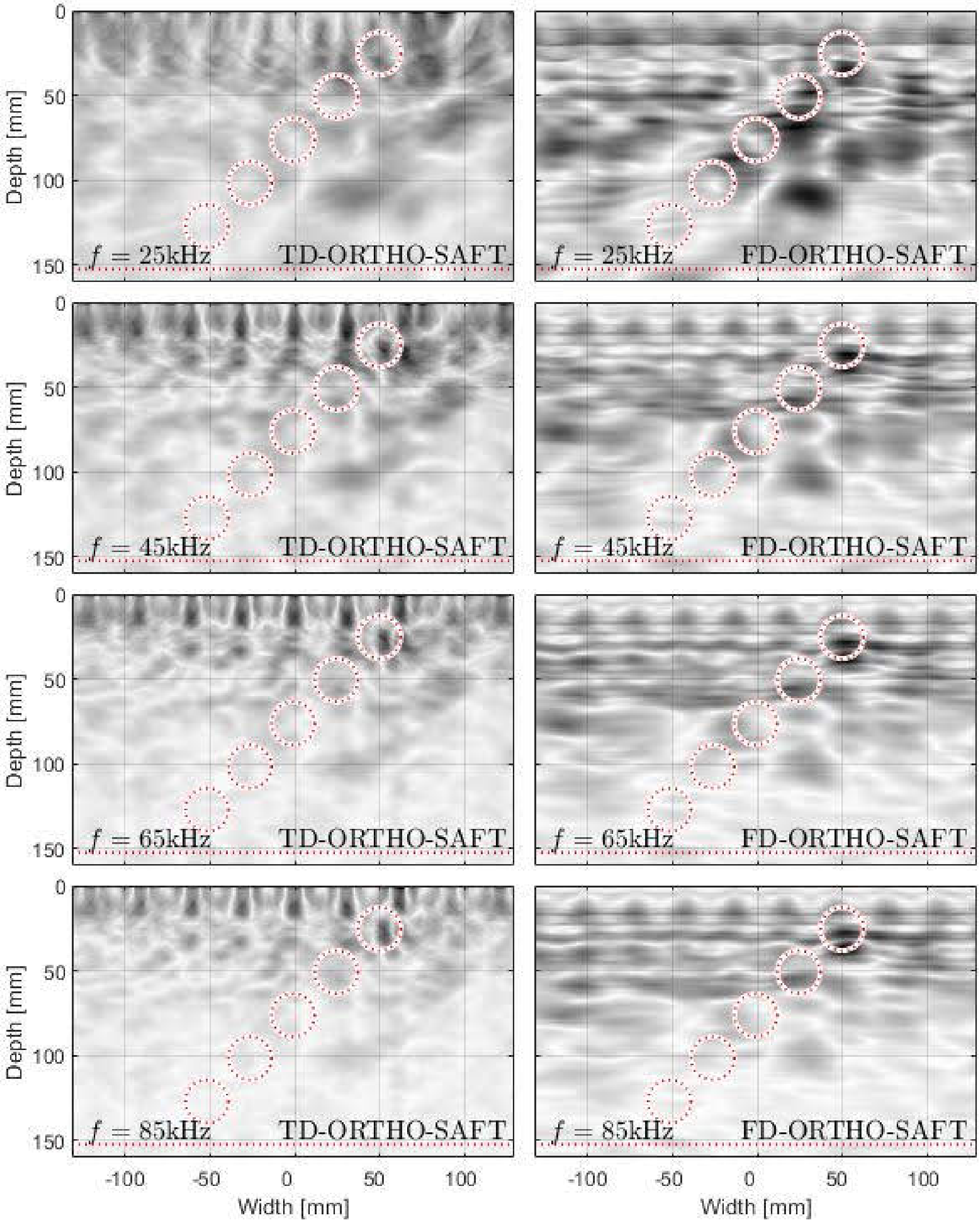

Figure 6.13: B-scan Images of Wood Specimen with Five ⌀25.4 mm Damage at Different Depth and with Different Frequencies by the TD-ORTHO-SAFT (left) and by the FD-ORTHO-SAFT (right)

6.4.4 Scenario 4: Three ⌀25.4 mm Damage at Different Depth

Another wood specimen for Scenario 4 is shown in Figure 6.14. In the previous scenario, the arrangement of damage close to each other makes the entire damage to be seen as one damage. Hence, a moderate distance is deployed between damages.

Figure 6.14: Wood Specimen with Three ⌀25.4 mm Damage at Different Depth

The B-scan images by the A1040 MIRA device are shown in Figure 6.14. In these images, similar phenomena, which is a down-shifting from the exact damage location, with the previous images can be seen. The expected damage reflection for the damage in the depth of 101.6 mm is not shown even in the B-scan image for

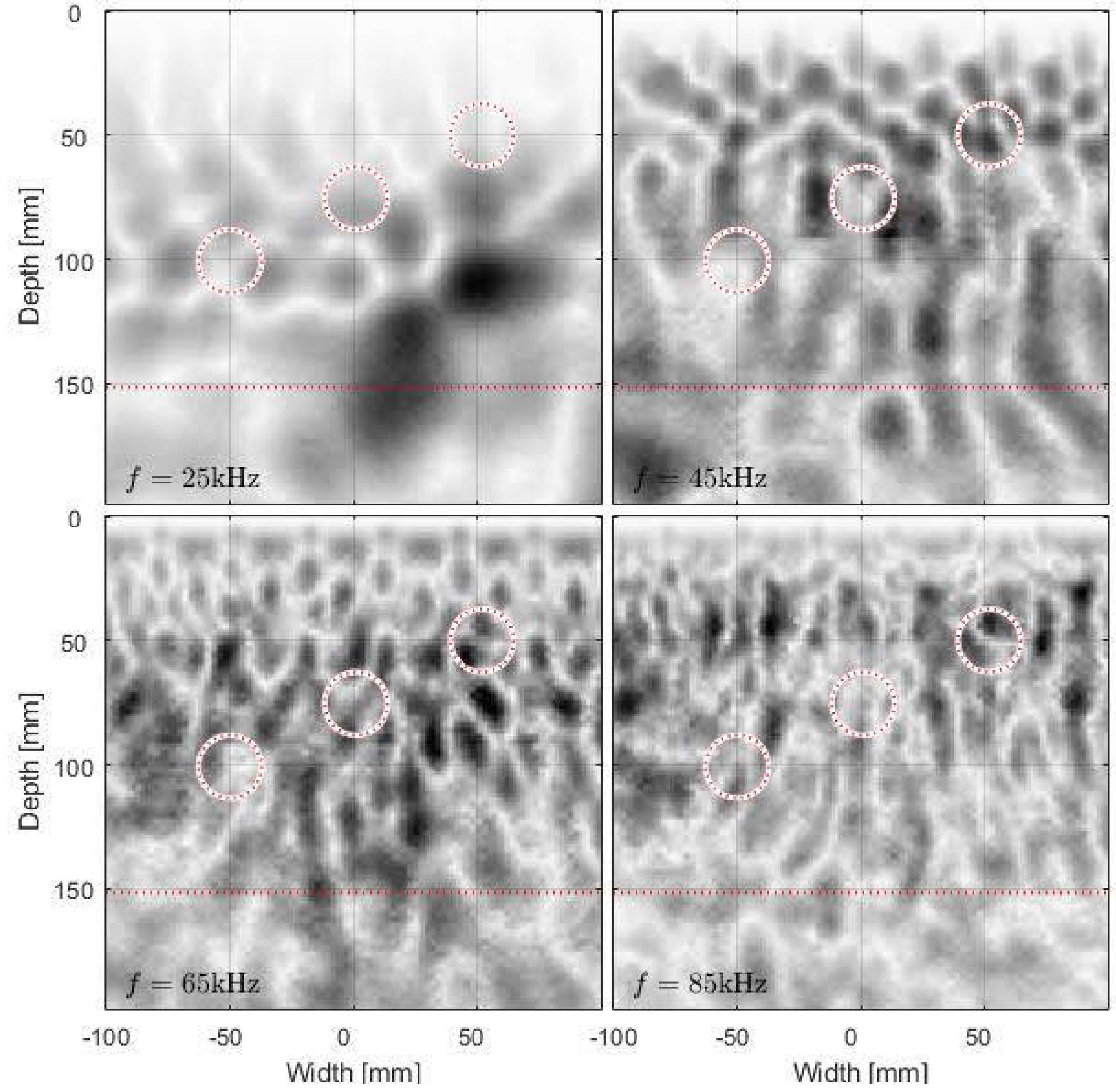

Figure 6.15: B-scan Images of Wood Specimen with Three ⌀25.4 mm Damage at Different Depth and with Different Frequencies by the A1040 MIRA

the frequency of 25 kHz. For this scenario, an expected-damage-like reflection is not shown in images for the frequencies above 25 kHz.

The B-scan images by the TD-ORTHO-SAFT and the FD-ORTHO-SAFE are plotted in Figure 6.16. In the B-scan image by the FD-ORTHO-SAFT for the frequency of 25 kHz, the expected damage reflections seem to be separated as the spacing between damages is stretched. But, these reflections seem to disappear in the images for the high frequency above 25 kHz. In the images by the TD-ORTHO-SAFT, nothing is seen as a damage reflection. This might be because of the short wavelength, high noise intensity, or inaccurate group velocity curve. In Figure 4.5, the B-scan image for simulated ultrasonic array signal with a non-identical group velocity curve between the material and the SAFT algorithm is shown. In comparison to the B-scan of the FD-ORTHO-SAFT, the TD-ORTHO-SAFT cannot provide a focused reflection in B-scan images with a similar group velocity curve with the material. This characteristic of the TD-ORTHO-SAFT might cause the lower detectability in these images for the experiment.

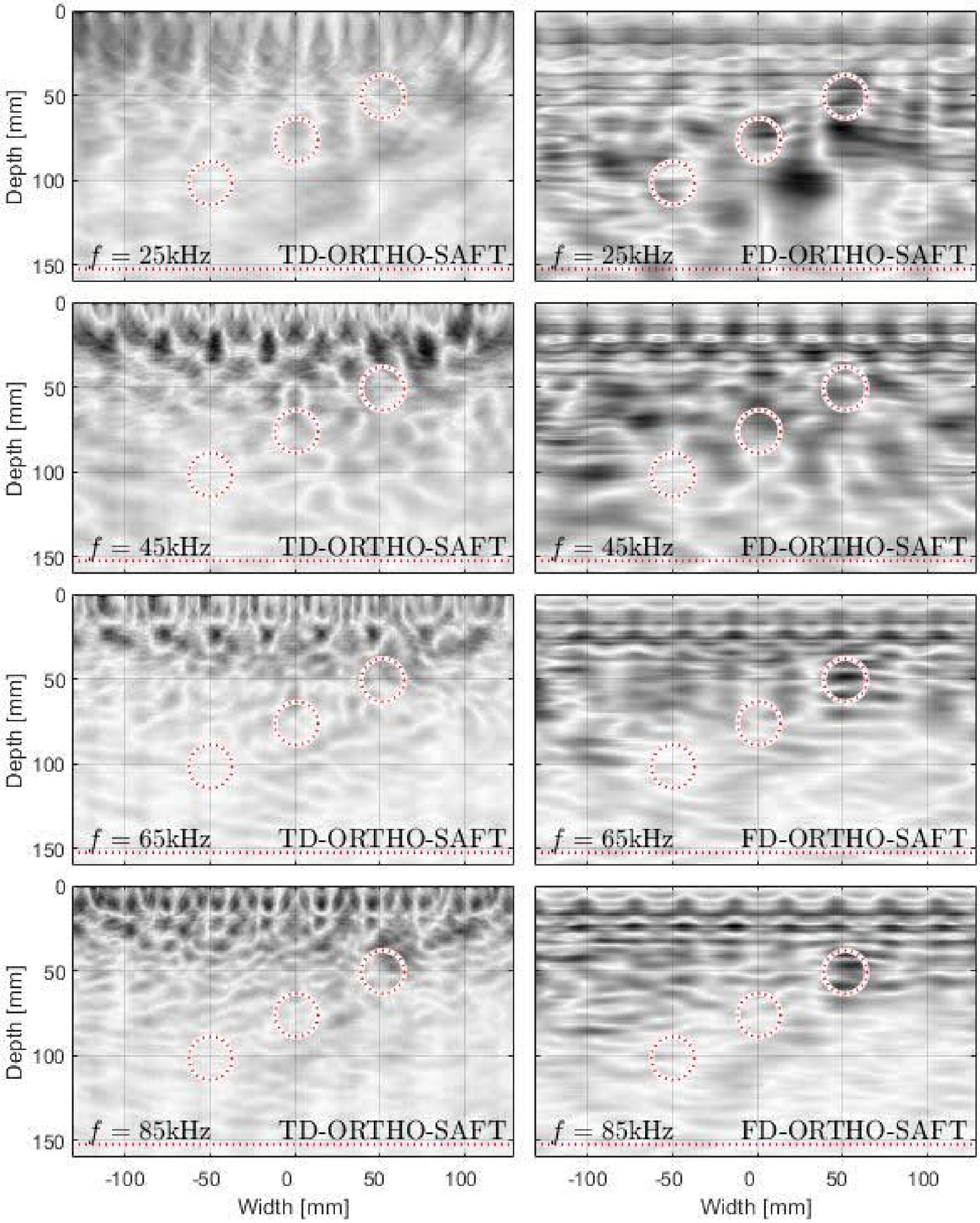

Figure 6.16: B-scan Images of Wood Specimen with Three ⌀25.4 mm Damage at Different Depth and with Different Frequencies by the TD-ORTHO-SAFT (left) and by the FD-ORTHO-SAFT (right)

7. SUMMARIES, CONCLUSIONS, AND FUTURE WORKS

An image reconstruction algorithm for the ultrasonic array device MIRA has been developed. It has a fast computation speed to inspect orthotropic media like wood products. The MIRA device is a bi-static system that creates all possible transducer signal pairs containing more information than a mono-static system. This type of system usually requires large computation loads. The developed FD-ORTHO-SAFT algorithm processes an input data in the wavenumber-frequency domain using the FFT technique, which shows a faster computation speed than the existing TD-ORTHO-SAFT algorithm if a microprocessor is good enough.

7.1 SIMULATION SUMMARIES

In order to validate the developed algorithm, two simulation methods were used to generate a simulated ultrasonic array signal - the mathematical model and the FDTD method. The performance of the algorithm was calculated using the API, performance map, potential damage curve, and computation time. The simulation results are summarized as follows:

- The FD-ORTHO-SAFT algorithm indicated the location of damage even with the limited information of the group velocity curve.
- The FD-ORTHO-SAFT better detects damage with the simulated ultrasonic array noised signal than the TD-ORTHO-SAFT.
- The performance of both algorithms seemed to be similar when using the parameters equivalent to the MIRA device, but the FD-ORTHO-SAFT showed unstable variance at the side of the array.

- When the spatial frequency of the array increased or the wave velocity increased, the performance of the FD-ORTHO-SAFT algorithm improved while the performance of the TD-ORTHO-SAFT was identical.
- The FD-ORTHO-SAFT had a computation speed of less than a second for a typical image size of the MIRA device, while the TD-ORTHO-SAFT showed a slower computation speed.

7.2 EXPERIMENT SUMMARIES

The feasibility of the developed FD-ORTHO-SAFT algorithm was tested for in-situ inspection using wood specimens. The TD-ORTHO-SAFT algorithm also performed to compare the performance of the FD-ORTHO-SAFT algorithm. The results of the experiment are summarized below:

- In order to apply the SAFT algorithm to in-situ inspection, knowing the group velocity curve for the material is essential.
- The group velocity curve for the material was assumed to be an ellipse. This assumption worked well for both the FD-ORTHO-SAFT and the TD-ORTHO-SAFT algorithms to assess the wood specimens.
- The FD-ORTHO-SAFT algorithm detected damage better than the TD-ORTHO-SAFT algorithm in the experiment. The expected damage reflection on the B-scan image by the embedded SAFT algorithm for isotropic media in the MIRA device did not appear in the B-scan image by the TD-ORTHO-SAFT. This might be because of the fact that the assumed group velocity curve used in the TD-ORTHO-SAFT is not identical, but similar to the actual group velocity curve. And the performance of the TD-ORTHO-SAFT was sensitive to the shape of assumed group velocity curve.

- Due to the significant signal attenuation of the shear wave on wood, damage in the depth up to around 75 mm was only detectable by the SAFT algorithm with a low impulse frequency. If the impulse frequency increased over 60 kHz, nothing could be detected because of the severe noise near the surface.

7.3 CONCLUSIONS

Based on the simulation and experimental results, overall conclusions are summarized as follows:

- The FD-ORTHO-SAFT is more suitable for an inspecting method for general wood products than the TD-ORTHO-SAFT in terms of detectability. Most wood products have a longitudinal coordinate along the length of the products, and an ultrasonic array device has to approach the wood product perpendicular to the length. This means that the shape of the group velocity curve is a vertically compressed form, and the FD-ORTHO-SAFT shows a better performance than the TD-ORTHO-SAFT with the vertically-compressed group velocity curve.

- The FD-ORTHO-SAFT has a faster computation speed than the TD-ORTHO-SAFT. Since the computation speed of the FD-ORTHO-SAFT algorithm is affected more by a microprocessor clock speed than by the size of memory, unlike the TD-ORTHO-SAFT, the improvement of the computation speed of the FD-ORTHO-SAFT would be better than the TD-ORTHO-SAFT if a faster microprocessor is used.

7.4 FUTURE STUDIES

Future studies to extend the results of this research should include the following:

- Further research about using a compressive wave instead of a shear wave for the ultrasonic array system is required. Since the shear wave cannot penetrate fluid media like liquid and air, signal attenuation of shear wave in the wood specimen was significant. In this research, damage in a depth of up to around 75 mm was identifiable. On the other hand, the compressive wave can penetrate air and liquid media and can provide more reflected signals than the shear wave. Also, research about an additional effects of compressive wave such as mode conversion should be conducted simultaneously.

- An advanced method for measuring group velocity curve for wood is necessary. The measuring method used in this research is not practical, and it is difficult to determine the group velocity curve based on the wood species because the material property of wood varies by species and even by part. Thus, a new method for figuring out the group velocity curve of a wood product is required for the SAFT algorithm to assess the wood product precisely.

- A new SAFT algorithm is required for different geometries of ultrasonic arrays. The arrangement of the ultrasonic array in the A1040 MIRA device is fixed for general purposes. The A1040 MIRA device has a linearly placed ultrasonic array. However, in reality, accessible surfaces are not limited to a single surface. If the ultrasonic array technique flexibly accesses the surfaces of an element to be assessed, the resulting B-scan image by the ultrasonic array system will become more comprehensive. Accordingly, developing a new SAFT algorithm is required for various geometries of ultrasonic arrays.

- A new interpolation technique for an ultrasonic array signal is needed. The FD-SAFT algorithm employs an FFT technique to transfer an array signal from a time-distance to a frequency-wavenumber domain to manipulate data.

A basic assumption of the FFT technique is that the data points are evenly distributed. However, if an ultrasonic array has different spacings between transducers or has different vertical locations because of an uneven surface condition, the measured ultrasonic array data has to be interpolated to have a constant data interval. Unlike a typical interpolation method for increasing the resolution of data, a new interpolation method for the ultrasonic array signal has to translate recorded impulses at one point into an appropriate time point corresponding to the geometry of the ultrasonic array and the wave propagation properties.

REFERENCES

Abbott, A. and L. Whale

1987. An overview of the use of glued laminated timber (glulam) in the UK. *Construction and Building Materials*, 1(2):104–110.

Arriaga, F., G. Íniguez, M. Esteban, and J. I. Fernández-Golfín

2006. Structural tali timber (erythrophleum ivorense a. chev., erythrophleum suaveolens brenan.): Assessment of strength and stiffness properties using visual and ultrasonic methods. *Holz als Roh-und Werkstoff*, 64(5):357–362.

Balendra, T., J. L. Wilson, and E. Gad

2010. Review of condition assessment and retrofitting techniques for timber bridge assets in Australia. *Advances in Structural Engineering*, 13(1):171–180.

Berglind, H.

2003. *Non-destructive detection of glue deficiency in laminated wood using thermography.* Ph.D dissertation, Luleå Tekniska Universitet.

Berglind, H. and A. Dillenz

2003. Detection of glue deficiency in laminated wood with pulse thermography. *Journal of Wood Science*, 49(3):216–220.

Bieker, D., R. Kehr, G. Weber, and S. Rust

2010. Non-destructive monitoring of early stages of white rot by trametes versicolor in fraxinus excelsior. *Annals of Forest Science*, 67(2):210.

Brashaw, B. K., R. J. Vatalaro, J. P. Wacker, and R. J. Ross

2005. Condition assessment of timber bridges. 1. evaluation of a micro-drilling resistance tool. Technical report, Forest Products Lab Madison WI.

Breyer, D. E., K. J. Fridley, K. E. Cobeen, and D. G. Pollock

1999. *Design of wood structures ASD*. McGraw-Hill New York.

Bucur, V.

2005. Ultrasonic techniques for nondestructive testing of standing trees. *Ultrasonics*, 43(4):237–239.

Bucur, V. and I. Böhnke

1994. Factors affecting ultrasonic measurements in solid wood. *Ultrasonics*, 32(5):385–390.

Bucur, V. and F. Feeney

1992. Attenuation of ultrasound in solid wood. *Ultrasonics*, 30(2):76–81.

Calderoni, C., G. De Matteis, C. Giubileo, and F. Mazzolani

2010. Experimental correlations between destructive and non-destructive tests on ancient timber elements. *Engineering Structures*, 32(2):442–448.

Carrasco, E. V. M. and A. R. Teixeira

2012. Methodology for inspection of wood pathologie using ultrasonic pulses. *Cerne*, 18(3):479–486.

Ceraldi, C., V. Mormone, and E. R. Ermolli

2001. Resistographic inspection of ancient timber structures for the evaluation of mechanical characteristics. *Materials and Structures*, 34(1):59–64.

Chen, S., X. Liu, L. Fang, and R. Wellwood

2010. Digital x-ray analysis of density distribution characteristics of wood-based panels. *Wood Science and Technology*, 44(1):85–93.

Chew, W. C.

1995. *Waves and fields in inhomogeneous media*. IEEE press.

Choi, F., B. Samali, J. Li, P. Brown, and U. Dackermann

2005. Investigation on the dynamic response of a damaged timber bridge. In *11th Asia-Pacific Vibration Conference, Langkawi, Malaysia*.

Conde, M. M., C. R. Liñán, and P. R. de Hita

2014. Use of ultrasound as a nondestructive evaluation technique for sustainable interventions on wooden structures. *Building and Environment*, 82:247–257.

Costello, L. R. and S. L. Quarles

1999. Detection of wood decay in blue gum and elm: an evaluation of the resistograph® and the portable drill. *Journal of Arboriculture*, 25:311–318.

Cown, D. J. and B. Clement

1983. A wood densitometer using direct scanning with x-rays. *Wood Science and Technology*, 17(2):91–99.

Dackermann, U., K. Crews, B. Kasal, J. Li, M. Riggio, F. Rinn, and T. Tannert

2014. In situ assessment of structural timber using stress-wave measurements. *Materials and Structures*, 47(5):787–803.

Dackermann, U., J. Li, and B. Samali

2009. Damage identification in timber bridges utilising the damage index method and neural network ensembles. *Australian Journal of Structural Engineering*, 9(3):181–194.

Dackermann, U., J. Li, and B. Samali

2010. Dynamic-based damage identification using neural network ensembles and damage index method. *Advances in Structural Engineering*, 13(6):1001–1016.

Dackermann, U., J. C. Li, R. Rijal, and B. Samali

2013. A vibration-based approach for the estimation of the loss of composite action in timber composite systems. In *Advanced Materials Research*, volume 778, Pp. 462–469. Trans Tech Publ.

Dinwoodie, J.

1975. Timber—a review of the structure-mechanical property relationship. *Journal of Microscopy*, 104(1):3–32.

Divos, F., S. Szegedi, and P. Raics

1996. Local densitometry of wood by gamma back-scattering. *Holz als Roh-und Werkstoff*, 54(4):279–281.

Dzbeński, W. and T. Wiktorski

2007. Ultrasonic evaluation of mechanical properties of wood in standing trees. In *COST E 53 conference—quality control for wood and wood products, Warsaw*, Pp. 15–17. Citeseer.

Emerson, R. N., D. G. Pollock, D. I. McLean, K. J. Fridley, R. J. Ross, and R. E. Pellerin

1999. Nondestructive testing of large bridge timbers. In *Proceedings or the 11th International Symposium on Nondestructive Testing of Wood*, Pp. 175–185.

Fleming, M. R., D. K. Agrawal, M. C. Bhardwaj, L. S. Bauer, J. J. Janowiak, J. E. Shield, K. Hoover, and R. Roy

2005. Noncontact ultrasound detection of exotic insects in wood packing materials. *Forest Products Journal*, 55(6):33–37.

França, F., G. Vidaurre, L. Nutto, X. Wang, J. T. d. S. Oliveira, and T. Biechele

2013. Nondestructive assessment of Schizolobium amazonicum with stress wave tomography. In *Proceedings of the 18th International Nondestructive Testing and Evaluation of Wood Symposium*, Pp. 716–722.

Frese, M. and H. J. Blaß

2011. Statistics of damages to timber structures in Germany. *Engineering Structures*, 33(11):2969–2977.

Gilbert, E. A. and E. T. Smiley

2004. Picus sonic tomography for the quanification of decay in white oak (quercus alba) and hickory (carya spp.). *Journal of Arboriculture*, 30(5):277–281.

Gupta, N. K., D. L. Schmoldt, and B. Isaacson

1999. Tangential scanning of hardwood logs: developing an industrial computer tomography scanner. In *Proceedings of the 11th International Symposium on Nondestructive Testing of Wood. 131-139.*

Gutkowski, R. M. and T. G. Williamson

1983. Timber bridges: State-of-the-art. *Journal of Structural Engineering*, 109(9):2175–2191.

Halabe, U. B., S. Agrawal, and B. Gopalakrishnan

2009. Nondestructive evaluation of wooden logs using ground penetrating radar. *Nondestructive Testing and Evaluation*, 24(4):329–346.

Hasenstab, A., B. Hillemeier, and M. Krause

2005. Defect localisation in wood with low frequency ultrasonic echo technique. In *Proceedings of the 14th International Symposium on Nondestructive Testing of Wood*, volume 2, P. 2005.

Hasenstab, A., M. Krause, C. Rieck, and B. Hillemeier

2003. Use of low frequency ultrasound echo technique to determine cavities in wooden construction composites. In *Proceedings of the International Symposium Non-Destructive Testing in Civil Engineering (NDT-CE), DGZfP (Ed.), BB.*

Hasenstab, A. and K. Osterloh

2009. Defects in wood non destructive locating with low frequency ultrasonic echo technique. In *7th International Symposium on Nondestructive Testing in Civil Engineering, Nantes, France.* Citeseer.

Hoegh, K. E.

2013. *Ultrasonic linear array evaluation of concrete pavements.* Ph.D dissertation, University of Minnesota.

Holmes, C., B. W. Drinkwater, and P. D. Wilcox

2005. Post-processing of the full matrix of ultrasonic transmit–receive array data for non-destructive evaluation. *NDT & e International*, 38(8):701–711.

Hunt, M. O., R. J. Ross, X. Wang, L. A. Soltis, R. Leavitt, and Z. Cai

2007. Assessment of in-place wood floor systems. *Journal of Architectural Engineering*, 13(1):30–35.

Hunter, A. J., B. W. Drinkwater, and P. D. Wilcox

2008. The wavenumber algorithm for full-matrix imaging using an ultrasonic array. *IEEE Transactions on Ultrasonics, Ferroelectrics and Frequency Control*, 55(11):2450–2462.

Isik, F. and B. Li

2003. Rapid assessment of wood density of live trees using the resistograph for selection in tree improvement programs. *Canadian Journal of Forest Research*, 33(12):2426–2435.

Johnstone, D. M., P. K. Ades, G. M. Moore, and I. W. Smith

2007. Predicting wood decay in eucalypts using an expert system and the IML-Resistograph drill. *Arboriculture and Urban Forestry*, 33(2):76.

Kasal, B.

2003. Semi-destructive method for in-situ evaluation of compressive strength of wood structural members. *Forest Products Journal*, 53(11/12):55–58.

Kolb, J.

2008. *Systems in timber engineering: loadbearing structures and component layers*. Walter de Gruyter.

Krause, M., K. Mayer, P. K. Chinta, and U. Effner

2013. Ultrasonic imaging of defects in building elements made from timber. *Advanced Materials Research*, 778:312–320.

Larsson, B., B. Bengtsson, and M. Gustafsson

2004. Nondestructive detection of decay in living trees. *Tree Physiology*, 24(7):853–

858.

Laufenberg, T. L.

1986. Using gamma radiation to measure density gradients in reconstituted wood products. *Forest Products Journal*, 36(2):59–62.

Lechner, T., Y. Sandin, and R. Kliger

2013. Assessment of density in timber using x-ray equipment. *International Journal of Architectural Heritage*, 7(4):416–433.

Liang, S., X. Wang, J. Wiedenbeck, Z. Cai, and F. Fu

2008. Evaluation of acoustic tomography for tree decay detection. In *Proceedings of the 15th international symposium on nondestructive testing of wood; 2007 September 10-12; Duluth, MN. Forest Products Society: 49-54.*

Lin, C.-J., T.-T. Chang, M.-Y. Juan, T.-T. Lin, C.-L. Tseng, Y.-N. Wang, M.-J. Tsai, et al.

2011. Stress wave tomography for the quantification of artificial hole detection in camphor trees (cinnamomum camphora). *Taiwan Journal of Forest Science*, 26(1):17–32.

Lin, C.-J., Y.-C. Kao, T.-T. Lin, M.-J. Tsai, S.-Y. Wang, L.-D. Lin, Y.-N. Wang, and M.-H. Chan

2008. Application of an ultrasonic tomographic technique for detecting defects in standing trees. *International Biodeterioration & Biodegradation*, 62(4):434–441.

López, G., L.-A. Basterra, G. Ramón-Cueto, and A. d. Diego

2014. Detection of singularities and subsurface defects in wood by infrared thermography. *International Journal of Architectural Heritage*, 8(4):517–536.

Maack, S. and M. Krause

2008. Diagnostic investigations of wooden structures using ultrasonic-echo technique. In *Proceedings of the 1st International RILEM Conference, on Site Assess-*

ment of Concrete, Masonry and Timber Structures (SACoMaTiS), Pp. 1081–1090.

Machado, J., P. Palma, and S. Simões

2009. Ultrasonic indirect method for evaluating clear wood strength and stiffness. In *Proceedings of the 7th International Symposium on Non-destructive Testing in Civil Engineering*, Pp. 969–974.

Machado, J. S. and P. Palma

2011. Non-destructive evaluation of the bending behaviour of in-service pine timber structural elements. *Materials and Structures*, 44(5):901–910.

Marchetti, B., R. Munaretto, G. Revel, E. P. Tomasini, and V. B. Bianche

2004. Non-contact ultrasonic sensor for density measurement and defect detection on wood. In *Proceedings of the 16th World Conference on Nondestructive Testing*, Pp. 14–21.

Meinlschmidt, P.

2005. Thermographic detection of defects in wood and wood-based materials. In *14th International Symposium of Nondestructive Testing of Wood, Hannover, Germany.*

Moody, R. and M. Ritter

1990. Structural wood products. In *Serviceability and Durability of Construction Materials*, Pp. 41–52. Citeseer.

Müller, U., R. Bammer, E. Halmschlager, R. Stollberger, and R. Wimmer

2001. Detection of fungal wood decay using magnetic resonance imaging. *European Journal of Wood and Wood Products*, 59(3):190–194.

Nicholson, C.

2013. Controlling wood movement: The drying process. `https://www.core77.com/posts/25085/controlling-wood-movement-the-drying-process-25085`. Online; accessed 7-November-2019.

Oja, J.

1999. *X-ray measurement of properties of saw logs.* Ph.D dissertation, Luleå Tekniska Universitet.

Oja, J., S. Grundberg, and A. Grönlund

2001. Predicting the stiffness of sawn products by x-ray scanning of Norway spruce saw logs. *Scandinavian Journal of Forest Research*, 16(1):88–96.

Oliveira, F. G. R., M. Candian, F. F. Lucchette, J. L. Salgon, and A. Sales

2005. A technical note on the relationship between ultrasonic velocity and moisture content of Brazilian hardwood (goupia glabra). *Building and Environment*, 40(2):297–300.

Oliveira, F. G. R. and A. Sales

2006. Relationship between density and ultrasonic velocity in Brazilian tropical woods. *Bioresource Technology*, 97(18):2443–2446.

Oliveira, F. G. R. d., J. A. O. d. Campos, and A. Sales

2002. Ultrasonic measurements in Brazilian hardwood. *Materials Research*, 5(1):51–55.

Ozelton, E. C. and J. A. Baird

2006. *Timber Designers' Manual.* Wiley Online Library.

Perlin, L. P., R. C. A. Pinto, and Â. d. Valle

2014. Use of ultrasonic tomography in the evaluation of timber structures. In *11th European Conference on Non-Destructive Testing (ECNDT 2014), Prague 2014, Oct 6-11.*

Rinn, F.

2012. Basics of micro-resistance drilling for timber inspection. *Holztechnologie*, 53(3):24–9.

Ross, R. and R. DeGroot

1998. Scanning technique to identify biologically degraded wood. *Experimental Techniques*, 22(3):32–33.

Ross, R., R. DeGroot, and W. Nelson

1994a. Technique for nondestructive evaluation of biologically degraded wood. *Experimental Techniques*, 18(5):29–32.

Ross, R., X. Wang, M. Hunt, and L. Soltis

2002. Transverse vibration technique to identify deteriorated wood floor systems. *Experimental Techniques*, 26(4):28–30.

Ross, R. J.

2001. *Relationship between stress wave transmission time and compressive properties of timbers removed from service*, volume 280. US Department of Agriculture, Forest Service, Forest Products Laboratory.

Ross, R. J. and R. F. Pellerin

1988. NDE of wood-based composites with longitudinal stress waves. *Forest Products Journal*, 38(5):39–45.

Ross, R. J., R. F. Pellerin, N. Volny, W. W. Salsig, and R. H. Falk

1999. Inspection of timber bridges using stress wave timing nondestructive evaluation tools: a guide for use and interpretation. *(General technical report FPL; GTR-114): 15 p.: ill., map; 28 cm.*, 114.

Ross, R. J., J. C. Ward, and A. TenWolde

1994b. Stress wave nondestructive evaluation of wetwood. *Forest Products Journal*, 44(7/8).

Ross, R. J., J. I. Zerbe, X. Wang, D. W. Green, and R. F. Pellerin

2005. Stress wave nondestructive evaluation of douglas-fir peeler cores. *Forest Products Journal*, 55(3):90–94.

Rust, S.

2000. A new tomographic device for the non-destructive testing of trees. In *12th International Symposium on Nondestructive Testing of Wood, University of Western Hungary, Sopron*, Pp. 233–237.

Sakai, H., A. Minamisawa, and K. Takagi

1990. Effect of moisture content on ultrasonic velocity and attenuation in woods. *Ultrasonics*, 28(6):382–385.

Samali, B., J. Li, U. Dackermann, and F. Choi

2011. Vibration-based damage detection for timber structures in australia. In *Structural Health Monitoring in Australia*, T. Chan and D. P. Thambiratnam, eds., Engineering Tools, Techniques and Tables Series, Pp. 81–108. Nova Science Publishers, Incorporated.

Sanabria, S. J., J. Neuenschwander, P. Niemz, and U. Sennhauser

2010. Structural health monitoring of glued laminated timber with a novel air-coupled ultrasound method. In *Proceedings of the 11th World conference on timber engineering, Riva del Garda, Trentino, Italy.*

Sandoz, J.

1989. Grading of construction timber by ultrasound. *Wood Science and Technology*, 23(1):95–108.

Sandoz, J.

1993. Moisture content and temperature effect on ultrasound timber grading. *Wood Science and Technology*, 27(5):373–380.

Sandoz, J. L.

1996. Ultrasonic solid wood evaluation in industrial applications. In *10th International Symposium on Nondestructive Testing of Wood*, volume 26, P. 1996.

Sasaki, Y., M. Yamasaki, M. Uchida, and T. Torichigai

2014. Non-destructive stress evaluation of wood members in Japanese traditional building. In *11th European Conference on Non-Destructive Testing (ECNDT 2014), Prague 2014, Oct 6-11 (ECNDT 2014).*

Schad, K. C.

1995. *Stress wave techniques for determining quality of dimensional lumber from switch ties*, volume 265. US Dept. of Agriculture, Forest Service, Forest Products Laboratory.

Shaji, T., S. Somayaji, and M. Mathews

2000. Ultrasonic pulse velocity technique for inspection and evaluation of timber. *Journal of Materials in Civil Engineering*, 12(2):180–185.

Skjelvareid, M. H.

2012. *Synthetic aperture ultrasound imaging with application to interior pipe inspection*. Ph.D dissertation, University of Tromsø.

Socco, L., L. Sambuelli, and G. Nicolotti

2004. Ultrasonic tomography for non destructive testing of living trees. In *Gruppo Nazionale di Geofisica della Terra Solida - Atti del 19° Convegno Nazionale*. Consiglio Nazionale delle Ricerche Istituto Nazionale di Oceanografia e di Geofisica Sperimentale, Citeseer.

Soltis, L., M. Hunt, R. Ross, X. Wang, and Z. Cai

1994. Nondestructive structural evaluation of wood floor systems in historic buildings. *USDA Forest Service, Forest Products Laboratory, FPL-GTR-70. Madison, Wisconsin*, 40:279–289.

Song, J., C. Chen, S. Zhu, M. Zhu, J. Dai, U. Ray, Y. Li, Y. Kuang, Y. Li, N. Quispe, et al.

2018. Processing bulk natural wood into a high-performance structural material. *Nature*, 554(7691):224.

Stalnaker, J. and E. Harris

1997. *Structural design in wood.* Springer Science & Business Media.

Stepinski, T. and F. Lingvall

2010. Synthetic aperture focusing techniques for ultrasonic imaging of solid objects. In *8th European Conference on Synthetic Aperture Radar*, Pp. 1–4. VDE.

Stubbs, N. and R. Osegueda

1990. Global non-destructive damage evaluation in solids. *International Journal of Analytical and Experimental Modal Analysis*, 5:67–79.

Tallavo, F., G. Cascante, and M. D. Pandey

2012. A novel methodology for condition assessment of wood poles using ultrasonic testing. *NDT & E International*, 52:149–156.

Tanaka, T. and F. Divós

2000. Wood inspection by thermography. In *Proceedings of the 12th International Symposium on Nondestructive Testing, Sopron*, Pp. 439–447.

Tsvankin, I. D.

2012. *Seismic Signatures and Analysis of Reflection Data in Anisotropic Media, Third Edition.* Society of Exploration Geophysicists.

Tucker, B. J. and D. A. Bender

2003. Continuous ultrasonic inspection of extruded wood-plastic composites. *Forest Products Journal*, 53(6):27.

Veldman, D., I. J. Bennett, B. Brockholz, and P. C. de Jong

2011. Non-destructive testing of crystalline silicon photovoltaic back-contact modules. In *2011 37th IEEE Photovoltaic Specialists Conference*, Pp. 003237–003240. IEEE.

Wang, X., R. J. Ross, M. McClellan, R. J. Barbour, J. R. Erickson, J. W. Forsman, G. D. McGinnis, et al.

2000. *Strength and stiffness assessment of standing trees using a nondestructive* *stress wave technique*. United States Department of Agriculture, Forest Service, Forest Products.

Wang, X., J. Wiedenbeck, and S. Liang

2009. Acoustic tomography for decay detection in black cherry trees. *Wood and Fiber Science*, 41(2):127–137.

Wyckhuyse, A. and X. Maldague

2001. A study of wood inspection by infrared thermography, part I: Wood pole inspection by infrared thermography. *Research in Nondestructive Evaluation*, 13:1–12.

Yang, X.

2008. *Simulation of Seismic Real and Virtual Data Using the 3D Finite-difference Technique and Representation Theorem*. Ph.D dissertation, Texas A&M University.